Breast Image Fusion Using Biomechanics

by Angela Wing Chung Lee

Supervised by Prof. Martyn P. Nash,
Assoc. Prof. Poul M. F. Nielsen and Dr. Vijayaraghavan Rajagopal

A thesis submitted in fulfillment of the requirements for the degree of
Doctor of Philosophy in Bioengineering,
The University of Auckland, 2011

Auckland Bioengineering Institute
The University of Auckland
New Zealand

December 2011

Abstract

Breast cancer is a leading cause of cancer mortality in women worldwide. Biophysical mathematical models of the breast have the potential to aid in the diagnosis and treatment of breast cancer. This thesis presents research on the development and validation of biomechanical models of the breast subject to gravity and compressive loads. The finite element method was used to implement the theory of finite elasticity coupled with contact mechanics in order to simulate the large non-linear deformations of the breast tissues.

Initially, validation studies were conducted using a breast phantom, which was placed in different orientations with respect to the gravity loading and compressed using a custom made device. A novel application of a block matching image processing method was used to quantitatively assess the accuracy of the biomechanics predictions throughout the entire phantom. In this way, systematic changes to the assumptions, parameters, and boundary constraints of the breast models could be quantitatively assessed and compared.

Using contact mechanics to model the interactions between the ribs and breasts can improve the accuracy of simulating prone to supine deformations due to the relative sliding of the tissues, as was observed using MRI studies on volunteers. In addition, an optimisation framework was used to estimate the heterogeneous mechanical parameters of the breast tissues, and the improvements to the models were quantified using the block matching comparison method.

A novel multimodality framework was developed and validated using MR and X-ray images of the breast phantom before being applied to clinical breast images. Using this framework, it

was shown that the parameters of the model (boundary conditions, mechanical properties) could be estimated and the image alignment improved. The biomechanical modelling framework presented in this thesis was shown to reliably simulate both prone to supine reorientation, and prone to mammographic compression, deformations. This capability has the potential to help breast radiologists interpret information from MR and X-ray mammography imaging in a common visualisation environment. In future, ultrasound imaging could also be incorporated into this modelling framework to aid clinicians in the diagnosis and management of breast cancer.

Acknowledgements

Table of Contents

List of Figures

List of Tables

Chapter 1: Introduction

1.1 Motivation

Breast cancer is the leading cause of cancer death for women, accounting for 14% of cancer mortalities in 2008 (Jemal et al., 2011). Early detection through X-ray mammography screening has been shown to reduce the mortality rate of this disease (Skaane, 2011). However, X-ray mammography imaging has its limitations, being unable to detect and distinguish with 100% accuracy the abnormalities in the breast (Baker, 1982, Berg et al., 2004). Other imaging modalities, such as ultrasound and magnetic resonance imaging (MRI), are therefore used in conjunction with X-ray mammography to image the breasts (Berg et al., 2004, Harms and Flamig, 2001).

X-ray mammography relies on compressing the breasts between two plates along the cranial-caudal (CC) and medio-lateral oblique (MLO) directions, and sending X-ray beams through the compressed breast tissues. In contrast, ultrasound and surgery are typically performed with patients lying in a supine position, and dynamic MRI is generally performed with an individual in the prone position. The challenge with interpreting and analysing these images together is that the breasts undergo large deformations between the modalities, and between images from the same modality.

Biomechanical models of the breast have shown promising results in their ability to predict the deformation of the breast tissues under different compression and gravity loading conditions (detailed literature reviews are contained within the relevant chapters). Previous work focussed on the use of landmark-based methods to assess the accuracy of biomechanical models, however, due to the complexity of the breast deformations, it is

important to assess the regional differences across the breast models. In this thesis, new image-based methods were developed to integrate image processing tools with modelling techniques to quantify the prediction accuracy of biomechanical models on a three dimensional, regional basis. These methods were used to quantify improvements to the biomechanical models, made by using more realistic boundary conditions and accounting for the heterogeneity of the breasts.

These techniques were validated on large deformations of a soft breast phantom before being applied to the breasts. The methods were then used to integrate the information derived from prone MR images with that from X-ray mammographic images. In addition, the use of block matching techniques in analysing the ability of the biomechanical models in predicting large deformations instead of landmark-based measures was validated and applied to breast models.

1.2   Thesis overview and contributions

The overall goal of this thesis was to develop novel methods to quantify and improve the predictions of biophysically-based finite element (FE) models of the breasts. In order to quantitatively evaluate the improvements of the biomechanical models of the breasts, a block matching comparison method was proposed and validated for determining the deformation position error over the models. Clinically relevant simulations were considered, with studies on prone to supine reorientation (e.g. for applications in merging information from MRI and ultrasound (US) images) and prone to compression (e.g. for merging information from MRI and X-ray mammograms) of the breast. Systematic improvements were made to the models by updating the rib boundary conditions with contact constraints and incorporating mechanical heterogeneity.

Chapter 2 provides a brief background on the anatomy and mechanical properties of breast tissues. Imaging techniques that are used in the diagnosis and management of breast cancer are described. The finite deformation and contact mechanics theory used in the simulation of the large deformations of the breasts are also described.

Chapter 3 validates a novel application of a three dimensional block matching method to assess the accuracy of FE models in simulating large deformations of soft materials, on a regional basis, using a breast phantom. Studies were performed with the breast phantom

placed under various compressive loads in the magnetic resonance (MR) scanner. Finite element models were used to simulate the deformations of the breast phantom under gravity and compressive loads using finite elasticity theory coupled with contact mechanics. Comparisons using block matching and feature-based methods were used to analyse the overall error between the FE model warped images and the experimental images. Techniques were also developed to take into account the heterogeneity of the breast phantom; the block matching method was used to quantify their effects on the accuracy of the simulations.

Chapter 4 uses the three dimensional block matching comparison method to assess the accuracy of physics-based models in predicting the deformations of the breasts for prone to supine reorientation. The block matching results indicated that improvements to the model could be made by changing the boundary conditions on the rib surface of the breast mesh to allow for tissue sliding. This was achieved using tied contact mechanic constraints. At that stage of the project, it was the first work on incorporating contact constraints on the rib surface of the breast models for prone to supine reorientation. Further improvements were then made to the models by incorporating information about the different mechanical properties of adipose and fibroglandular compartments of the breasts by using heterogeneous material parameters. The significant contribution of this chapter was the systematic analysis quantifying the importance of regional errors over the model. A novel application of the block matching method was used to define these regional errors, which were then used to estimate the material and contact stiffnesses of the breast models.

Chapter 5 compares the physics-based biomechanical models that have been developed for the breast phantom, and the breasts of volunteers, with a conventional image-based non-rigid registration algorithm. In addition, a hybrid method, where the biomechanical model was coupled with the image-based method, was used to align prone and supine breast images, and uncompressed and compressed breast phantom images. The important contribution in this chapter was the objective quantification of the registration errors, using block matching, for the three methods.

Chapter 6 describes studies using the breast phantom to validate techniques for a novel three dimensional MRI - two dimensional X-ray mammography multimodality image registration framework. The errors at each stage of the process were systematically quantified using the breast phantom studies. These methods were then demonstrated using a patient study, where MR and X-ray mammography images of the breasts were acquired. The information derived

from the images was used to improve the compression simulations of the biomechanical model by updating model parameters such as the boundary conditions and the material properties. The important contribution was the development of an optimisation framework, where the parameters of the FE model used to simulation compression were optimised based on the image similarity measure between a clinical X-ray mammogram and a pseudo X-ray mammogram generated from the FE warped MR prone image.

Chapter 7 summarises the work presented in this thesis and discusses the limitations and future directions.

1.3   List of publications

The main contributions of this research have been presented in the following peer reviewed publications:

- Rajagopal, V., **Lee, A. W. C.**, Chung, J. H., Nielsen, P. M. F., and Nash, M. P., 2007. Computational biomechanics of the breast: The importance of the unloaded reference state. Proceedings of Computational Biomechanics for Medicine II (MICCAI2007 Workshop), eds. Miller, K., Paulsen, K. D., Young, A. A., Nielsen, P. M. F., pp. 103-112.

- Rajagopal, V. **Lee, A. W. C.**, Chung, J. H., Warren, R., Highnam, R. P., Nielsen, P. M. F., and Nash, M. P., 2007. Towards tracking breast cancer across medical images using subject-specific biomechanical models. *Lecture Notes in Computer Science*, **4791**: 651-658.

- Rajagopal, V., **Lee, A. W. C.**, Chung, J. H., Warren, R., Highnam, R. P., Nielsen, P. M. F., and Nash, M. P., 2008. Creating individual-specific biomechanical models of the breast for medical image analysis. *Academic Radiology*, **15**(11): 1425-1436.

- **Lee, A. W. C**., Rajagopal, V., Bier, P., Nielsen, P. M. F., and Nash, M. P., 2008. Biomechanical modelling for breast image registration. Proceedings of SPIE Medical Imaging, **6918**(69180U).

- **Lee, A. W. C**., Rajagopal, V., Bier, P., Nielsen, P. M. F., and Nash, M. P., 2009. Correlation of breast image alignment using biomechanical modelling. Proceedings of

SPIE Medical Imaging, **7262**(726219).

- **Lee, A. W. C.**, Schnabel, J. A., Rajagopal, V., Nielsen, P. M. F., and Nash, M. P., 2010. Breast image registration by combining finite elements and free-form deformations. *Lecture Notes in Computer Science*, **6136**: 736-743.

- **Lee, A. W. C.**, Rajagopal, V., Chung, J. H., Nielsen, P. M. F., and Nash, M. P., 2010. Method for validating breast compression models using normalised cross-correlation. Chapter 7 in Computational Biomechanics for Medicine IV (MICCAI 2009 Workshop), eds. Miller, K., Nielsen, P. M. F., Springer, pp. 63-71.

- **Lee, A. W. C.**, Rajagopal, V., Reynolds, H., Doyle, A., Nielsen, P. M. F., and Nash, M. P., 2011. Breast X-ray and MR image fusion using finite element modelling. Proceedings of Workshop on Breast Image Analysis (MICCAI 2011 Workshop), eds. Tanner, C., Schnabel, J., Karssemeijer, N., Nielsen, M., Giger, M., Hawkes, D., pp. 129-136.

The work in this thesis was also presented at the following conferences:

- **Lee, A. W. C.**, Rajagopal, V., Chung, J. H., Nielsen, P. M. F., and Nash, M. P., 2007. Biomechanical model for breast image registration, Proceedings of the Physiological Society of N.Z., p. 66, MedSciNZ Congress, Queenstown N.Z., November.

- **Lee, A. W. C.**, Rajagopal, V., Chung, J. H., Nielsen, P. M. F., and Nash, M. P., 2008. Registration of breast MR images using a biomechanical model. Asia-Oceania Top University League on Engineering Postgraduate Conference (AOTULE), Auckland N.Z., September.

- **Lee, A. W. C.**, Rajagopal, V., Chung, J. H., Nielsen, P. M. F., and Nash, M. P., 2008. Image registration for a biomechanical breast model. Proceedings of the Physiological Society of N.Z., p. 68, MedSciNZ Congress, Queenstown N.Z., November.

- **Lee, A. W. C.**, Rajagopal, V., Chung, J. H., Nielsen, P. M. F., and Nash, M. P., 2008. Breast image registration using biomechanical modelling. *Australasian Physical & Engineering Sciences in Medicine*, **31**(4): 464-465. Engineering and Physical Sciences in Medicine & Australian Biomedical Engineering Conference (EPSM-ABEC), Christchurch N.Z., November.

- **Lee, A. W. C.**, Rajagopal, V., Chung, J. H., Nielsen, P. M. F., and Nash, M. P., 2009. Breast MR image registration using a biomechanical model. Proceedings of the XXXVI International Congress of Physiological Sciences (IUPS 2009) Function of Life: Elements and Integration. Kyoto Japan, Springer, p. 353, August.

- **Lee, A. W. C.**, Babarenda Gamage, T. P., Rajagopal, V., Nielsen, P. M. F., and Nash, M. P., 2010. In-vivo estimation of breast tissue mechanical properties using 3D normalised cross-correlation. Proceedings of the Physiological Society of N.Z., p. 59, MedSciNZ Congress. Queenstown N.Z., November.

Chapter 2: Breast imaging, anatomy and modelling

Here the background material relating to this thesis is presented. The imaging physics necessary for image fusion applications is described, followed by an introduction to the anatomy and finite element theory needed for breast modelling.

2.1 Breast cancer imaging

Breast cancer is the most common cause of cancer death for women (Jemal et al., 2011, Parkin et al., 2005). In order to increase the chance of survival by detecting breast cancer at its early stages, breast cancer screening programs have been set up worldwide (Jemal et al., 2011). X-ray mammography is considered the 'gold standard' for breast cancer screening and allows clinicians to make diagnostic decisions based on the visualisation of internal breast tissues (Ikeda, 2011). It has been estimated that regular mammographic screening can reduce the mortality rate of breast cancer by 35% to 40% (Skaane, 2011). During X-ray mammography the breasts are compressed either in the cranial-caudal (CC) or the medio-lateral-oblique (MLO) directions and a short burst of radiation is applied to the breast to form the two dimensional X-ray image (Bushberg et al., 2002). In order to more reliably interpret the images, mammograms are seldom considered independently, but are considered in the context of previous scans (temporal comparison) or between the left and right sides, as asymmetry in the structures can indicate abnormality (bilateral comparisons).

2.1.1 X-ray mammography physics

One aim of this thesis was to merge information from MRI and X-ray using knowledge about the physics of soft tissue deformation (see Chapter 6). To do this pseudo X-rays were generated, which requires a basic understanding of the physics of the X-ray mammography system. X-rays are produced by an X-ray tube in mammographic systems, where a voltage is applied between two electrodes inside a vacuum tube. As the electrons travel from the negatively charged cathode to the positively charged anode, they accelerate, gaining kinetic energy due to the electrical potential difference. When the beam of electrons hit the anode, electron deceleration and electron ejection produces a polyenergetic X-ray beam, where the maximum energy of the X-ray beam is dependent on the potential difference between the anode and cathode.

Electron deceleration occurs as electrons in the energetic beam are deflected by the electrostatic fields of the material's atoms. When the electron is deflected it loses kinetic energy, which is emitted in the form of an X-ray photon. Electron ejection occurs when electrons from the electron beam collide with electrons orbiting the nucleus of the atom in the material with sufficient energy. When electrons from the inner electrons shells (e.g. K-shell) are ejected, electrons from the outer shells drop down to fill the vacant position, and in the process emit X-ray radiation. The energy associated with these X-rays is dependent on the differences in the binding energies of the electron shells, resulting in characteristic radiation wavelength profiles for different materials.

A rhodium anode was used during the mammographic image acquisition for the breast phantom and the Patient study in the present thesis. The characteristic radiation for rhodium occurs at 20.2 keV and 22.7 keV, respectively, leading to peaks in the energy spectrum at these specific energy levels. Filtering (e.g. 25 μm rhodium filter, vacuum tube) was used to attenuate low and high energies in the energy spectrum resulting in the energy spectrum shown in Figure 2.1 (Bushberg et al., 2002).
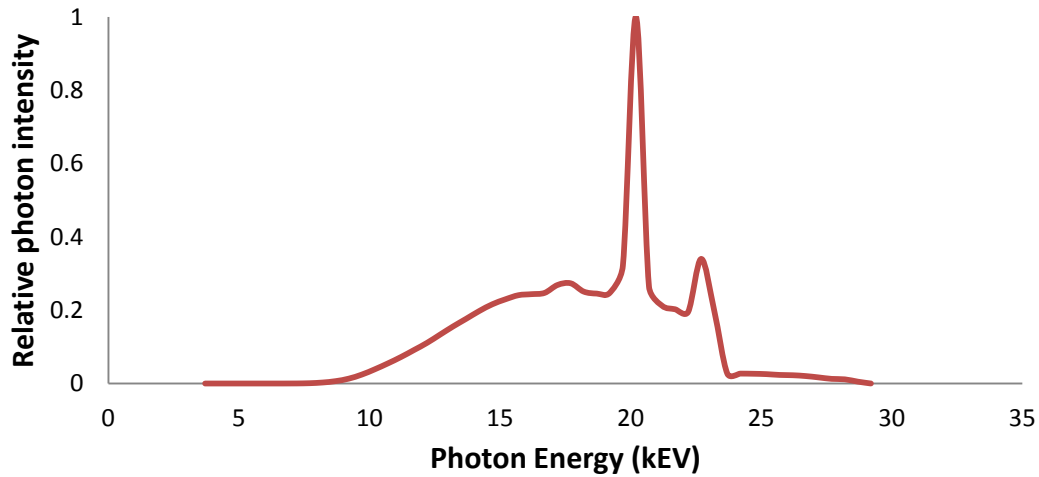
Figure 2.1: Energy spectrum of a Rhodium anode with a 0.025 mm Rhodium filter with a peak tube voltage of 29 kV.

This polyenergetic X-ray beam is attenuated as it passes through tissues due to interactions between the X-ray photons and the atoms in the tissues, resulting in a decrease in radiation intensity reaching the detector. The Beer-Lambert law gives the relationship between the transmitted (I) and incident (I_0) X-rays as:

$$I = I_0 e^{-\sum_i \mu_i x_i} \tag{2.1}$$

where x_i is the thickness and μ_i is the linear attenuation coefficient of attenuating material i.

The linear attenuation coefficient is dependent on the density of the material that the X-ray beam travels through; therefore the mass attenuation coefficient, $\left(\mu/\rho\right)$ is more widely reported (Bushberg et al., 2002, Hubbell and Seltzer, 2004). X-ray mass attenuation coefficients for different types of tissues are dependent on the combined effect of the photoelectric effect, the Compton effect and coherent scattering. These factors are dependent upon the energy of the X-ray, thus the mass attenuation coefficient is also dependent on the energy of the X-ray beam as shown in Figure 2.2 (Hubbell and Seltzer, 2004).
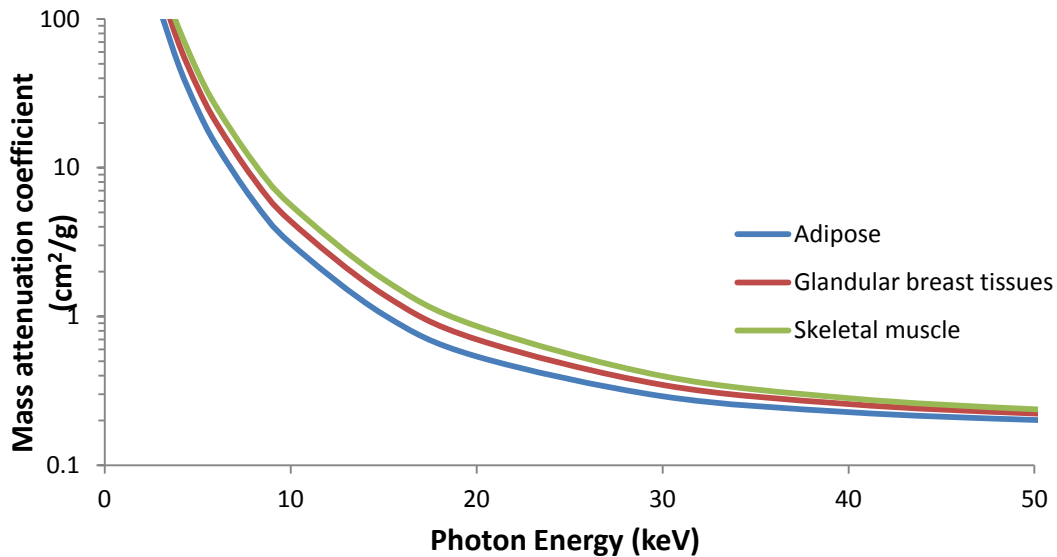
Figure 2.2: Mass attenuation coefficients for adipose, glandular and skeletal muscle tissues.

The attenuation characteristics of different types of material for the polyenergetic beam can be approximated by an equivalent attenuation coefficient, μ_{equ} at an effective monoenergtic beam (Robinson and Scrimger, 1991):

$$\mu_{equ} = -\frac{1}{x}\ln\left[\sum_{i=1}^{N}\frac{I_i}{I_0}\exp\left(-\mu_i x\right)\right] \qquad (2.2)$$

where I_i is the number of photons at the energy value i, I_0 is the incident energy beam (approximated as a sum of the photons at each energy level i), μ_i is the mass attenuation coefficient at energy i, and x is an arbitrary thickness of tissue that the beam passes through.

The above calculations were used to give an approximation of the initial 'for processing' mammogram. However, the data that was acquired for the breast phantom and the Patient studies were the 'for presentation' images. This means that after the image was acquired, image processing was performed to allow the clinicians to interpret the information with greater ease. For the mammography system used to obtain the images in this thesis (Senographe DS, General Electric, Connecticut, USA), this involved unsharp masking, thickness equalisation and negative logarithmic transform, for which a higher intensity in the image corresponds to a greater amount of photons applied to the 'for processing' image.

Unsharp masking is an image processing technique used to sharpen the image and can be expressed with the following equation (Bick and Diekmann, 2010):

$$y' = y + c * \left(y - s(\sigma)\right) \qquad (2.3)$$

where *y'* and *y* are the processed and original images, respectively, *s* is the smoothed image and *c* is a constant determining the level of enhancement. The blurring was performed using Gaussian smoothing.

Thickness correction or peripheral enhancement compensates for the lower image intensities at the edge of the compressed breast by the addition of an image representing the tissue thickness. A two dimensional image was generated by projecting through a three dimensional mask of the FE warped image. This image was normalised and inverted, then multiplied with a correction factor representing the image intensity of the adipose tissue (obtained from the mammogram image) to generate the thickness image.

2.1.2 Breast cancer screening

The sensitivity of X-ray mammography screening, where malignant tumours are identified as such, has been found to vary from 45% (for dense breasts) to 100% (for fatty breasts) (Berg et al., 2004). Early studies have also found that X-ray mammography has low specificity (less than 20% (Baker, 1982)), which can lead to unnecessary biopsies being performed. Therefore, as an adjunct to X-ray mammography, other imaging modalities, such as magnetic resonance imaging (MRI) and ultrasound are used (Berg et al., 2004, Harms and Flamig, 2001, Sardanelli et al., 2004). It has been found that a combination of the information from multiple modalities leads to more reliable diagnosis and management of breast cancer compared to any individual test (Berg et al., 2004, Malur et al., 2001).

Ultrasound works by the interaction of tissues with ultrasound waves, which are transmitted by a probe. When these waves hit an interface of materials with different mechanical impedance, they are either absorbed or reflected back to the probe. Different materials can be distinguished from each other by the different amplitudes of echoes. Breast ultrasound is performed on patient's in order to further investigate suspicious lesions found with mammography, or from lumps felt in the breast by the patients self examination or during a physical exam (Ikeda, 2011).

The other most common adjunct for breast imaging is contrast-enhanced MRI (CE-MRI). CE-MRI is used to differentiate between benign and malignant tumours found in the breast, thus reducing the need for surgical biopsies on benign tumours (Harms and Flamig, 2001). The enhancement of cancerous tissue tends to be greater and faster than the surrounding normal breast tissues due to the increased vascularisation in dynamic MR imaging (Warren

and Coulthard, 2002). Breast MRI is more sensitive than breast ultrasound and mammography, and can be used to detect tumours that are detected in a physical examination but are invisible in mammographic images (Warren and Coulthard, 2002). Unlike mammography, MRI and ultrasound are not limited by dense breasts (Berg et al., 2004). However, image artefacts due to patient movement (for example breathing) during image acquisition can complicate the interpretation of the images (Warren and Coulthard, 2002).

2.1.3 Breast image registration

In order to aid clinicians in interpreting inter- or intra-modality breast images, image registration techniques have been applied to breast images. The methods used for breast image registration have been discussed in detail by Guo et al. (2006), Rueckert et al. (1999), Sivaramakrishna (2005) and therefore only a brief introduction into breast image registration is given in this chapter. For greater detail on biophysically-based breast image registration refer to Section 4.2 for gravity loading deformations and Section 6.1 for previous work on breast compressions.

Breast image registration is used to find the optimal transformation to apply to one image (source) to align it to another image (target). The general framework for a registration problem is a similarity measure, a transform, and an optimizer. The source image is transformed to align with the target image, and the similarity between the transformed source image and the target image is computed using a similarity measure. An optimiser is used to find the parameters of the transformation that best align the two images according to the similarity measure.

Similarity measures can be classed as intensity-based or feature-based methods. Feature-based measures typically require pre-processing of the images prior to the registration to identify the features such as contours, landmarks, or surfaces and the accuracy of these methods is dependent on the accurate extraction of the features. For intensity-based methods, an error measure is calculated directly from the images. There are a range of intensity-based similarity measures that can be used for image registration such as: sum of squares differences (SSD), normalised cross correlation (NCC), and normalised mutual information (NMI) (Eq.2.4, 2.5, 2.8). SSD is best used for images acquired using the same modality where the pixel intensities associated with the same region is unchanged in the source and target images. If there is linear scaling of the intensities, then NCC would be more

appropriate. In this thesis, NCC was used to assess the similarity of experimental and FE-warped MR images. The SSD and NCC similarity measures are calculated as follows:

$$SSD(A,B) = \sum_N (A_i - B_i)^2 \tag{2.4}$$

$$NCC(A,B) = \frac{\sum_N (A_i B_i)}{\sqrt{\sum_N {A_i}^2 \sum_N {B_i}^2}} \tag{2.5}$$

NMI gives a measure of the mutual dependence of the images on one another and is appropriate when there are statistical dependencies between the intensities, and is suitable for multimodality image registration. This similarity measure computes the sum of the Shannon entropies (*H*) of the two images and then normalises it by the joint entropy (*H(A,B)*) of the two:

$$H(A) = -\sum_a p(a) \log p(a) \tag{2.6}$$

$$H(A,B) = \sum_{a,b} p(a,b) \log p(a,b) \tag{2.7}$$

$$NMI(A,B) = \frac{H(A) + H(B)}{H(A,B)} \tag{2.8}$$

where *p(a)* is the probability of a pixel in image *A* having an intensity of *a*.

2.2   Breast anatomy

In order to accurately model breast biomechanics under different loading conditions, a basic understanding of the breasts and their internal structures is required. The classical definition of the female breast places it anterior to the *pectoralis major* muscle on the thoracic wall with the superior and inferior margins extending from the second to sixth ribs, respectively. The medial boundary extends to the sternum. Typically the breasts are tear drop shaped, with the tail extending up to the mid-axillary line.

With reference to Figure 2.3, the breast (mammary gland) is composed of fibrous, adipose, and glandular tissue. Subcutaneous adipose lies beneath the skin, and the amount of adipose tissue inside the breast depends on the total body fat percentage, and as such can vary substantially between individuals (Sabel, 2009). Generally each mammary gland consists of 15-20 glandular lobes that converge at the nipple and can secrete milk for the nourishment of babies. These glandular lobes are surrounded and separated from each other by dense fibrous connective tissue, known as Cooper's ligaments (Cooper, 1840), while collectively these

structures are grouped together as the fibroglandular tissue. Cooper's ligaments provide internal suspensory support to the breast tissues by extending antero-posteriorly throughout the breast tissues and attaching perpendicularly onto the overlying skin (Macéa and Fregnani, 2006, Pandya and Moore, 2011).

Figure 1.2A "Lateral view and sagittal section of breast. From Drake RL, Vogl AW, Mitchell AWM, et al. Gray's atlas of anatomy. Edinburgh: Churchill Livingstone; 2008." Hall-Findlay, E. J. and Evans, G. R. D. 2010. *Aesthetic and reconstructive surgery of the breast.* Edinburgh, Saunders Elsevier.

Figure 2.3: Lateral view of the breast. Adapted from Drake et al. (2008).

The breast tissues are attached to the skin via Cooper's ligaments and lie upon the deep investing fascia (dense connective tissue) surrounding the *pectoralis major, serratus anterior* muscles, and the *anterior rectus sheath* (Hall-Findlay and Evans, 2010, Sabel, 2009). The fascia surrounding the muscles allows them to slide against each other and over the ribs. These muscles then attach to the ribs, sternum, and clavicle as shown in Figure 2.4.
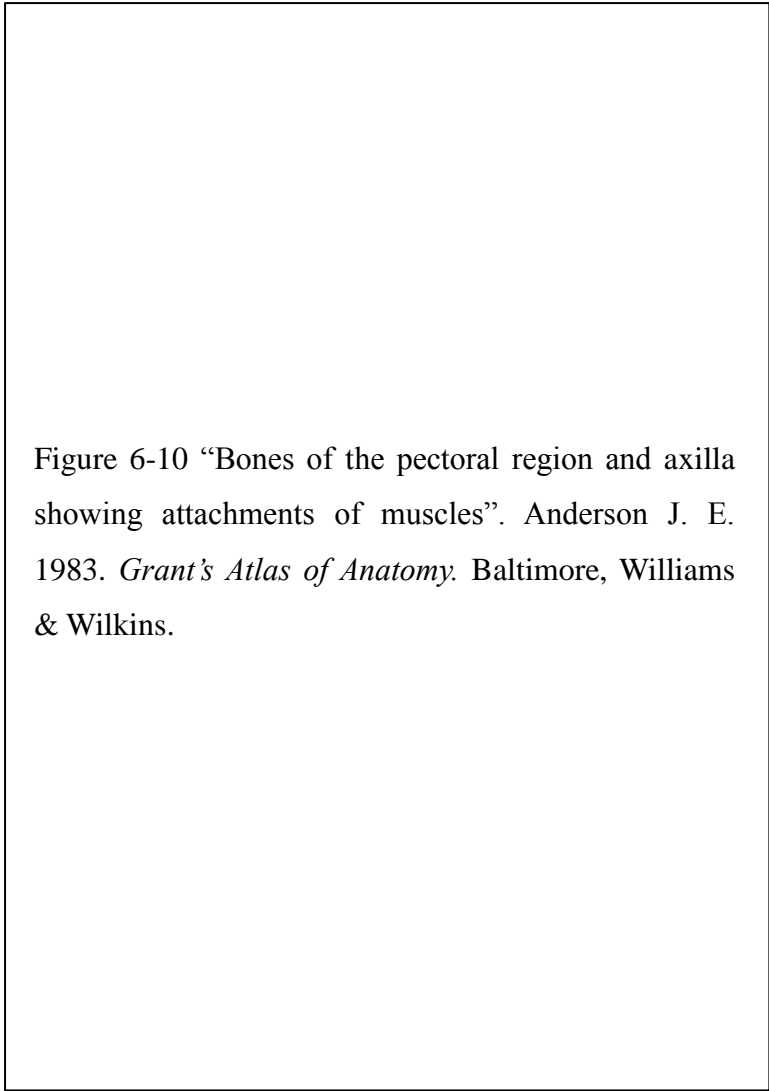
Figure 6-10 "Bones of the pectoral region and axilla showing attachments of muscles". Anderson J. E. 1983. *Grant's Atlas of Anatomy.* Baltimore, Williams & Wilkins.

Figure 2.4: Bones of the Pectoral region and axilla showing attachments of muscles. Reproduced from Anderson (1983).

Between the fibrous tissue surrounding the mammary gland and the deep fascia of the pectoralis major muscle, there is a space known as the *retromammary bursa* (Macéa and Fregnani, 2006), which is composed of loose connective tissue arranged almost horizontally (Pandya and Moore, 2011, Riggio et al., 2000). The mobility of the breast is dependent upon the *retromammary bursa* and the Cooper's ligaments.

2.3   Breast tissue mechanical properties

Studies have been performed to identify the mechanical properties of normal and pathological breast tissues (O'Hagan and Samani, 2009, Samani et al., 2007). In the clinical arena, the stiffness of breast tissues is of interest, as tumours have been found to be substantially stiffer

than normal breast tissue, with malignancy corresponding to an increase in stiffness (Egorov et al., 2009, Samani et al., 2007). Pathological breast tissues have been found to be two times to two orders of magnitude stiffer than normal breast tissues (O'Hagan and Samani, 2009).

The composition of normal breast tissues depends on the hormonal and temporal influences. During the menstrual cycle the breast tissue can increase in volume from approximately 15 cm^3 to 30 cm^3 due to the influence of hormones such as estrogen and progesterone (Sabel, 2009). In addition, the elasticity of the fibroglandular tissue has been found to significantly change (up to 35%) during the menstrual cycle (Lorenzen et al., 2003). On a larger time scale, when women go through menopause, the breast undergoes structural changes where the glandular tissue decreases in volume and is replaced with fatty tissue due to the loss of hormonal stimulation (Sabel, 2009).

A large range of values have been reported for the mechanical properties of the adipose and glandular tissue mechanical properties based on ex-vivo mechanical testing of small tissue samples (Kerdok et al., 2005, Krouskop et al., 1998, Samani and Plewes, 2004, Samani et al., 2007, Wellman, 1999). Within the literature the elastic moduli of the adipose and glandular tissue has been reported to range from 0.5 kPa to 25 kPa and from 2 kPa to 66 kPa, respectively (Gefen and Dilmoney, 2007). Krouskop et al. (1998) and Wellman (1999) found that the level of precompression has a significant effect on the elastic modulus of the glandular tissue, indicating the non-linear nature of its mechanical properties. Hyperelastic constitutive relations have therefore been used to describe the mechanical properties of normal breast tissues (Krouskop et al., 2003, O'Hagan and Samani, 2009, Samani and Plewes, 2004, Samani et al., 2007).

An inherent limitation of ex-vivo studies is that isolating small sections of breast tissue for testing removes the constraints from the surrounding structures that would influence the mechanical properties of the breast tissues. In addition, the mechanical properties of the breast tissues are highly variable across a population and also vary over time for any individual.

In-vivo studies of breast tissues have been conducted by imaging the breast under different loading conditions. One method is MR elastography, where dynamic images are acquired of the breast while small perturbations (typically less than 500 μm) are applied at low frequencies (75 Hz - 300 Hz) (McKnight et al., 2002, Van Houten et al., 2003). These images are used to identify changes in strain in the breast tissues in order to calculate the shear

stiffness. A limitation of this method is that only small deformations are applied to the breasts, thus the derived properties are primarily related to the dynamic stiffness of the tissues.

FE models have been used to model quasi-static deformations, due to gravity or compressive loads, to estimate the in-vivo mechanical properties of the breast tissues. For further details on previous biomechanical breast models used to simulate gravity loading or compression loading please refer to Chapter 4 and Chapter 6, respectively. Various material relations have been investigated such as: linear elastic (Carter et al., 2006, Schnabel et al., 2003, Shih et al., 2010, Tanner et al., 2006, 2008), exponential (Ruiter et al., 2006, 2008), and neo-Hookean (Carter et al., 2009, Chung et al., 2008a, del Palomar et al., 2008, Rajagopal et al., 2008b, Ruiter et al., 2006, Samani et al., 2001, Tanner et al., 2006). It has been shown that the use of the neo-Hookean constitutive relation results in realistic predictions of the reorientation of the breast from prone to supine and compressions of up to 38% (Chung et al., 2008a, Rajagopal et al., 2008b).

The mechanical behaviour of the breast tissues has been modelled as either homogeneous (Carter et al., 2008, Chung et al., 2008b, del Palomar et al., 2008, Rajagopal et al., 2008b) or with specific tissues such as the adipose, fibroglandular, skin, and muscle being considered independently (heterogeneous models) (Carter et al., 2006, Ruiter et al., 2006, Samani et al., 2001, Schnabel et al., 2003, Shih et al., 2010, Tanner et al., 2006, 2009). The parameters of these material relations have typically been optimised based on distance measures of features such as the skin surface (Carter et al., 2009, Rajagopal et al., 2008b).

Even though Cooper's ligaments play an important role in the shape and structure of the breast, they have not been modelled explicitly in any published model to date. This is likely to be due to the image resolution and computational cost associated incorporating these structures into the FE models (Babarenda Gamage et al., 2011). However, it has been proposed that the effect of the Coopers ligaments can be modelled using anisotropic constitutive relations for the breast (Tanner et al., 2009, 2010, 2011).

The skin tissue is also highly variable between individuals, with its thickness ranging from 0.8mm to 3mm, typically decreasing proportionally with increasing breast size (Hall-Findlay and Evans, 2010). The mechanical properties of the skin have been modelled by assigning the top layer of elements in the three dimensional FE model as skin (Tanner et al., 2009) or by coupling a two dimensional layer of elements with the anterior surface of the FE mesh (del

Palomar et al., 2008, Ruiter et al., 2006). In this thesis, the effect of skin was ignored in favour of investigating the effects of boundary conditions on the rib surface, and homogeneous versus heterogeneous material properties. There are a number of factors that would need to be considered when incorporating skin into biomechanical models of the breast, such as the interface conditions between the skin and the underlying tissues, skin mechanical properties, and the state of the pre-stress of skin in the different loaded configurations of the breasts (Babarenda Gamage et al., 2011).

2.4   Finite deformation elasticity mechanics

In this chapter a brief introduction of the mechanical theory used to simulate the large deformations of the breast tissues and the breast phantom is given. For a more in-depth description of three dimensional finite elasticity theory please refer to Malvern (1969) and Atkin and Fox (1980).

2.4.1 Kinematic equations

In this thesis the motion of the breast tissues and breast phantom due to the application of different loads is of interest. The motion of an object from an undeformed (reference) state (**X**) to a deformed configuration (**x**) can be represented using the deformation gradient tensor **F**:

$$F = \frac{\partial x}{\partial X} \tag{2.9}$$

A measure of the strain in the system can be quantified using the Green-Lagrange strain tensor (**E**), which is related to the right Cauchy-Green deformation tensor (**C**) and the identity tensor (**I**) as:

$$E = \frac{1}{2}(C - I) \tag{2.10}$$

$$C = F^T F \tag{2.11}$$

2.4.2 Stress equilibrium

Conservation of mass requires that the mass before and after deformation of a body remains the same, resulting in the following equation:

$$\rho_0 = J\rho, \tag{2.12}$$

where $J = \det(F)$ and ρ_0 and ρ are densities of the body in the reference and deformed states, respectively. It can be seen that J also relates the volume of the reference mesh, V with

the volume in the deformed mesh, v by: $dv = J dV$.

Conservation of linear momentum for a quasi-static system results in the following equation:

$$(\nabla \cdot \boldsymbol{\sigma} + \boldsymbol{b}) = 0 \qquad (2.13)$$

where $\boldsymbol{\sigma}$ represents the Cauchy stress tensor and $\boldsymbol{b}$ is the body force per unit mass applied to the body.

Other stress tensors for finite elasticity include the 1st and 2nd *Piola Kirchhoff* stress tensors given as $\mathbf{P}$ and $\mathbf{S}$ respectively: $\mathbf{P} = J\boldsymbol{\sigma}\mathbf{F}^{-T}$, $\mathbf{S} = J\mathbf{F}^{-1}\boldsymbol{\sigma}\mathbf{F}^{-T}$. Conservation of angular momentum results in a symmetry condition on the Cauchy stress tensor, $\boldsymbol{\sigma}$ (and hence the 2nd *Piola Kirchhoff* stress tensor, $\mathbf{S}$).

The principle of virtual work is a weak form of the stress equilibrium equations and can be used as the governing equation for the finite deformation elasticity problem:

$$\delta W = \int_V J\boldsymbol{\sigma} : \frac{\partial(\delta\boldsymbol{u})}{\partial\boldsymbol{x}} dV - \int_S \boldsymbol{t} \cdot \delta\boldsymbol{u} \, dS - \int_V \boldsymbol{b} \cdot \delta\boldsymbol{u} \, dV = 0 \qquad (2.14)$$

where $\boldsymbol{t}$ is the surface traction vector and $\delta\boldsymbol{u}$ is the virtual displacement field.

Breast tissues are generally regarded as being incompressible; implying that $J = 1$. This constraint can be weakly enforced using:

$$\int_V \delta p(J - 1) \, dV = 0 \qquad (2.15)$$

where δp is a variation of the hydrostatic pressure. The hydrostatic pressure, p can be regarded as a physical stress, which needs to be determined in order to maintain zero volume change.

2.4.3 Constitutive equations

Constitutive equations describe the relationship between the stresses and strains of an object. A hyperelastic relationship is one that is path independent, where one only considers the reference and the final deformed state. A commonly used hyperelastic material relation for biological tissues is the neo-Hookean relationship, which assumes that the material is isotropic and incompressible:

$$\psi = C_1(I_1 - 3) \qquad (2.16)$$

where the strain energy function, ψ is a function of the invariant trace of $\mathbf{C}$, $I_1 = trace(C)$ and C_1 is a scalar material coefficient.

The stresses can be calculated by differentiating the strain energy function, ψ with respect to a measure of strain:

$$S = \frac{\partial \psi(E)}{\partial E} = \frac{\partial \psi(C)}{\partial C} \frac{\partial C}{\partial E} = 2 \frac{\partial \psi(C)}{\partial C} \tag{2.17}$$

2.5   Contact mechanics

Contact mechanics was used to model the interactions of the breast phantom and breast tissues against compression plates (see Chapter 3 and Chapter 6, respectively) and the breast tissues against the ribs (see Chapter 4 and Chapter 6). A brief outline on the theory is presented here, for more details please refer to Bonet and Wood (1997), Laursen (2002) and Chung (2008). In order to model the contact interactions between two objects as a coupled problem, one object is designated the slave, and the other the master. As can be seen in Figure 2.5, contact points are defined on the slave surface and are projected onto the master surface. At the projected point on the master surface, two tangent vectors, τ_1, τ_2 are given as:

$$\boldsymbol{\tau}_\alpha = \frac{\partial \boldsymbol{x}^{(2)}}{\partial \xi_\alpha}, \alpha = 1,2 \tag{2.18}$$

The distance between the slave and master meshes is given by the gap function, g_N:

$$g_N = -\boldsymbol{n}.(\boldsymbol{x}^{(1)} - \boldsymbol{x}^{(2)}) \tag{2.19}$$

where $\boldsymbol{n}$ is the unit outward normal vector on the master surface and is calculated as:

$$\boldsymbol{n} = \frac{\boldsymbol{\tau}_1 \times \boldsymbol{\tau}_2}{\|\boldsymbol{\tau}_1 \times \boldsymbol{\tau}_2\|} \tag{2.20}$$

With regard to Figure 2.5, when there is overlap between the two objects, the gap function is positive and, when there is no penetration, the gap function is negative.
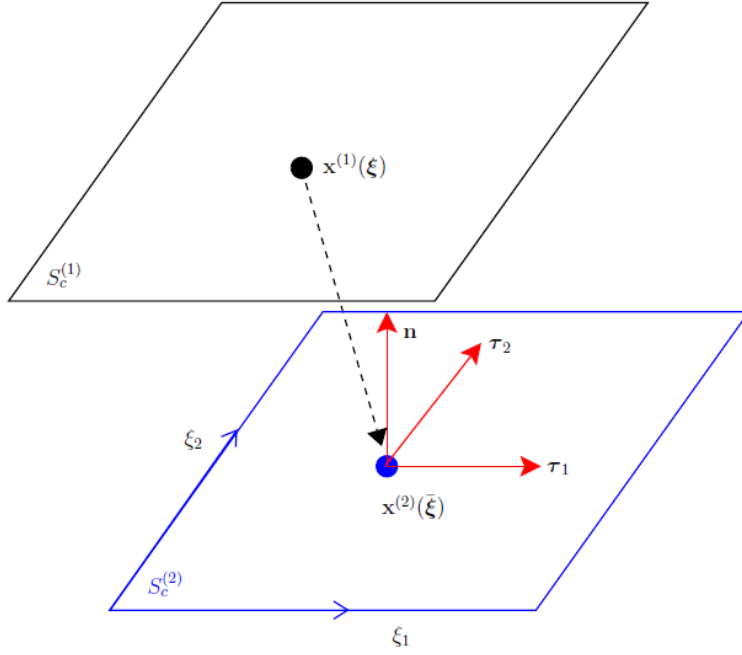
Figure 2.5: Contact between two surfaces is modelled by projecting contact points, $\boldsymbol{x}^{(1)}$ from the slave surface (black) onto the master surface (blue). Reproduced from Chung (2008).

The governing equation for a coupled contact problem can be obtained by combining the principle of virtual work associated with each body, $\delta W^{(i)}$ with the contact residual, δW_c to obtain the total coupled virtual work, $\delta W^{coupled}$:

$$\delta W^{coupled} = \sum_{i=1}^{2} \{\delta W^{(i)}\} + \delta W_c \tag{2.21}$$

$$\delta W_c = \int_{S_c^{(1)}} [(t_{T_\alpha} \boldsymbol{\tau}^\alpha - t_N \boldsymbol{n}) \cdot (\delta \boldsymbol{u}^{(1)} - \delta \boldsymbol{u}^{(2)})] dS_C^{(1)} \tag{2.22}$$

where $\delta \boldsymbol{u}^\alpha$ are the virtual displacements associated with each body, t_N and t_{T_α} (where $\alpha = 1,2$) represent the normal and tangential components of the contact pressure, respectively. The integral is defined over the slave surface, $S_c^{(1)}$ and $\boldsymbol{n}$ is the normal base vector at the projected point on the master surface [Figure 2.5]. While $\boldsymbol{\tau}^\alpha$, the contravariant basis vectors are given as:

$$\boldsymbol{\tau}^\alpha = m^{\alpha\beta} \boldsymbol{\tau}_\beta, \qquad m^{\alpha\beta} = \left(\boldsymbol{\tau}_\alpha \cdot \boldsymbol{\tau}_\beta\right)^{-1} \tag{2.23}$$

where $\alpha, \beta = 1,2$.

2.5.1 Frictionless contact

The tangential and normal components of the contact traction are dependent on the type of

contact condition between the slave and master objects. The contact interactions between the slave object and master object can be modelled as frictionless, frictional, or tied. In Chapter 3, experiments were conducted where a breast phantom was compressed with and without lubrications. The compression experiments where lubrication was applied were approximated as being frictionless. Frictionless contact can be described using the *Kuhn-Tucker* optimality conditions (Laursen, 2002):

$$g_N \leq 0 \quad , \quad t_N \geq 0 \quad , \quad t_N g_N = 0 \tag{2.24}$$

where g_N represents the gap function and t_N represents the contact pressure. If there is no contact ($g_N < 0$), then there is no contact pressure ($t_N = 0$); however if there is contact ($g_N = 0$), then there is positive contact pressure ($t_N > 0$).

The penalty method, as described by Chung et al. (2008a) and Laursen (2002), was used to implement these contact constraints, where a penalty parameter C_N is introduced to approximate the *Kuhn-Tucker* conditions:

$$t_N = \begin{cases} C_N g_N \, , & if \ g_N \ \geq 0 \\ 0 \quad , & \text{otherwise} \end{cases} \tag{2.25}$$

It can be seen in the schematic illustration in Figure 2.6, that the Kuhn-Tucker conditions are met only when $C_N \rightarrow \infty$, otherwise there is some degree of penetration between the master and slave meshes.
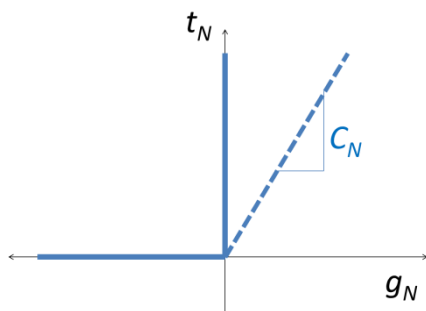
Figure 2.6: Frictionless contact: The bold line defines the admissible combinations of the contact gap (g_N) and contact pressure as given by the Kuhn-Tucker conditions. The dotted line represents the penalty approximation of these conditions. See Laursen (2002) for further detail.

2.5.2 Frictional contact

In Chapter 3, the breast phantom was compressed with no lubrication applied between the compression plates and the phantom (frictional conditions). Instead of the *Kuhn-Tucker*

conditions described above, a Coulomb friction law can be used to describe the frictional behaviour between two objects, where the following conditions must be met, as illustrated in Figure 2.7:

$$\| \, t_T \, \| \leq \mu t_N \tag{2.26}$$

$$g_T = \lambda t_T, \quad where \begin{cases} \lambda = 0, & if \ \| \, t_T \, \| < \mu t_N \\ \lambda \geq 0, & if \ \| \, t_T \, \| = \mu t_N \end{cases} \tag{2.27}$$

where no tangential slip (g_T) occurs when the tangential stress (t_T) is less than the frictional coefficient (μ) times the normal contact pressure (t_N). When slip does occur, it is co-linear with the frictional stress given by μt_N.

Similar to the approach taken for the frictionless case, the frictional conditions above can be approximated by introducing a penalty parameter, namely the tangent stiffness, C_T, as illustrated in Figure 2.7. Instead of there being only slip or no slip as given by the conditions above, a new stick state is introduced:

$$t_t = \begin{cases} C_T g_T, & if \ \| \ C_T g_T \, \| < \mu t_N \ (stick) \\ \mu t_N \dfrac{\| \, t_T^{trial} \, \|}{t_T^{trial}}, & if \ \| \ C_T g_T \ \| > \mu t_N \ (slip) \end{cases} \tag{2.28}$$

The stick state can be considered as a recoverable elastic micro-deformation on the contacting surface. As before, the slip state occurs when the tangential stress exceeds the frictional coefficient (μ) times the normal contact pressure (t_N). When slip does occur, it is co-linear with the frictional stress given by μt_N and in the direction given by the tangential stress.
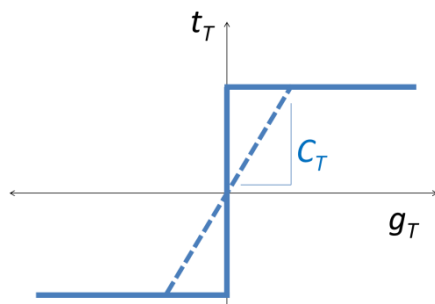
Figure 2.7: Frictional contact: The bold line defines the admissible combinations of the tangential slip (g_T) and tangential stress as given by Coulomb frictional laws. The dotted line represents the penalty approximation of these conditions. See Laursen (2002) for further detail.

2.5.3 Tied contact

Neither frictionless nor frictional contact constraints are appropriate for modelling breast-rib interface interactions as the breasts do not slide freely over the chest wall, but have a restricted range of motion due to the suspensory ligaments and the retromammary bursa that attach it to the skin and chest wall. The tangential motion of the breast tissues is generally recoverable. Therefore, the interaction of the breast tissues with the chest wall was approximated by using tied contact (Chung et al., 2008b, Reynolds et al., 2011), where an elastically recoverable sliding condition was enforced (see Chapter 4 and Chapter 6). The tangential contact pressure, t_T is dependent on the contact gap, g_T and a penalty parameter, C_T:

$$t_T = C_T g_T \qquad\qquad (2.29)$$

It can be seen in Figure 2.8 that as the tied contact stiffness, $C_T \to \infty$, the zero-displacement boundary conditions would be replicated.
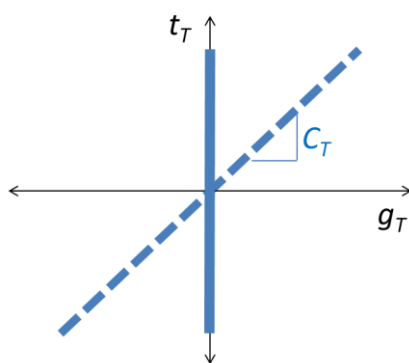
Figure 2.8: Tied contact: The dotted line replicates the tied contact relationship between the tangential motion, g_T and the tangential contact pressure, t_T. The zero-displacement boundary condition on the contact surface will be approximated as $C_T \to \infty$ (bold line). See Chung (2008) for further detail.

2.6   Finite element implementation

The finite element method (FEM) was used to model the large deformations of the breast shaped phantom and breast tissues under both gravity and compressive loads using an in-house mathematical modelling framework, *Continuum Mechanics, Image analysis, Signal*

processing and System identification (*CMISS*[1]). In this section only brief overview of FEM is given; for a more in-depth explanation of FEM please refer to Zienkiewicz and Taylor (2005).

The foundation of FEM is that complex problems can be approximated by discretising a continuous domain into sub-domains (elements), which can then be used to solve the governing equations for the coupled problem (Eq. 2.14, 2.21, 2.22). The elements are defined with basis functions, such as linear Lagrange or cubic Hermite shape functions, with a local material coordinate system *ξ,* that ranges from 0 to 1.

Linear Lagrange meshes approximate the field (e.g. geometric) as a weighted sum of the boundaries of each element (node points). Linear Lagrange meshes only have C^0 continuity (piecewise continuous), whereas cubic Hermite meshes have higher order continuity (C^1 slope). In this thesis, the geometry of the breast tissues and the breast phantom were represented with cubic Hermite basis functions.

In order to numerically evaluate the volume and surface integrals (Eq. 2.15, 2.23), the Gauss-Legendre quadrature method was used. Gaussian quadrature approximates an integral as a weighted sum of the function's values at specific points. These points are termed Gauss points and for *n* Gauss points, a polynomial of order 2*n*-1 can be exactly integrated. For a 1D function, the integral can be approximated as:

$$\int_0^1 f(\xi)d\xi \approx \sum_{i=1}^n w_i f(\xi^i) \tag{2.29}$$

where w_i is the weight for each Gauss point ξ^i in an *n* Gauss point scheme.

The coupled contact mechanics problem (Eq. 2.21) can be solved using the Newton-Raphson method by reformulating the system of nonlinear equations to:

$$\left(\boldsymbol{K}_{coupled} + \boldsymbol{K}_c\right)\Delta\boldsymbol{u}_{coupled} = -\left(\boldsymbol{R}_{coupled} + \boldsymbol{R}_c\right) \tag{2.30}$$

where $\Delta\boldsymbol{u}$ is the solution increment vector and the global tangent stiffness matrices (**K**) and the global residual vectors (**R**) are formed from contributions of each body (subscript *coupled*) and the contact between the bodies (subscript *c*). For full derivation details please refer to Chung (2008).

An iterative process was used to determine the deformed configuration (**u**) until convergence

---

[1] www.cmiss.org

was achieved:

$$u_{n+1} = u_n + \Delta u \tag{2.31}$$

where subscript n represents the increment index.

2.7 Summary

In this background chapter, the motivation for modelling breast biomechanics was outlined. The boundary conditions and material properties of the breast were described, and the finite deformation theory and contact mechanics methods were summarised. In the subsequent chapters in this thesis, large deformations of the breast phantom and breast tissues were simulated using FEM implementation (CMISS) of finite deformation theory and contact mechanics. In Chapter 3, the compressive deformations of a breast shaped phantom under frictionless and frictional conditions were investigated. In Chapter 4, the deformations of the breasts due to prone to supine reorientation were simulated. Breast deformations due to mammographic compressions were subsequently explored in Chapter 6.

Chapter 3: Non-rigid image registration using finite element methods

Image registration techniques have been applied to help clinicians interpret breast images across different modalities. One method used to validate non-rigid registration algorithms makes use of customised finite element (FE) models to deform breast images. The warped and original images were registered with other non-rigid breast image registration algorithms, such as fluid registration, whose success or failure was determined by their ability to replicate the FE derived displacement fields (Tanner et al., 2009, Van de Sompel and Brady, 2008). In these studies the FE models were treated as a 'gold standard' and the accuracy of other methods were validated with respect to these models of the breasts.

However, such FE models of the breasts have not been systematically validated, so how can one justify their use as a gold standard for the analysis of other non-rigid registration algorithms?

In this chapter a three dimensional block matching method for validating FE-based non-rigid image registration techniques is presented. This block matching algorithm uses three dimensional imaging data to quantitatively assess model predictions on a localised basis over the entire three dimensional object. This comparison technique was validated using three dimensional imaging data of a breast shaped phantom subject to large compressions.

In order to predict breast deformations using FE models, various assumptions need to be

made regarding the tissue properties and the boundary conditions. Studies have found that the errors associated with such assumptions of the FE models of the breasts remain unresolved (Tanner et al., 2006). Previous quantitative validation of non-rigid registration of breast images *using finite element models* has focussed on the registration error of a small number of manually defined landmarks, the skin surface, or the overall accuracy of the image registration (Carter et al., 2009, Chung et al., 2008b, Han et al., 2011, Rajagopal et al., 2008b, Ruiter et al., 2006, Tanner et al., 2011). The non-linear nature of the breast deformations means that the choice of landmarks can potentially bias the analysis of the model predictions. It is therefore advantageous to consider similarity measures on a regional basis across the entire breast.

The accuracy of FE models on a localised basis was assessed using a three dimensional block matching approach as an error measure. The novelty of the method presented here is that, unlike previous applications of three dimensional block matching as an image registration algorithm, this is the first instance where the method is used as a localised accuracy measure. The resulting error vector field can then be used to infer how the FE model could be improved.

3.1   Block matching image comparison measure

3.1.1 Previous work

The block matching technique was first applied to medical images as a two dimensional non-rigid registration *tiles method* described by Periaswamy et al. (1999). In this work a multi-scale approach was used, where spline-pyramids of the target image and source image were created. At the lowest level of the pyramid the images were represented at the coarsest scale and in the successive levels up the pyramid, finer scales were used until the highest level, where the image was defined with its initial resolution.

An initial global rigid registration was performed on the lowest resolution representations of the target and source images using Fourier-based correlation (Reddy and Chatterji, 1996). The source image was then warped accordingly. An approximation of the Kaiser-Bessel function (Periaswamy et al., 1999) was used to window images to reduce wraparound errors in the frequency domain. The two dimensional target and source images were iteratively divided into four overlapping two dimensional region blocks (down to 8 pixel x 8 pixel

blocks). Corresponding two dimensional regions in the two images were rigidly registered with respect to each other, and a smooth molding map was generated by using thin-plate splines (Bookstein, 1989) with landmarks determined from the rigid transformation parameters. The registration at each of the iterations was performed by interpolating the molding map with cubic B-splines to warp the source image.

Subsequent work by Periaswamy and Farid (2003a) focussed on using local affine transformations to match the target image with the source image. In this work a three dimensional non-rigid registration algorithm was developed, where local affine parameters for each region were determined by the summation of the results of registration at different levels of the image pyramid. These parameters were interpolated to produce a smooth molding map based on splines. This was a similar approach to that taken by Rueckert et al. (1999), where a hierarchical series of B-spline-based free form deformation meshes were created over the whole image and the nodal parameters of each mesh were altered to maximise an image similarity measure.

3.1.2 Three dimensional block matching for analysis of finite element models

The block matching technique presented here is an extension of the two dimensional *tiles method* to three dimensions. This technique was used to compare image data across the entire breast volume to quantitatively assess non-rigid registration simulations on a regional basis. First, a global image comparison is made by using the squared normalised cross correlation (NCC^2) (see Chapter 2) to compare the FE-warped, resampled breast images with the clinical images of the different gravity-loaded configurations [Figure 3.1]. The practical meaning of this image similarity measure in context of breast image comparisons is briefly discussed in Section 4.4.2
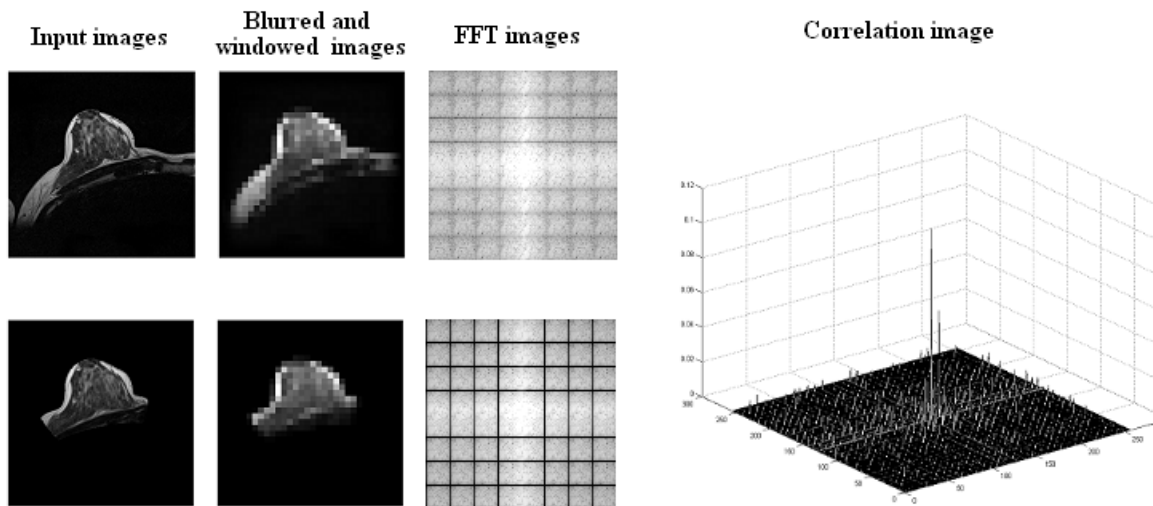
Figure 3.1: Determining optimal rigid translation between two three dimensional images. The two input images were blurred and windowed before being transformed into the frequency domain to find the optimal NCC^2 between the images.

A more detailed, regional variation in the image alignment error was then calculated using localised NCC^2. The source and target images were iteratively subdivided into 50% overlapping three dimensional sub-regions (to 5 mm × 5 mm × 5 mm volume) and the shift in the previous iteration that maximised the NCC^2 was used as the initial translation for the subsequent steps. Each sub-region was compared to an equivalent sub-region in the clinical image to find the optimal rigid translation for the model-warped sub-image. The initial translation of each sub-window was taken from interpolating the translations required for the larger sub-regions from the previous iteration. The localized correlation within these sub-windows was then used to find the local error vector of each sub-region [Figure 3.2].
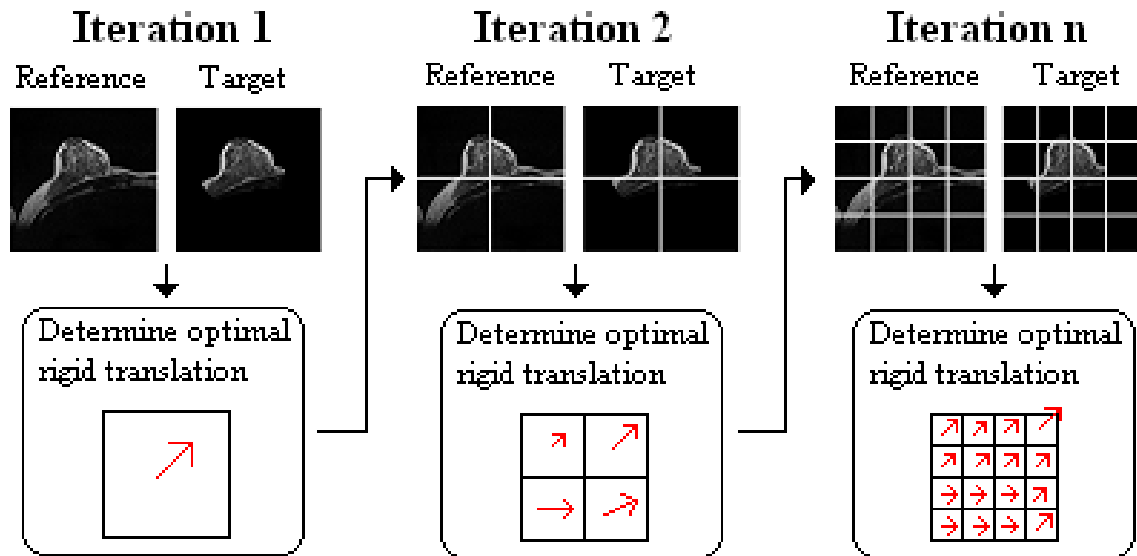
Figure 3.2: The optimal rigid translations were found for the sub-regions at each iteration, and were used as the initial translations for each of the sub-regions for the subsequent iterations.

Similar to the tiles method, the block matching algorithm is based on fast Fourier transforms (Lewis, 1995) of the images; therefore a cosine-tapered windowing function was applied to the images to reduce wraparound error in the frequency domain [Figure 3.1]. It was found that the high frequency noise present in the medical images had a detrimental effect on the accuracy of the comparison measure. A low pass filter was implemented to reduce the resolution of the images to deal with this issue. The coarsest resolution was used for the initial translation and the resolution was increased for each subsequent step. The un-blurred images were used for the final iteration.

The output from the three dimensional block matching technique was an error vector field, which describes the deformation error of each of the three dimensional regions in the image. These individual vectors associated with each region can be analysed statistically to quantitatively assess the accuracy of the image registration algorithms, including the FE model warping method. When block matching was used to assess the predictions of the FE models of the breasts, the distributions of the resulting errors within the FE models was used to identify the assumptions that cause the largest errors. Subsequent revisions of the assumptions for the FE models can lead to improvements in the accuracy and reliability of the models in simulating large-scale deformations of soft tissue mechanics.

3.2　Breast phantom studies

3.2.1 Breast phantom

A series of controlled experiments were carried out on a breast shaped phantom (Triple Modality Biopsy Training Phantom, Model 051, Computerized Imaging Reference Systems, Virginia, USA) to validate the use of the block matching algorithm as a measure of error for image registration techniques. The breast phantom is made with Zerdine® and has physical density similar to that of an average 50% glandular breast. The phantom is 500cc in volume, with a length of 12 cm, height of 9 cm and width of 10 cm [Figure 3.3]. It contains twelve lesions which are viewable under MRI, mammography and ultrasound. Six inclusions are cyst-like masses with diameters ranging from 3 mm to 10 mm and the remaining six are dense masses with diameters ranging from 2 mm to 8 mm.

(a)　　　　　　　　　　　　　　　　　　　　　　　　*(b)*
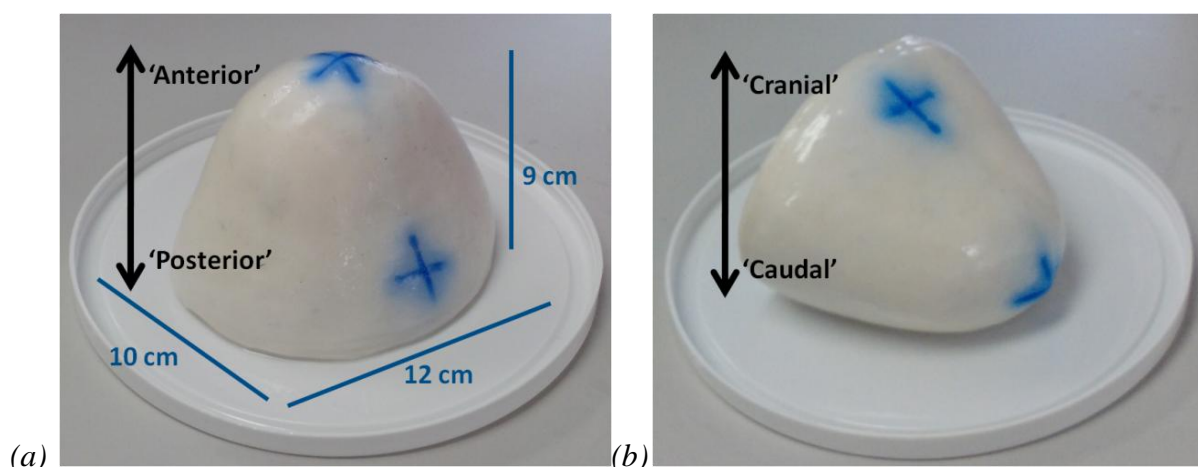
Figure 3.3: A breast shaped phantom was used in the validation of block matching as an accuracy measure for FE simulations of large deformations. (a) 'Anterior-posterior' and (b) 'cranial-caudal' directions were defined on the phantom as shown.

3.2.2 Compression device

A compression device was designed and, using Perspex plates, built which allowed the breast phantom to be compressed to five levels. The compression plates were made of thick (12 mm) Perspex so they would not flex but rather remain completely rigid when compressing the breast phantom. The top compression plate rotated about a pivot point set at 280 mm from the front end of the device. Non-ferrous copper pins were used to hold the top compression

plate down during a scan. The top and bottom compression plates were milled so that plates of varying thicknesses (2 mm, 6 mm, 10 mm, 12 mm and 20mm) could be inserted, resulting in a range of separation distances: 44 mm, 52 mm, 54 mm, 58 mm and 62 mm [Figure 3.4]. These compression distances were chosen as they fall within the compression thickness range (12 mm to 90 mm) of X-ray mammograms of the breasts (Helvie et al., 1994, Klein et al., 1997, Poulos et al., 2003). Experiments were performed with and without lubrication (mineral oil) between the compression plates and the phantom, which allowed the predictions of the phantom model to be tested across a wide range of strain distributions.

(a) *(b)*
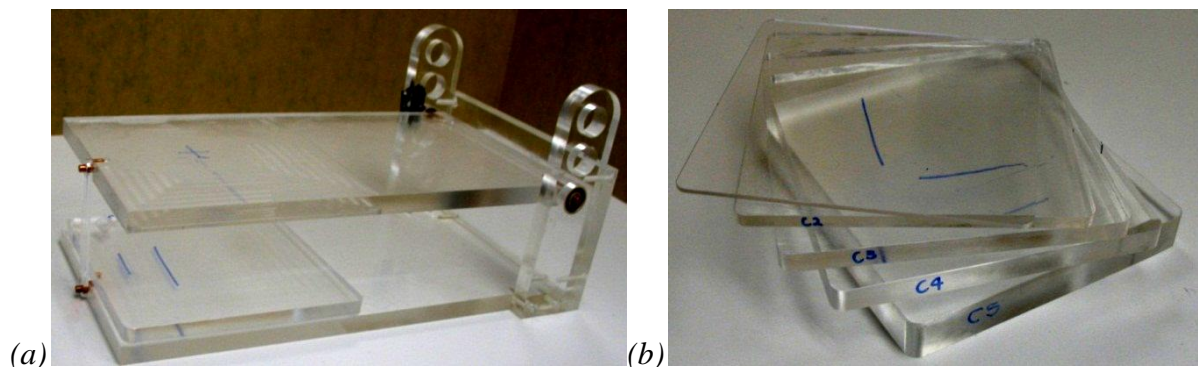
Figure 3.4: (a) Perspex compression device with (b) insert plates of varying thicknesses to allow for five levels of compression.

3.2.3 Compression experiments

The phantom was compressed in the 'anterior-posterior' (AP) and 'cranial-caudal' (CC) directions. For ease of reference, the orientations of the phantom have been described in terms of the body coordinate system shown in Figure 3.3. For AP compressions, where the anterior-posterior direction was aligned with the direction of gravity, the phantom was imaged before and during 24%, 29%, 34%, 37% and 46% compressions [Figure 3.5a]. For CC compressions, where the CC direction was aligned with the gravity vector, the phantom was imaged before and during the following levels of compressions: 27%, 32%, 37%, 39% and 49% [Figure 3.5b].

3.2.4 Image acquisition

MR images, with a T_1 weighted FL3D pulse sequence, were acquired of the breast phantom in the uncompressed state and under different states of compression, using a 1.5T MR scanner (MAGNETOM Avanto, Siemens, Munich, Germany). The MR image dimensions

were 512 pixel x 512 pixel with a 350 mm x 350 mm field of view with 176 slices with 0.75 mm slice thickness [Figure 3.5].

a)   0%   24%   29%   34%   37%   46%

b)   0%   27%   32%   37%   39%   49%
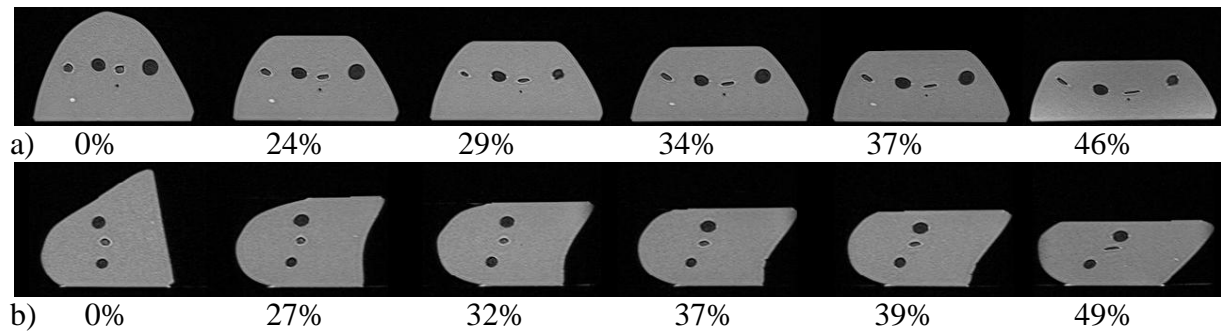
Figure 3.5: Two dimensional MR slices of the breast phantom before and during different levels of compression in a) AP and b) CC directions.

3.3   Homogeneous finite element simulations of the phantom

3.3.1 Uncompressed mesh

The surface of the phantom and the inclusions were automatically segmented from the MRI data using a simple intensity threshold method. The segmentations of the surface of the uncompressed breast phantom were used to create FE models of the uncompressed breast phantom in the AP and CC directions as shown in Figure 3.6 (see Appendix A for convergence analysis of the model). A brief introduction to using finite elements to implement finite elasticity was given in Chapter 2. In this section the specific details of the FE models used to describe the breast shaped phantom were provided.
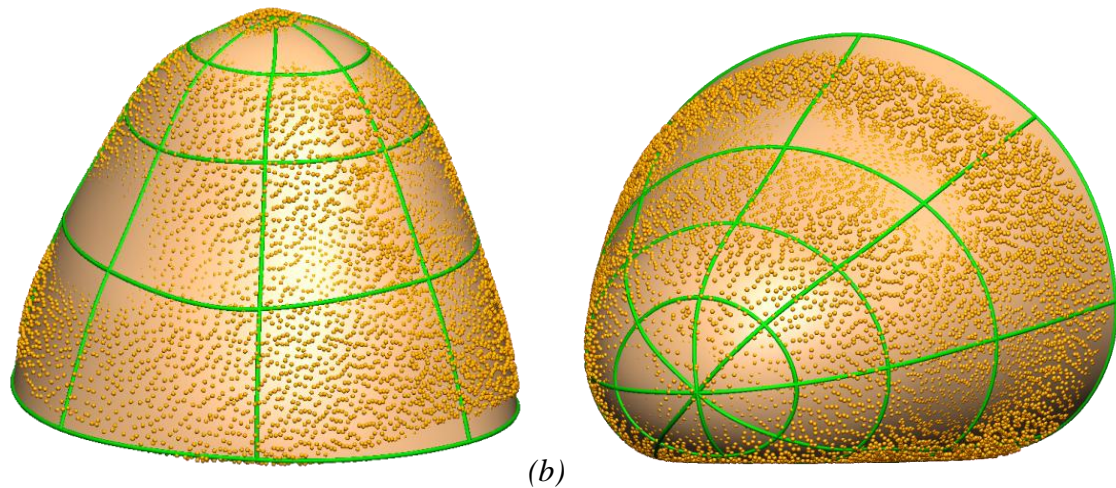
(a)   *(b)*

Figure 3.6: The segmented surface of the breast phantom were used to create FE models of (a) the AP uncompressed phantom (RMS error=0.53 mm) and (b) CC uncompressed phantom (RMS error=0.58 mm).

3.3.2 Unloaded reference mesh

Throughout the imaging, the breast phantom was subjected to gravity loading. The models created from the uncompressed data therefore represent deformed states of the phantom. In order to accurately predict the non-linear deformations of the breast phantom under the large levels of compression, the stress-free unloaded state is required. Using the methods developed by Rajagopal et al. (2008a), the unloaded state was directly calculated from the known gravity deformed states of the phantom, and used as the reference state for subsequent simulations.

The stress-free state should ideally be the same for both the AP and CC models when the gravity loads are removed. However, as the phantom was positioned on the bottom compression plate during image acquisition, there are contact forces in addition to the gravity load. Currently the software CMISS used to calculate the stress-free configuration is unable to account for contact constraints. Instead of calculating the true unloaded reference shape and then using contact mechanics to predict the shape of the phantom due to contact with the bottom plate, kinematic constraints on the nodal values and derivatives were used on the breast phantom's contact surface to maintain the contact with the bottom plate and predict the gravity unloaded shape of the breast. As the area of contact between the breast phantom and the bottom compression plate is different for the AP and CC gravity loading cases, two gravity unloaded models were calculated [Figure 3.7].
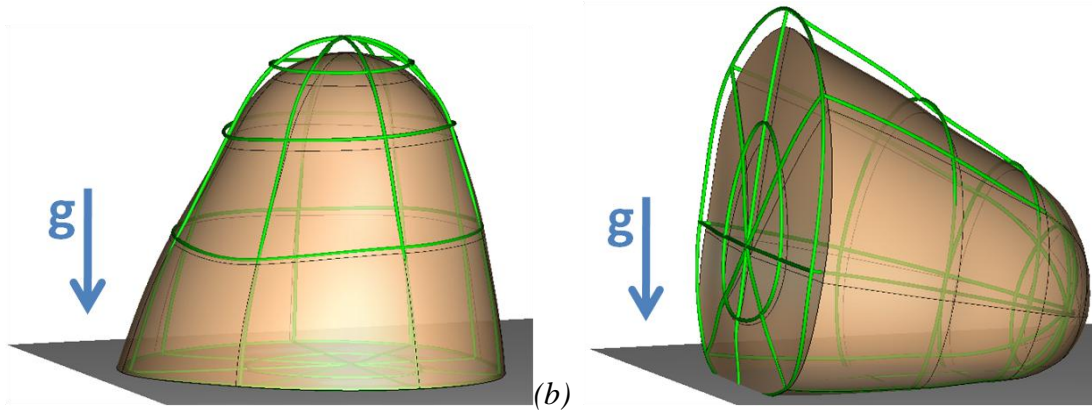
Figure 3.7: The uncompressed mesh (brown) with the corresponding estimate of the unloaded reference state (green outline) for gravity loading (g) along the (a) AP and (b) CC directions. Nodes were fixed on the contact surface of the uncompressed phantom with the bottom compression plate (gray) during the calculation of the unloaded reference state.

3.3.3 Compressed mesh

At the start of the compression simulations, gravity loads were applied to the unloaded mesh before the top compression plate was rotated down onto the breast phantom, allowing the effect of gravity to be accounted for throughout the compression simulations [Figure 3.8].
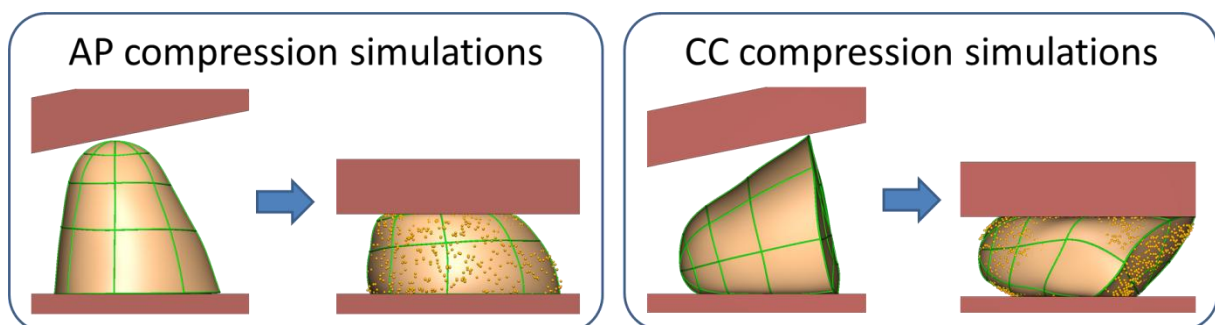
Figure 3.8: The AP and CC compressions were simulated by rotating the top compression plate down onto the breast phantom. The accuracy of the deformations was assessed by calculating the Euclidean distances of the projections of the experimental compressed data points (gold) to the surfaces of the compressed models.

Contact mechanics constraints were applied in these compression simulations. The kinematic constraints previously applied to calculate the gravity unloaded configuration were removed and the deformed shape of the breast phantom was calculated using contact constraints with the top and bottom plates. The simulations were set up as coupled contact mechanics

problems, with the breast phantom chosen as the slave mesh and the rigid compression plates chosen as the master mesh (see Chapter 2).

The CC experiments were carried out with lubrication, reducing the friction between the contact surfaces. Therefore, frictionless contact mechanics was used during simulations (see Section 2.5.1). Since the phantom was covered in mineral oil, it was able to slip as the compression was applied. During the experiments, the phantom was held in position to prevent it from moving off the compression device. Correspondingly during the FE simulations, realistic fixed displacement boundary conditions were applied to the model to prevent it from sliding off the compression plates during the simulation [Figure 3.9].
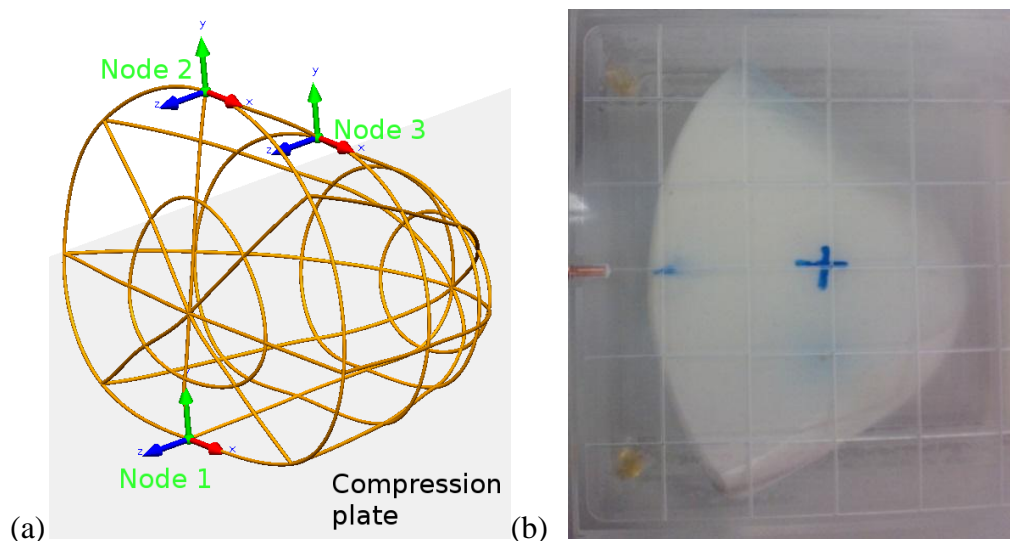
Figure 3.9: (a) During simulation of the frictionless compression in the CC direction, fixed displacement boundary conditions were used to prevent the phantom from sliding off the compression device. Node 1 was fixed in the x (red) and z (blue) directions, and Nodes 2 and 3 were fixed in the x (red) direction. (b) These boundary conditions correspond to what was observed during compression of the breast phantom in the CC direction.

The AP experiments were carried out without lubrication; therefore frictional forces resisted slippage between the breast phantom and the compression device. Thus, in contrast to the CC simulations, nodal locations not fixed during the simulations. Frictional contact mechanics were used to model the interactions between the contact plates and the phantom (see Section 2.5.2).

3.3.4 Parameter estimation

Cranial-caudal frictionless homogeneous model optimisation

The CC compression experiments, where the direction of the compression on the breast phantom aligned with its CC direction, were conducted using lubrication. Frictionless contact mechanics was used to simulate these deformations with the FE model (see Chapter2). To minimise the penetration between the master and slave meshes while still allowing for numerical convergence, the penalty parameter for contact stiffness, C_N, was set as 50 MPa/m for the breast phantom simulations.

The FE models were based on an isotropic, homogeneous, and incompressible mechanical response, as defined by the neo-Hookean constitutive relation: $W=C_1(I_1-3)$, where I_1 is the first principal invariant of the right Cauchy-Green deformation tensor and C_1 is the stiffness parameter.

The stiffness of the breast phantom was unknown; therefore the material stiffness parameter, C_1, was estimated using the FE model. The optimisation was performed using a nonlinear least-squares algorithm (*lsqnonlin*) in the Matlab optimization toolbox. After each of the CC compression simulations, the deformed surfaces were compared against the segmentations of the phantom surfaces from the MR images of the corresponding compression level. The data points that represented the actual deformed surface of the breast phantom were projected onto the nearest point on the surface of the deformed biomechanical mesh. The Euclidean distance of the projection was then calculated and used to define the objective function used in optimization (Babarenda Gamage et al., 2011). The objective function, Ø, for the optimisation was defined by the combination of these distances as defined in Eq. 3.1:

$$\emptyset = \sum_{Comp=1}^{M} \sum_{i=1}^{N_{Comp}} ||Z_{i\,Comp}||^2 \qquad (3.1)$$

where $||Z_{i\,Comp}||^2$ was the Euclidean distance between the data point and its projection on the surface, M was the number of compression models considered in the optimisation, and N_{Comp} was the number of data points segmented from the breast phantom surfaces for each of the compressed MR images.

In this case, an initial estimate for the material stiffness was supplied to the mechanics models, $C_1^{intial}=1$ kPa. Upper and lower bounds for the material stiffness parameter were set

to be 0.5 kPa and 20 kPa, respectively. These values were determined by performing a parameter sweep for the highest level of compression in the CC direction (46%), and then comparing the FE simulation with the clinical images. A converged result was reached when the change in the parameter was less than the specified tolerance. The optimal material stiffness value, C_1, for the CC simulations was found to be 1.21 kPa.

Anterior-posterior frictional homogeneous model optimisation

The AP compression experiments, where the direction of the compression on the breast phantom aligned with its AP direction, were conducted without any lubrication. Therefore, frictional contact mechanics was used to simulate these deformations with the FE model (see Section 2.5.2). For the AP frictional simulations, additional contact parameters, such as the penalty for slip in the tangential (frictional) direction and the frictional coefficient, needed to be defined. As for the CC simulations, the penalty parameter for contact stiffness, C_N was set as 50 MPa/m. These parameters were properties of the problem and helped to determine whether the breast phantom sticks or slips on the contact surface with the compression plates during mechanics simulations.

The dimensionless frictional coefficient (μ) was set to 0.95 throughout the simulations for AP compressions. A simple experiment was conducted to estimate the static frictional coefficient between the compression plates and the breast phantom. The frictional coefficient, μ is defined as:

$$\mu = \frac{T}{N} \qquad (3.2)$$

where T is the tangential force magnitude and N is the normal force magnitude at the point at which there is slip.

One of the compression plates was set at an incline and the breast phantom was placed on top. The level of inclination was increased until the phantom began to slip. The gravity force can be decomposed into the normal and tangential components with respect to the contact surface using the angle of inclination. Using trigonometry, the frictional coefficient, μ could thus be calculated as the tangent of the angle of incline as illustrated in Figure 3.10:
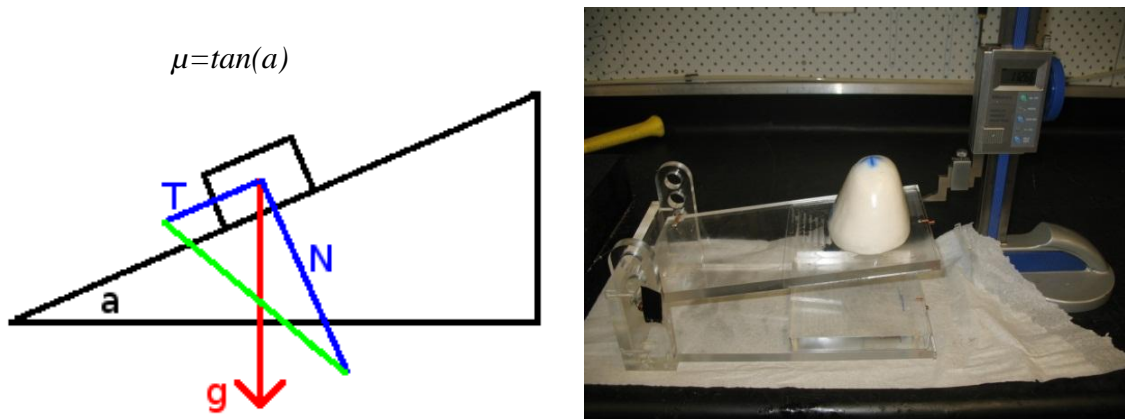
Figure 3.10: Estimation of the frictional coefficient between the breast phantom and compression plates without lubrication. The incline of the compression plate was increased until the breast phantom began to slip. The angle of incline (a) was then used to calculate the frictional coefficient.

During the simulations, the deformation of the breast phantom under frictional AP compression depends on both the material stiffness (C_1) and the tangent stiffness (C_T) parameters. During CC compression simulations, the contact constraints were modelled as frictionless and the tangential contact stiffness, C_T, can be considered to be zero i.e. the model is always in the slip state. The same phantom was used for both the AP frictional and the CC frictionless experiments, thus the material stiffness, C_1, applies to both sets of simulations. The homogeneous material stiffness, C_1, needed to be re-determined with the addition of the frictional AP simulations. The tangent stiffness, C_T, (using the frictional AP experiments) and the material stiffness, C_1, (using both sets of experiments) were estimated using the optimisation framework shown in Figure 3.11. The initial estimate for the material stiffness was set as the previous optimised value from the CC frictionless simulations. The normal (frictionless) component of the contact traction, C_N, was set to be 50 MPa, and the optimal value for the tangential (frictional) component of the contact traction, C_T, was found to be 29 kPa/m, while the homogeneous material stiffness, C_1, was 1.07 kPa.
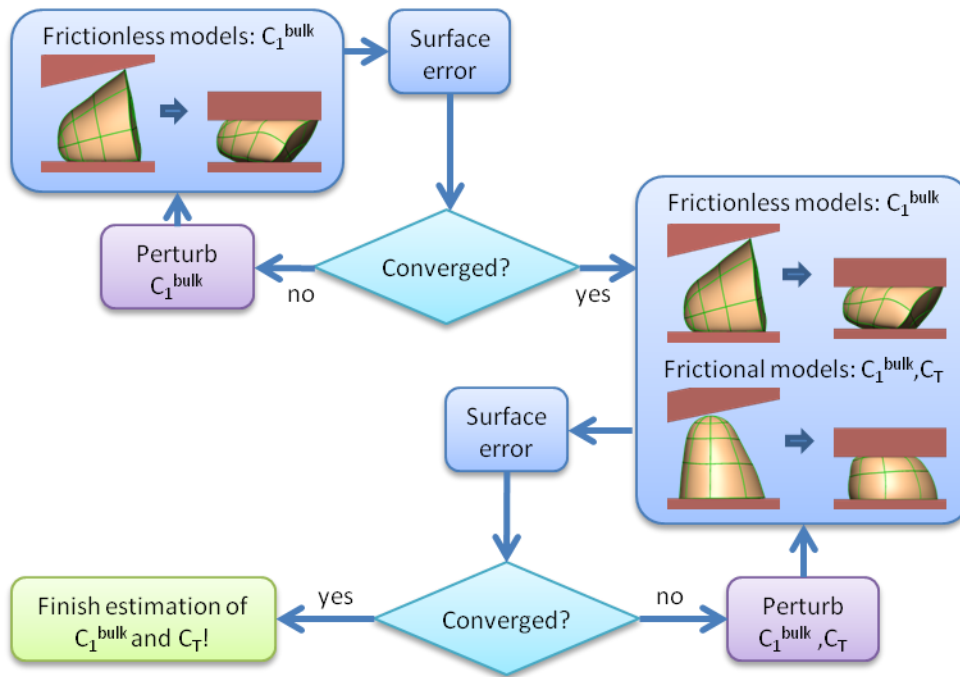
Figure 3.11: Framework for homogeneous material and contact stiffness optimisation

3.3.5 Image warping

In order to assess the predictions of the FE model, the simulated results needed to be compared against the experimental data. In the above optimisation, the error was measured as the distance between the surface of the model predictions and the surface of the breast phantom in the experiments. However, in addition to the surface, the MR images also contain information about the internal structures of the phantom. This extra information can be used to assess the accuracy of the model. However, first the MR images of the uncompressed states needed to be deformed in accordance with the model predictions.

The voxels associated with the model were identified and their material point locations (in FE co-ordinates) with respect to the model were defined. These material point locations in the deformed model were mapped back into geometric space to identify the deformed locations of the voxels. When an image is deformed and the voxel locations are altered, the pixel locations may no longer be regular. In order to compare the model warped images directly with the experimental images, tri-linear interpolation was used to re-sample the voxel intensity values at regular grid locations. The AP uncompressed and CC uncompressed images were embedded and warped using the FE predictions for the various levels of compression using Matlab. The FE-warped images and the experimental images were then compared using the block matching comparison method (Section 3.1).

3.4 Heterogeneous finite element simulations of the phantom

For the initial compression simulations described in the previous sections, it was assumed that the breast phantom was made of only one type of material. However, this was clearly not the case as the breast phantom contains twelve inclusions, of which six are cystic masses and the remaining six are solid masses with correspondingly lower or higher material stiffnesses, respectively, compared to the bulk material of the phantom. As there were no features in the homogeneous bulk material of the phantom, the areas with the largest error in the block matching analysis for the homogeneous FE breast phantom model corresponded with the surfaces of the breast phantom and the inclusions. In this section, the heterogeneous mechanical properties of the inclusions inside the phantom were investigated. As the bulk material composes more than 99% of the volume of the breast phantom, the material stiffness for this region and the tied contact parameter were fixed to the previous estimates from the homogeneous optimisation (C_I=1.07 kPa, C_T=29 kPa/m), during optimisation of the soft and stiff inclusion material properties. Since the largest changes in the shape of the 12 inclusions occur with the highest levels of compression in AP (46%) and CC (49%) directions, only these models were used in the optimisation. The methods used to extend the phantom model can also be applied to the breast, which contains structures such as adipose, fibro-glandular, muscle, and in some cases tumourous tissues, all of which have different mechanical properties.

3.4.1 Segmentations

The breast phantom was imaged under MRI in the AP and CC uncompressed positions. A simple intensity threshold method was sufficient to distinguish the inclusions from bulk material in the MR images. The inclusions were separated into cystic or solid groups based on the deformed shapes of the inclusions in the compressed images [Figure 3.12]. As the solid materials have a higher stiffness than the cystic masses and the bulk material, the six structures that maintained their shape were classed as solid inclusions, whereas the structures which changed from ellipsoid shapes to more disc-like structures were classed as cystic masses.
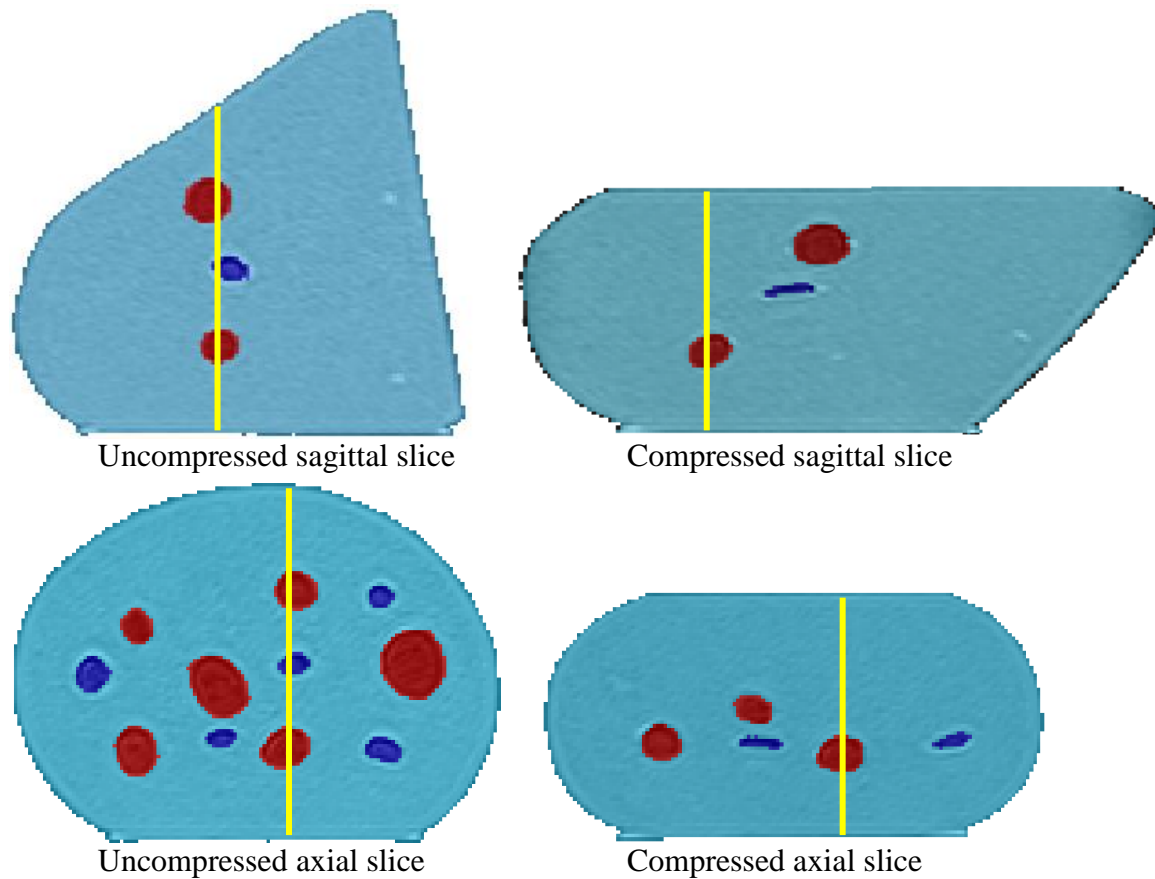
Figure 3.12: The breast phantom structures were classed as bulk (light blue), solid inclusions (red) and cystic inclusions (dark blue) by considering the actual deformations of the breast phantom inclusions before and after compression. Sagittal slices and axial slices are shown with the yellow lines indicating the location of the corresponding slice.

For application to breast models, different imaging modalities can reveal information about the stiffness characteristics of abnormal breast tissues. Cystic masses, with lower stiffnesses in comparison to normal breast tissue, are typically confirmed using ultrasound (Ikeda, 2011). In contrast malignant breast cancers, which tend to be much stiffer than normal breast tissues, typically have an increased level of vascularisation, resulting in distinctive enhancement curves in contrast enhanced MR studies (Warren and Coulthard, 2002).

3.4.2 Heterogeneous stiffness fields

The FE mesh was made up of large elements (average volume: 3313 mm^3) described with cubic Hermite shape functions, while the solid and cystic inclusions ranged from 2 mm to 10 mm in diameter. In order to describe the material heterogeneity of the breast phantom, stiffness values were assigned to the Gauss points inside the elements. The material stiffness

for each of the Gauss points was calculated as a linear combination of the stiffnesses of each of the three materials, as:

$$C_1^{GP} = w_{bulk}^{GP} C_1^{bulk} + w_{solid}^{GP} C_1^{solid} + w_{cysts}^{GP} C_1^{cysts} \qquad (3.3)$$

where w_{bulk}^{GP}, w_{solid}^{GP} and w_{cysts}^{GP} were the weightings of the bulk, solid and cystic materials, respectively, at each Gauss point.

The weightings can be calculated using either a closest point Voronoi method or a field-based method [Figure 3.14]. In the Voronoi method, every voxel inside each element was assigned to the closest Gauss point inside that same element. The weightings were the proportion of the voxel labels for the various material types assigned to each Gauss point [Figure 3.13].

(a)   *(b)*
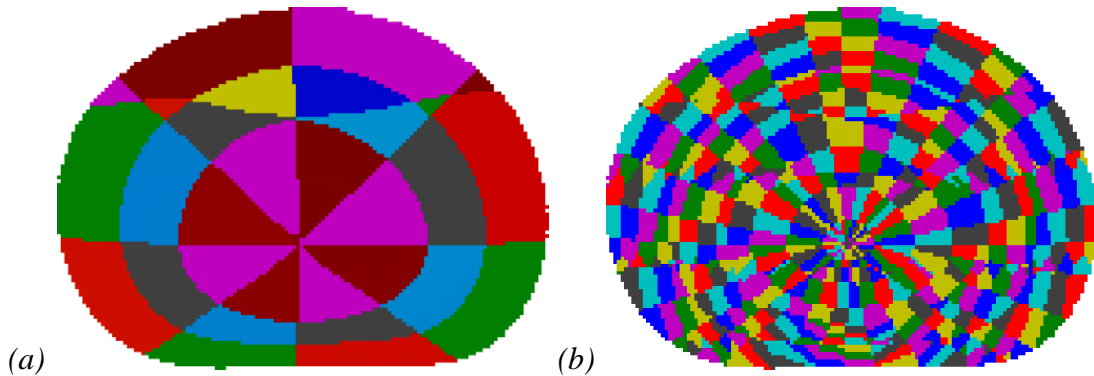
Figure 3.13: Using the Voronoi method to account for the heterogeneous stiffness field. (a) The model was subdivided into elements (different colours represent the different elements). (b) The voxels in each element were then assigned to the closest Gauss point in that element (different colours represent the Gauss point assignment). Each voxel now has two labels: Gauss point and material type.

In the field-based method, the segmentation was split up into three binary masks – one for each label (bulk, solid and cysts). These masks were used to set up three fields inside the FE mesh, where each field was assigned values of ones or zeros corresponding to the mask. These binary fields distributed across the mesh were approximated with tri-cubic Hermite basis functions. The fields were then interpolated at each individual Gauss point within each element, to determine the weightings of the different materials.

This field approximation can result in negative weighting values at some of the Gauss points, which corresponds to a negative stiffness value, which cannot be simulated with the FEM software (CMISS). The upper limit of the material stiffness which is permissible for the

material (e.g. solid) was calculated by rearranging Eq. 3.3:

$$0 = w_{bulk}^i C_1^{bulk} + w_{solid}^i C_1^{solid} + w_{cysts}^i C_1^{cysts}$$

$$C_1^{solid} = \frac{-w_{bulk}^i C_1^{bulk} - w_{cysts}^i C_1^{cysts}}{w_{solid}^i}, \text{ where } w_{solid}^i = \min(w_{solid}^{GP})$$

(3.4)

The advantage of the field-based method is that the same interpolation scheme is used to define both the geometry and the mechanical properties of the breast phantom at the nodal locations. The ability of the model to deform depends on the stiffness field which is generated based on the interpolations of the segmentations.

Cubic Hermite basis functions that were used to describe both the geometric and segmentation fields enforces C^1 continuity, although the segmentation field is discontinuous. This interpolation of the discontinuous segmentation field with cubic Hermite shape functions has the effect of blurring the effective stiffness field as shown in Figure 3.14. Disallowing negative weightings resulted in a limited effective range of stiffness values that can be assigned to the Gauss points. This limitation could be dealt with by increasing the resolution of the mesh, however refining the mesh correspondingly increases the computational expense of solving the mechanics simulations.

In contrast, the Voronoi method for assigning the weightings of the mechanical properties of the mesh lacks the compatibility with the geometric degrees of freedom of the mesh. However, it provides greater fidelity to the segmentations of the breast phantom images, and allows for a larger range of effective stiffness values that can be assigned to the Gauss points to represent the material types [Figure 3.14]. Therefore, the Voronoi method was used to assign the weighting values to calculate the stiffness values of each Gauss point.
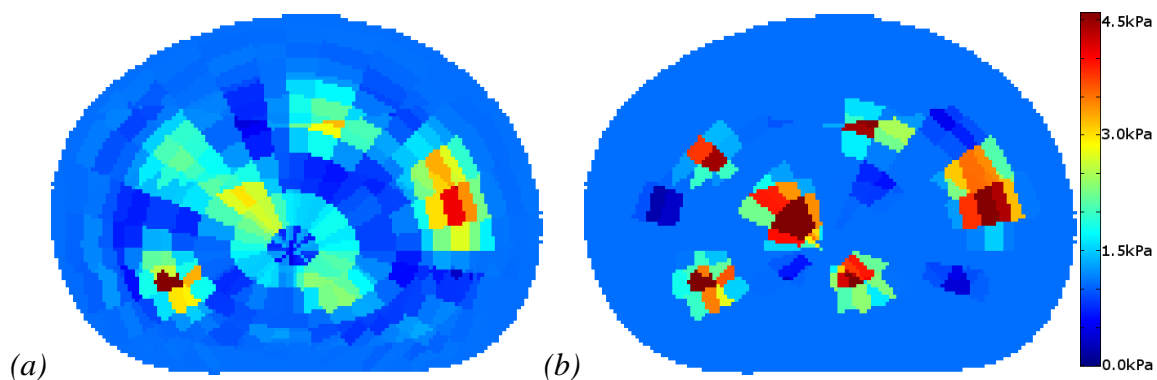
(a)   (b)
Figure 3.14: Distribution of stiffness values in an axial slice of the CC uncompressed model where the weightings were determined by using (a) the field-based method and (b) using the Voronoi method.

The methods discussed in this section approximated the heterogeneous nature of the breast phantom by varying the material stiffness across elements in the mesh at a Gauss point resolution. This had the effect of blurring the distinction between the structures as shown in Figure 3.12 and Figure 3.14. In addition, these methods neglect the interface conditions across the boundaries of the structures. However, the aim of this thesis centres on FE models of the breast, whereas the phantom studies were used to validate techniques, prior to application to breast models.

Unlike the homogeneous C_1 estimation, the block matching method was used as the metric for the optimisation of the solid and cystic inclusions in the breast phantom. It was found that the optimal values for the solid and cystic inclusions were 6.73 kPa and 0.04 kPa, respectively.

3.5 Comparison of different biomechanical models of the breast phantom

3.5.1. Modelling error quantification

The FE model predictions were quantitatively assessed on a localised basis over the entire phantom by comparing the FEM-warped images against the experimental MR images of the compressed phantom using the block matching comparison method [Figure 3.15]. In the phantom there are twelve inclusions, which were distinct under MRI. The inclusions were tracked in order to assess the overall internal deformation in addition to the surface deformation of the breast phantom.
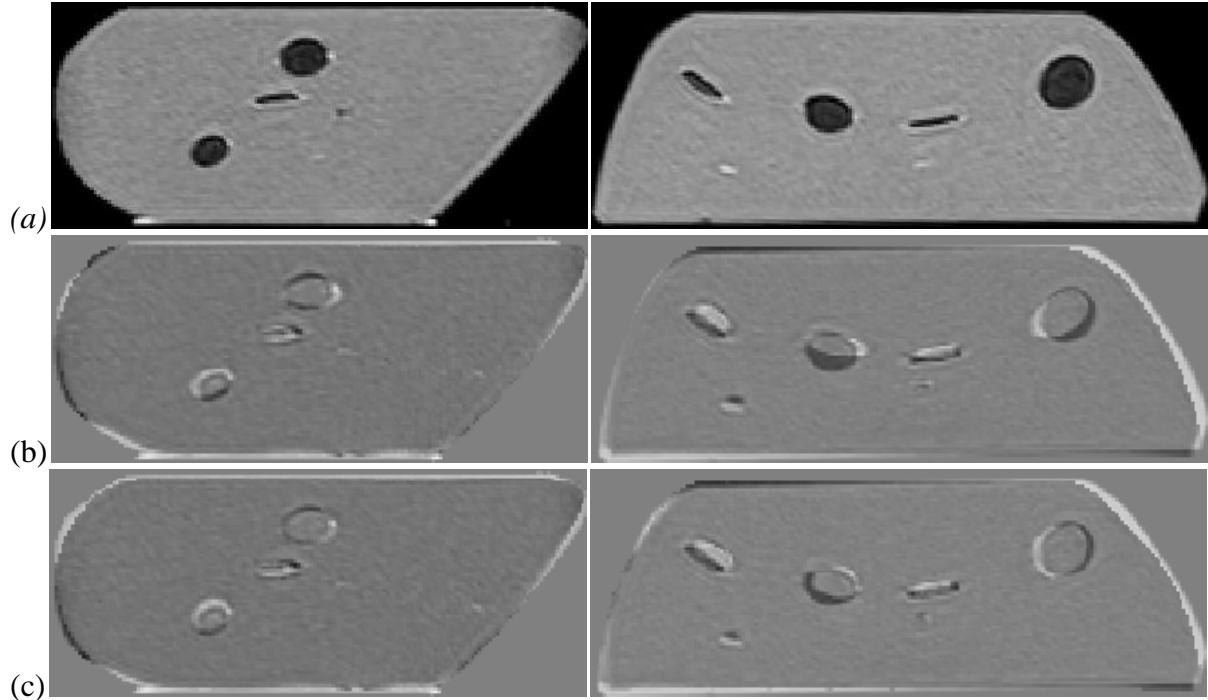
Figure 3.15: (a) Ground truth images of the breast phantom under AP and CC compression loads were acquired in the MRI scanner. The deformations of (b) homogeneous and (c) heterogeneous FE models were used to warp the uncompressed MR images. The differences between the model warped images and the ground truth images are shown.

Feature tracking error measures, which have typically been used to assess image registration algorithms (Carter et al., 2008, Chung et al., 2008b, Klein et al., 2009, Rajagopal et al., 2010, Ruiter et al., 2006, Tanner et al., 2011) were also analysed to assess the error of the breast phantom image registration using the FE models. The target registration errors of the centroid distance (*CENT*) of the inclusions between the model-warped images and the experimental images of the compressed phantom were calculated. The volume overlap (Dice coefficient, *DICE*) and surface distance (symmetric mean absolute distance, *SMAD*) were evaluated for each of the 12 inclusions:

$$DICE = \frac{2|A \cap B|}{|A| + |B|} \times 100 \tag{3.5}$$

$$SMAD = \frac{1}{n_a + n_b}\left(\sum_{n_a}|d_i^{ab}| + \sum_{n_b}|d_i^{ba}|\right) \tag{3.6}$$

where *A, B* are the inclusions segmented from the target and warped images, respectively, d_i^{ab} is the minimum distance between the ith surface voxel on *A* and the surface voxels on *B*, and n_a, n_b are the number of surface voxels for the inclusions in *A* and *B* respectively.

In addition to the landmark-based methods, the block matching method was used to give an overall assessment of the accuracy of the model deformations. The errors for the inclusions can be identified by using masks with the block matching method. By comparing the results of the block matching approach with the feature tracking methods, the use of the block matching method to assess the deformations of the FE models was validated.

Initially homogeneous FE models of the breast phantom were used to simulate compression in the AP and CC directions. Based on the results from the homogeneous model block matching error evaluations, the model was improved by adding varying stiffness fields to take into account the heterogeneous structures inside the breast phantom (Section 3.4). The stiffness values for the different structures were estimated by comparing the model predictions of the most compressed states in both AP and CC directions against the experimental data, using the block matching as the objective function.

3.5.2. Statistical analysis

Means and standard errors for the landmark and block matching measures of accuracies were calculated for the homogeneous and heterogeneous biomechanical models of the breast phantom. After confirming normality (Shapiro-Wilk test) and equal variance (Levene's test) of the landmark data, the two models were assessed using paired t-tests for each of the landmark-based error measures (CENT, SMAD and DICE) using the statistical package R^2. The p value to reject normality and/or equal variance was set at $p \leq 0.05$. Paired t-tests were used to assess the landmark-based methods as the same lesions were measured in both models. While an independent t-test was used to assess the block matching error measures for the two models.

3.5.3. Results

Paired t-tests between the homogeneous and heterogeneous FE models for the landmark-based measures indicated that there were significant differences between them for two of the landmark-based measures (CENT: p<0.01; SMAD: p<0.01), while comparisons using the volume overlap measure indicated that there were no significant differences between the models (DICE: p=0.3). The independent t-test indicated that there were significant

---

[2] www.r-project.org

differences between the models when the block matching method was used for analysis (p<0.001). Comparisons between the homogeneous and heterogeneous models for the CENT, SMAD, and block matching error measures indicated that taking into account the heterogeneous nature of the breast phantom improved the prediction of the FE simulations as shown in Table 1.

Table 1: A FE-based method was used to warp the three dimensional clinical images of the uncompressed breast phantom to match images of the breast phantom under 46% anterior-posterior (AP) and 49% cranial-caudal (CC) compression loads. The 12 individual masses of the breast phantom were used to calculate the mean and standard errors (SE) of the centroid distance (CENT), surface distance (SMAD) and volume overlap (DICE) errors of the frictionless and frictional models (n=24). A block matching method was also used to assess the overall accuracy of the models.

	CENT (mm)	SMAD (mm)	DICE (%)	Block Matching (mm)
Homogeneous simulations	2.71 ± 0.20	1.20 ± 0.07	55.6 ± 3.7	2.85 ± 0.01 (n=45134)
Heterogeneous simulations	1.84 ± 0.14	0.97 ± 0.06	58.2 ± 3.9	2.75 ± 0.01 (n=45184)

3.6   Remarks

The purpose of this chapter was two-fold: firstly the block matching method was validated as an error measure for image registration of medical images of the breast phantom; and secondly methods for estimating heterogeneous material properties were developed. In Table 1 it can be seen that using block matching as an error measure for non-rigid registration of large deformations of soft tissues was consistent with what was observed using landmark-based methods. The main advantage of the block matching method for assessing error over feature tracking is that it can automatically determine the regional errors over the entire three dimensional volume (Lee et al., 2010a). For breast images, feature tracking error measures are typically based on manually defined landmarks, and are hence subjective (Carter et al., 2008, Chung et al., 2008b, Rajagopal et al., 2008b, Ruiter et al., 2006, Tanner et al., 2011).

Different measures were used to investigate the accuracy of the homogeneous and heterogeneous models in predicting the compressive deformations of the breast phantom. Statistical analysis of the homogeneous and heterogeneous models using the volume overlap (DICE) of the inclusions as an error measure indicated that there were no significant differences between the FE models (p=0.3). However, the other error measures (and visual inspection) indicated that the heterogeneous models were significantly more accurate than the

homogeneous models (p<0.01). This result reflects the insensitivity of the volume overlap measure to the difference between the models. This difference lies in the material stiffnesses of the inclusions, which make up a relatively small part of the breast phantom. The relative locations of the inclusions in the breast phantom remained the same across the two models, though the shape differed, with the heterogeneous model having greater fidelity to the actual compressions, as shown in Figure 3.15 and Table 1.

The block matching method was used as a metric to estimate the heterogeneous material parameters. The block matching method presented in this chapter provides regional information about the accuracy of the simulated deformations over the whole breast. The FE models can thus be systematically improved by identifying the regions with the largest errors and adjusting the assumptions of the model accordingly. Statistical analysis was on both feature-based error measures and the block matching comparisons for the highest compressed models in the AP and CC directions and it was found the heterogeneous models performed significantly better than the homogeneous models in predicting the internal deformations of the breast phantom.

In the rest of this work, the block matching non-rigid registration algorithm was used as an error measure where the deformation field between the FE-warped image and the target image was analysed to assess the accuracy of the FE-warping. Other image registration algorithms such as fluid registration (Crum et al., 2005) or the B-spline-based free-form deformation (FFD) method (Rueckert et al., 1999) can be used instead of the block matching approach described here, to assess localised error of the biomechanical model. However, as shown in the results above, the simpler block matching approach is sufficient to capture the regional inaccuracies of a FE model.

In summary, methods for assessing the accuracy of the three dimensional model on a regional basis and estimating the heterogeneous material properties were validated. These techniques were then applied to FE models of the breast simulating prone to supine reorientation in Chapter 4.

Chapter 4: Finite element-based non-rigid registration of breast MR images

4.1 Motivation

Contrast-enhanced (CE) MRI (prone orientation), X-ray mammograms (CC or MLO compressed with patient in an upright posture), and ultrasound (supine orientation) can provide complementary information for the diagnosis of breast cancer. MR images of the breast are typically acquired with the patient lying in a prone position, with the breasts hanging pendulously within a MR breast coil to improve the signal-to-noise ratio by providing greater image contrast and minimising motion artefacts from breathing or other patient movements (Warren and Coulthard, 2002). However, surgery and ultrasound are usually performed with the patient lying in a supine orientation. Accurate collocation of tumours inside the breasts across different gravity loading conditions would therefore be a useful clinical tool.

CE-MRI relies on the enhancement characteristics of normal and abnormal breast tissues to identify malignant tumours in the breasts. Invasive breast cancers are characterised by increased vascularisation, and therefore tend to enhance faster and to a greater degree than normal fibroglandular tissue. Due to the dynamic nature of the image acquisition, patient motion can be problematic in the interpretation of images. Different transformations have been applied to breast images to account for motion-based artefacts; early work on registering

dynamic breast MR images focussed on the global alignment on the images using affine or rigid transformations (Zuo et al., 1996). However, breast tissues are soft and thus undergo non-linear deformations that are generally not well represented by rigid or affine transformations. Studies have acknowledged this limitation and used non-rigid registration techniques such as free-form deformations (FFD) based on B-spline warping (Rohlfing et al., 2003, Rueckert et al., 1999), thin-plate splines (TPS) (Wirth et al., 2002), and fluid registration (Crum et al., 2005) to capture the local deformations of the soft breast tissues.

Rueckert et al. (1999) proposed a method for the non-rigid registration of prone breast MR images using free-form deformations. The global motion of the breast was captured using an affine transformation; this was then followed by FFD based on B-splines to model the local deformations of the breast tissues. A penalty term was used to maintain the smoothness of the transformation. They showed that this algorithm was much better at capturing the deformations of the breast tissues than simple rigid or affine transformation of the images. However, non-rigid registration techniques can alter the volume of the breast tissues and features that are highlighted by the contrast agent, such as tumours, often shrink substantially during the non-rigid registration process. Tanner et al. (2000) and Rohlfing et al. (2003) augmented the Rueckert approach to include a volume-preserving constraint to address this problem. This demonstrated the need for image registration algorithms to take into account the physical behaviour of the breast tissues. Finite element (FE) models have therefore been used to provide physically realistic constraints on aligning sequential breast imaging studies (Krol et al., 2006, Roose et al., 2008, Schnabel et al., 2003, Tanner et al., 2000, Unlu et al., 2010).

Finite element (FE) models have also been developed to simulate the deformations of the breasts for different gravity loading conditions. One of the main advantages of FE models over other non-rigid registration methods is that it restricts the motion to physically plausible deformations. It would be clinically beneficial to be able to track the internal deformations of the breast tissues between the prone, supine, and upright gravity loaded states, as well as the compressed state because different imaging modalities require the breasts to be subject to different loading conditions. In this chapter, the ability of the biomechanical model to predict the deformations of the breast tissues for prone to supine reorientation was validated using MR images of volunteers.

4.2 Previous finite element breast models for gravity loading simulations

FE models have been developed to simulate larger deformations of the breast tissues: (i) under compression loads (Alonzo-Proulx et al., 2010, Azar et al., 2001, Chung et al., 2008b, Hipwell et al., 2007, Galea and Howe, 2003, Pathmanathan et al., 2008, Reynolds et al., 2011, Ruiter et al., 2006, Samani et al., 2001, Schnabel et al., 2003, Shih et al., 2010, Tanner et al., 2011); or (ii) due to changes in the gravity loading state (Carter et al., 2009, del Palomar et al., 2008, Pathmanathan et al., 2008, Rajagopal, 2007, Yu-Neifert, 1995). In this chapter, a biomechanical modelling framework was tested using prone to supine reorientation studies. For further discussion on compression models, please refer to Chapter 6.

Yu-Neifert (1995) developed one of the earliest FE models of the breasts, for which the geometry of the model was based on stereographic images of the breast surface. The supine orientation was used as the reference state, and gravity loads were applied to the mesh in the caudal and anterior bodily directions to simulate the upright and prone orientations, respectively. Since the composition of the fibroglandular and adipose tissues within the breasts were not captured, their model assumed that the breast tissues were composed entirely of adipose tissue, with a linearly elastic skin layer. A major limitation of the Yu-Niefert model was that only surface information was used to create and validate the model. Pathmanathan et al. (2008) developed an improved model that was created from prone three dimensional MR images. The images captured the internal structures of the breast, and this information was used to develop a heterogeneous (adipose, fibroglandular, and skin) model of the breast that was used to simulate the supine orientation and mammographic compressions from a prone orientation.

Surgery and ultrasound are typically performed on breasts while the patient lies in a supine orientation. However, satisfactory outcomes for breast augmentation or reduction surgeries depend upon the morphology of the breast tissues in the upright position. Del Palomar et al. (2008) investigated the deformations of the breast tissues from supine to upright orientations. CT images were acquired of two patients lying in the supine orientation, and the tissues (adipose, fibroglandular, muscle, and bone) were segmented using a marching cubes algorithm. FE models of the breasts were then constructed from the segmentations of the adipose and fibroglandular tissues, and the global stiffness of the breast tissues was

determined based on the properties of the respective tissues within the model using the neo-Hookean material relation.

Limitations

1. In a number of studies, either the prone or supine orientations were used as the biomechanical reference state (Yu-Neifert, 1995, del Palomar et al., 2008, Carter et al., 2008). One problem with this is that the material relations used in the analysis assume that the reference state is unloaded and stress-free, which is inappropriate as the breast tissues are subject to gravity loading in the prone and supine orientations. A well defined (e.g. stress-free) reference state is required in order to accurately predict the deformation of the breast due to applied loads. The importance of the biomechanical unloaded reference state was investigated in gravity loading simulations by Rajagopal et al. (2007a, 2008a). The unloaded reference state can be calculated using a 'reverse method', where the conventional finite elasticity equations are reformulated in terms of the known deformed (prone) configuration (Rajagopal et al., 2007a). This method was experimentally validated using a silicon gel beam under gravity loading (Rajagopal et al., 2007a), before being applied to breast FE models (Rajagopal et al., 2008a). In this chapter, this 'reverse method' was used to estimate the biomechanical unloaded reference state directly from the prone orientation, prior to supine simulations. This is in contrast to studies where gravity is applied twice, first in the direction opposite to the actual gravity vector, then in the direction corresponding to the subsequent deformation (upright or supine) (Carter et al., 2008, del Palomar et al., 2008).

2. Major limitations of the work described above on breast deformations due to gravity are that either no quantitative validation was performed (Pathmanathan et al., 2004, 2008) or that it was based only upon the skin surface deformations of the breast models (Yu-Neifert, 1995; del Palomar et al., 2008). Using the most anterior point on the skin surface for validation of the model is insufficient (Yu-Neifert, 1995), as simpler transformations (such as the affine transform) could give comparable results. However, it has been shown that affine transforms are unable to accurately represent the deformations of the breast in sequential prone imaging studies (Rueckert et al., 1999). Del Palomar et al. (2008) validated their models with a greater number of points; although these points were all located at the skin surface.

3. This limitation was addressed in other studies where the accuracy of the internal

deformations of the breast tissues in FE model simulations of gravity loading were assessed using MR images of the breast in different orientations with respect to the direction of gravity (Carter et al., 2008, 2009, Han et al., 2011, Rajagopal et al., 2007a, 2008b). In these studies, skin surface deformations, and manually tracked internal landmarks, were used to assess the accuracy of the FE model predictions.

4. In this chapter, the block matching method (described in Section 3.1) was used to automatically assess the regional accuracy of the FE models throughout the entire breast. Based on the block matching results, the biomechanical breast models for simulating prone to supine reorientation were systematically improved by modifying the boundary conditions and assumptions about the breast model composition. This is an improvement over methods that have manually defined landmarks (Carter et al., 2008, 2009, Han et al., 2011, Rajagopal et al., 2007a, 2008b), as the distribution of the error vectors varies over the volume of the breast. Moreover, the choice of landmarks presents a subjective (and potentially biased) view of the model accuracy.

Boundary conditions

Within the literature, boundary conditions at the posterior nodes of the breast mesh have traditionally been: fixed in one/all directions (Rajagopal et al., 2007, 2008a, 2008b, Shih et al., 2010, del Palomar et al., 2008); displaced according to non-rigid registration deformation fields (Tanner et al., 2006, Carter et al., 2006); displaced at a linear rate dependent on the distance from the sternum (Carter et al., 2008); or have used contact constraints with the rib surface (Chung et al., 2008, Reynolds et al., 2010, Han et al., 2011).

In validation studies of biomechanical models of the breast, MR images were acquired before and during compression (Ruiter et al., 2006, 2008, Chung et al., 2008) or between different gravity loading states (Rajagopal et al., 2008, Carter et al., 2008, 2009, del Palomar et al., 2008). Carter et al. (2008) estimated linear displacement of the nodes on the posterior surface, based on manual identification of corresponding features close to the pectoral muscle in MR images of the breast under prone and supine gravity loading. In other studies, non-rigid image registration techniques, such as fluid registration (Carter et al., 2009) or FFD based on B-splines (Tanner et al., 2006), were used to align images of the breast under different loads. Subsequently FE models were used to simulate the deformations of the breast across the different loading conditions, while applying nodal constraints on the surfaces of the FE breast models, based on the non-rigid registration deformation fields. A limitation of

these methods is that they require a-priori three dimensional images of the deformed state (compressed or supine), which are typically not acquired in the clinical setting. This chapter focuses on the accuracy of biomechanical models in predicting prone to supine deformations without the use of supine images. The accuracy of the model predictions was quantitatively assessed to compare the use of fixed-displacement against contact boundary constraints. Contact constraints have previously been applied to FE breast models for both compression (Chung et al., 2008; Reynolds et al., 2010) and prone to supine reorientation (Han et al., 2011) studies. A limitation of these studies was that the parameters describing the contact constraints were arbitrarily defined. In this chapter, methods for estimating the contact constraints on the rib surface of the breast model were developed.

Mechanical properties

As previously discussed in Chapter 2, a wide range of material stiffness values have been reported for adipose and fibroglandular tissues in the breasts, with the level of pre-compression of the breast tissue having influence on the stress-strain relationship (Wellman, 1999; Krouskop et al., 2003). However, this was likely a consequence of their use of linear models, which do not accurately represent the material properties of the breast tissues. Hyperelastic material relations, such as the neo-Hookean model, have therefore been used to approximate mechanical behaviour of the breast (Babarenda Gamage et al., 2011).

The mechanical properties of the breast tissues have been represented as either homogeneous or heterogeneous fields in FE models. Isotropic and transversely-isotropic (with greater stiffness in the AP direction) material relations have also been considered for compression simulations (Tanner et al., 2011). However, these models used the prone gravity loaded configuration as the reference state in the simulations. Anisotropic material properties will need to be investigated for cases when an estimation of the biomechanical unloaded reference state is calculated using the 'reverse method'.

In this chapter, the validity of using more realistic boundary conditions on the rib surface and incorporating information about the heterogeneous nature of the breast into the FE models were investigated by examining the sensitivity of the model predictions. Initially, a homogenous model with zero-displacement boundary conditions on the rib surface was used to simulate the deformations of the breast tissues for prone to supine reorientation. Subsequently contact constraints were applied to the rib surface, before heterogeneity in the stiffness of the various tissues (adipose, fibroglandular, and muscle) was incorporated. The

accuracy of the biomechanical models of the breasts was assessed using a three dimensional block matching method (see Chapter 3).

4.3   Breast MR imaging studies of volunteers

To investigate the use of different boundary conditions and mechanical property assumptions on the FE model accuracy, MRI studies were performed on two healthy volunteers who were scanned using a 1.5T MR scanner (MAGNETOM Avanto, Siemens, Munich, Germany). Written informed consent was obtained from both volunteers prior to participation in the study, which was approved by the local ethics committee[3]. Volunteer 1 was a multiparous woman (who had given birth to two children) of 35 years with a body mass index (BMI) of 22.1, who was lactating at the time of imaging. Volunteer 2 was a nulliparous woman (never having given birth) of 21 years with a BMI of 22.8. T_2-weighted images of the breasts were acquired with the volunteers positioned both in prone and supine orientations [Figure 4.1].

Although the standard sequence for breast MR imaging is T_1, the T_2 imaging protocol used in these studies is more appropriate for studies investigating tissue heterogeneity in the breasts (Section 4.6), as it allows for greater distinction between the adipose and fibro-glandular tissues. The image dimensions were 512 pixel x 512 pixel spanning a 350 mm x 350 mm field of view with 52 and 60 slices of 2.5 mm thickness for Volunteers 1 and 2, respectively.

---

[3] The University of Auckland Human Participants Ethics Committee (reference: 2006/149)
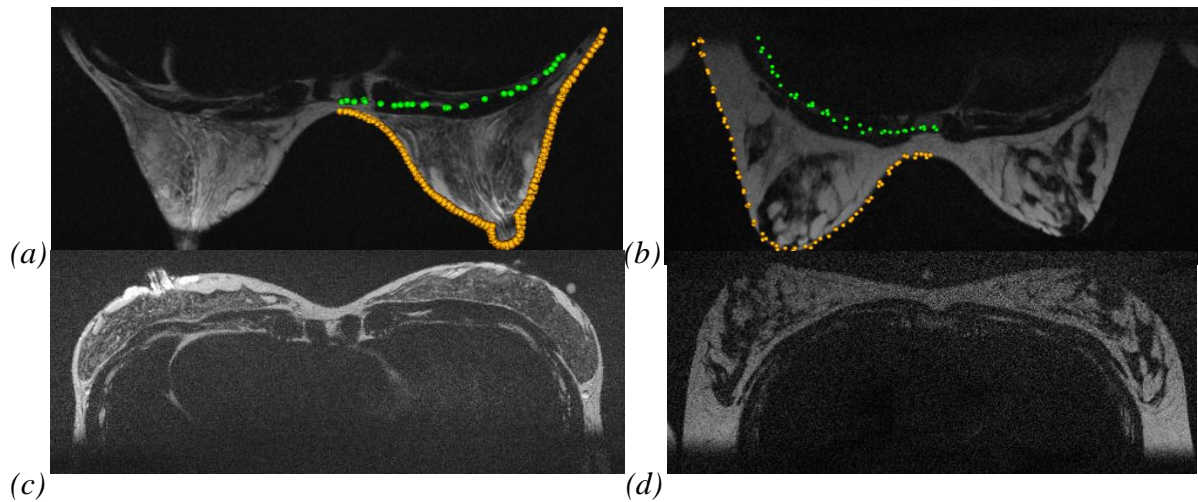
Figure 4.1: Clinical MR images of the prone breast were used to create personalised FE models for (a) Volunteer 1 and (b) Volunteer 2 using the skin (gold points) and rib (green points) segmentations. In order to validate the model deformations, clinical supine images were also obtained for (c) Volunteer 1 and (d) Volunteer 2.

4.4 Biophysical breast models with fixed boundary conditions

4.4.1 Model setup

The skin and rib surfaces in the MRI data for the volunteers in the prone positions were manually segmented and used to create personalised models for FEM-based registration [Figure 4.2]. The model customisation was performed by fitting the anterior surface of a generic mesh to the skin data cloud and the posterior surface of the mesh to the rib data.

The breast mesh extended from the mid-sagittal plane (sternum) around the front of the torso up to the mid-coronal plane (axilla) [Figure 4.2]. The axilla edge of the mesh was chosen to be relatively remote from the bulk of the breast tissues, so that any assumptions on the boundary conditions applied to the axilla edge of the breast mesh would not greatly influence the accuracy of the breast deformations.

The FE models for the breasts were based on an isotropic, homogeneous, and incompressible mechanical response, described by the neo-Hookean constitutive equation: $W=C_1(I_1-3)$, where I_1 is the first principal invariant of the right Cauchy-Green deformation tensor and C_1 is the stiffness parameter. See Appendix A for convergence analysis of the models.

(a)   *(b)*
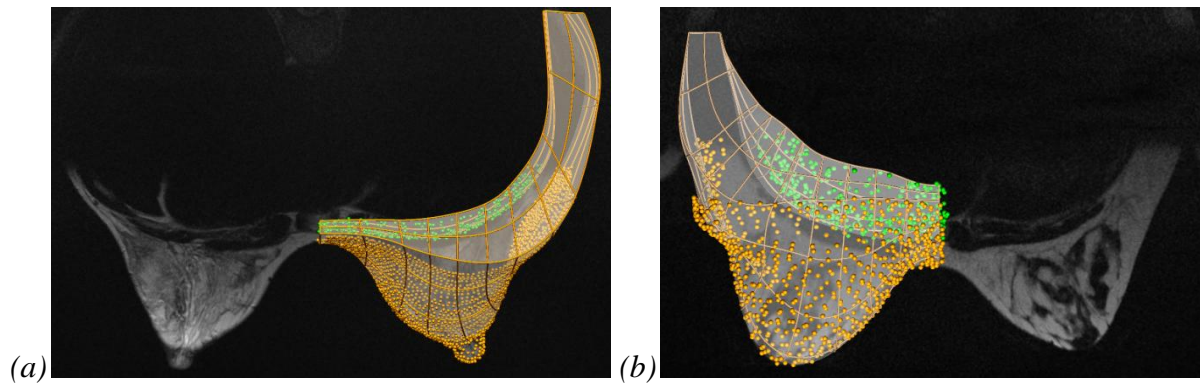
Figure 4.2: A generic mesh was fitted to the skin (gold) and rib (green) segmentations of the prone data to customise the mesh to (a) Volunteer 1 (Skin RMSE=1.8 mm, Rib RMSE=0.9 mm) and (b) Volunteer 2 (Skin RMSE=1.9 mm, Rib RMSE=1.5 mm).

4.4.2 Boundary conditions

The deformation of the breast tissues is of primary interest; therefore the breast tissues were isolated from the rest of the torso and shoulder during the creation of the FE mesh. Kinematic boundary conditions were enforced to account for the constraints that these structures normally place on the deformation of the breast tissues.

The breast tissues and pectoral muscles were initially assumed to be firmly attached to the chest for simulating the prone to supine reorientation. Based on this assumption, zero-displacement boundary conditions were applied to the nodes on the rib surfaces of the FE models. Kinematic boundary conditions were also applied to the medial, axial, cranial, and caudal surfaces of the breast mesh to ensure realistic deformations as described in Figure 4.3. In addition to fixing the nodes on the rib surface, some skin surface nodes on the cranial edge of the model were also fixed to account for the attachment of the breast tissues to the shoulder [Figure 4.3].

Unlike some previously published similar studies (Tanner et al., 2006, Carter et al., 2008), additional displacements were not prescribed on the skin surface of the FE-warped prone mesh to ensure that it matched the clinical supine data. Although this approach may provide a better match between the skin surface of the FE-warped and clinical images, this disregards the physics of the situation, as these displacements introduce unbalanced and unrealistic forces at the free (skin) surface of the FE mesh. By maintaining fidelity to the physical situation of the breast tissues, biomechanical breast models can be used to predict the deformations of breast tissues given known boundary conditions and where a-priori three

dimensional information of the breast deformations are unknown.
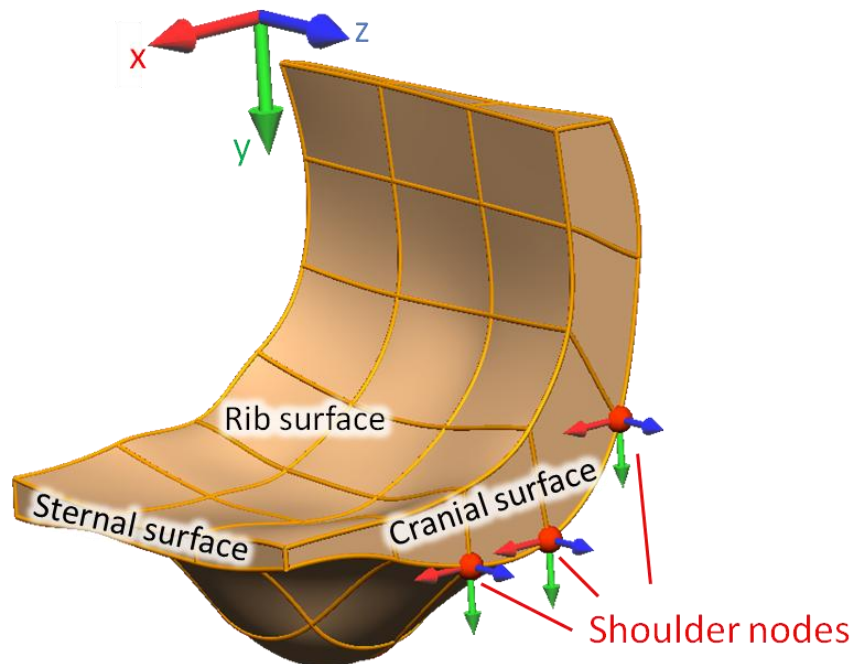
Figure 4.3: During prone to supine reorientation simulations, kinematic boundary conditions were applied to the breast models to mimic the torso constraints. The nodes associated with the shoulder (red) and rib surface were fixed in all directions. The sternum and axilla surfaces were fixed in the x (red) and y (green) directions, respectively, while the cranial and caudal surfaces were fixed in the z (blue) direction. The nodal derivatives on these five surfaces were also fixed to prevent unrealistic bulging at the edges of the model.

4.4.3 Mechanics simulations

FE implementation of finite deformation elasticity was used to simulate the large deformations that the breast tissues underwent between imaging. In both the prone and supine orientations, the breasts are subject to gravity loading. In order to model the deformation of the breast tissues from one loading state (prone) to another (supine), the mechanics reference state needs to be determined. In many studies, the shape of the breasts under gravity loading was taken as the reference state (Yu-Neifert, 1995, Carter et al., 2006, 2008, del Palomar et al., 2008). However, the constitutive relations used in these models assume zero-stress and zero-strain in the reference state.

In this thesis, the biomechanical reference state of the breast tissues was predicted by deforming the FE models of the prone breast in accordance with the large deformation

elasticity theory. The method used to estimate the unloaded state of the breast tissues from the loaded configuration (prone) was based on redefining the knowns (to be the loaded state) and unknowns (to be the unloaded reference state) in the finite elasticity equations (Rajagopal et al., 2007). The estimated biomechanical unloaded reference state was then deformed into the supine position through the application of gravity loading towards the posterior direction [Figure 4.4].
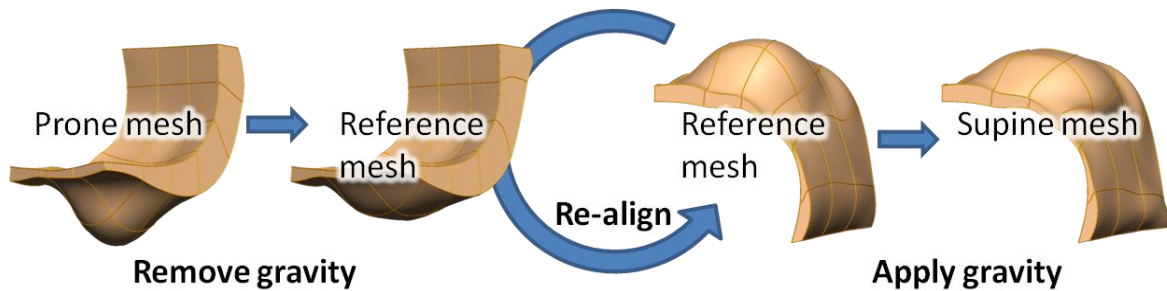
Figure 4.4: Estimation of the unloaded reference state from the prone orientation by removing the effect of gravity. The supine orientation was then simulated by applying gravity to the estimate of the unloaded state of the breasts.

4.4.4 Stiffness estimation

The breasts for the two volunteers were initially modelled using a homogeneous stiffness field. The stiffness of the breast tissues is dependent on several factors, including the ratio of adipose to fibroglandular tissues, which is different for each individual. Therefore, there is a need to customise not only the geometry of the FE model, but also the mechanical properties of the breast tissues to each individual. In Chapter 3, an optimisation framework was introduced to determine the unknown material stiffnesses for a breast phantom. A similar method was applied here to customise the mechanical properties of the breast tissues [Figure 4.5].

The prone FE models were first created from the segmentations of the skin and rib surfaces of the prone MR images. Breast deformations were then modelled using gravitational body forces to simulate the 'unloading' of the breast and then the reorientation from prone to supine. The shape of the anterior surface of the biomechanical model of the breast was compared to segmentations of the skin surface from the clinical supine images. In order to minimise the computational time required for the optimisation routine, a low resolution FE model (975 geometric solution degrees of freedom) was first used to determine initial

estimates of the stiffness values, which were subsequently used for a high resolution FE model (4606 geometric solution degrees of freedom) optimisation. The homogeneous material stiffnesses (C_1) were found to be 75 Pa and 122 Pa for Volunteers 1 and 2, respectively, which is similar to previously reported material stiffness values of 80 Pa and 130 Pa (where the shoulder nodes were not fixed) (Rajagopal et al., 2008).
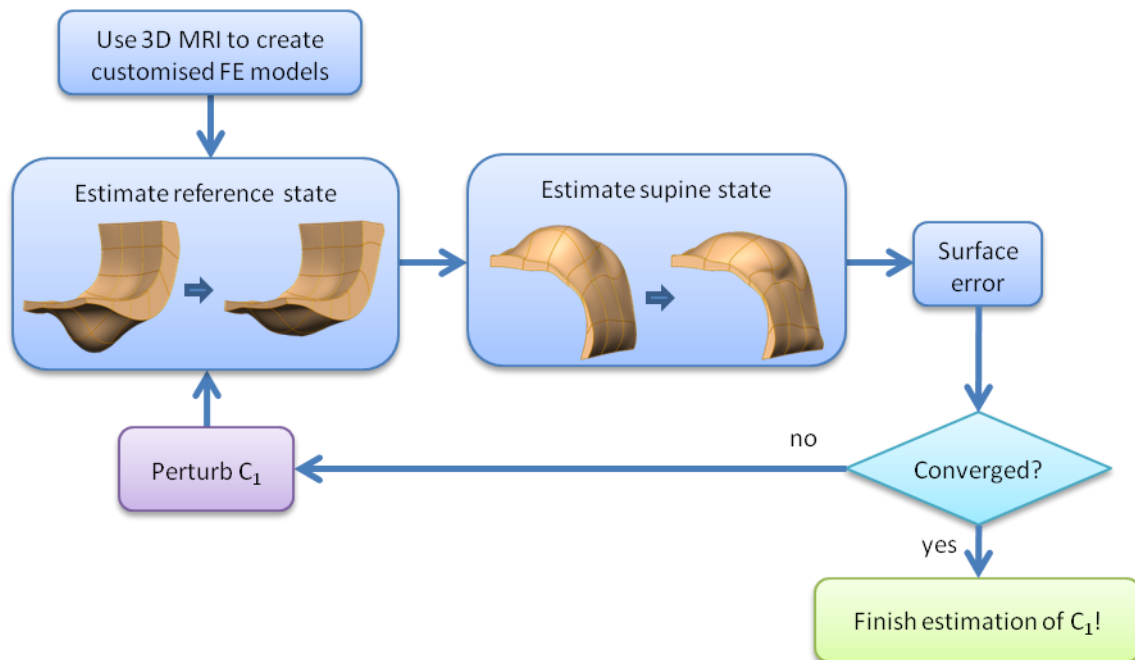
Figure 4.5: Framework for estimating the material stiffness, C_1.

4.5 Biophysical breast models using tied contact constraints

4.5.1 Model setup

In the previous section, the breast tissues were assumed to be fixed to the pectoral muscles and rib cage. However, this is a simplification of the physiological interactions between the breast tissues and the chest wall. It is known that the breast tissues are attached to the chest wall via Cooper's ligaments and the retromammary bursa, which allow mobility of the breast across the chest wall during prone to supine reorientation (Sabel, 2009).

To account for the sliding, contact constraints were used to represent the interaction between the breast and ribs. This allowed the biomechanical models to be used for *predictions* where the three dimensional deformations of the breast tissues are not known. To simulate the contact interactions between the breast ('slave' mesh) and the chest wall, for the supine

simulations, a new mesh representing the rib surface ('master' mesh) needed to be developed [Figure 4.6].

The FEM software, CMISS only allows contact mechanics constraints to be imposed in the forward simulation from the unloaded reference state to the supine orientation. Thus, for the prone to unloaded reference state simulations, the breast tissues were fixed to the rib surface. For the forward simulations from the unloaded reference state to the supine orientation, the kinematic constraints on the rib surface were removed to allow for the relative sliding. In addition, the nodes on the axilla edge were mapped to a single degree of freedom to maintain a uniform degree of sliding at this extremity, instead of being fixed [Figure 4.6].
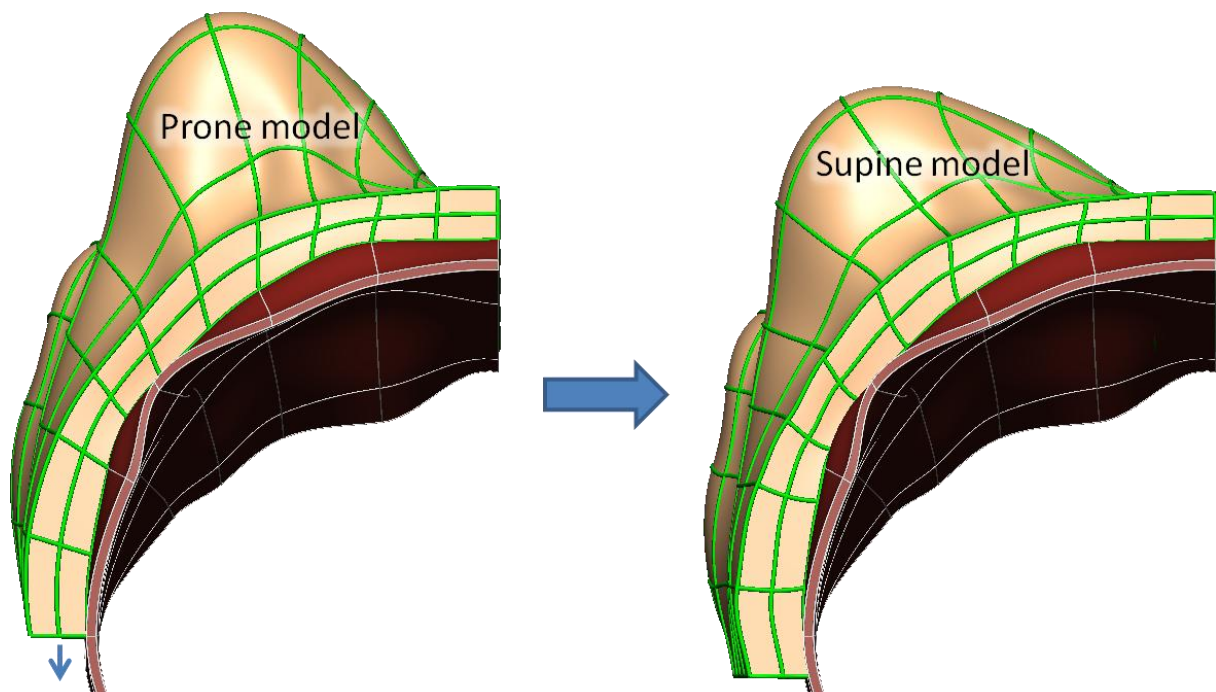
Figure 4.6: Inferior view of a new rigid rib (master) mesh (red) was developed for contact simulations between the unloaded reference and supine simulations. Constraints on the breast (slave) mesh (light brown) were imposed to allow sliding on the ribs.

4.5.2 Stiffness estimation

As discussed in Chapter 2, fixed displacement boundary conditions can be simulated with high tied contact stiffness, while lowering the tied contact stiffness results in behaviour that gradually approaches the frictionless sliding case. To minimise the penetration between the rib mesh and breast meshes, while still allowing for numerical convergence, the penalty parameter, C_N, for the normal component of the contact traction was set as 2 MPa/m. The

tangential component of the contact pressure was determined from the tangential gap function and a tied contact penalty value, C_T, estimation of which is discussed below.

The deformation of the breast tissues depends on both the tangential contact penalty value, C_T, and the material stiffness parameter, C_I. The influences of these two parameters were investigated using block matching as the error measure (see Chapter 3). In the previous section, the homogeneous material stiffnesses of the breast models were estimated using an objective function based on the root-mean-square error (RMSE) of the skin surface projections. For this error measure, the segmented skin surface data points of the supine states were projected onto the nearest point on the surface of the deformed breast models. However, the internal deformations were also of interest. As this method does not even track the material points on the skin surface, its sensitivity is not sufficient for the estimation of C_I and C_T. A hierarchical scheme was used for the block matching comparison, where the images were subdivided into successively smaller overlapping three dimensional blocks at each iteration, and the local translation required for each sub-region was identified using the NCC^2 image similarity measure. The practical meaning of the NCC^2 value, as applied to the three dimensional breast MR images, was previously investigated using the following comparisons: autocorrelation ($NCC^2=1$); prone MR vs. noise ($NCC^2=0.005$); prone MR images acquired on different days ($NCC^2=0.86$) (Lee et al., 2008).

To simultaneously estimate both the material stiffness, C_I, and contact stiffness, C_T, the block matching method over the whole model was used as the objective function. However, it was found that a unique solution for the two parameters did not exist, as in the parameter space the block matching metric did not converge to a minimum point, but rather along a flat valley [Figure 4.7], indicating trade-off behaviour between the two parameters. When the material stiffness, C_I, was reduced, the breast model deformed more due to its softer nature. There was also greater motion when the contact stiffness, C_T, was reduced, as the breast model can slide more on the rib surface, resulting in a greater level of deformation, as shown in Figure 4.8. Thus these two parameter variations can result in similar effects, causing a trade-off of the parameters C_I and C_T for a given target deformation.
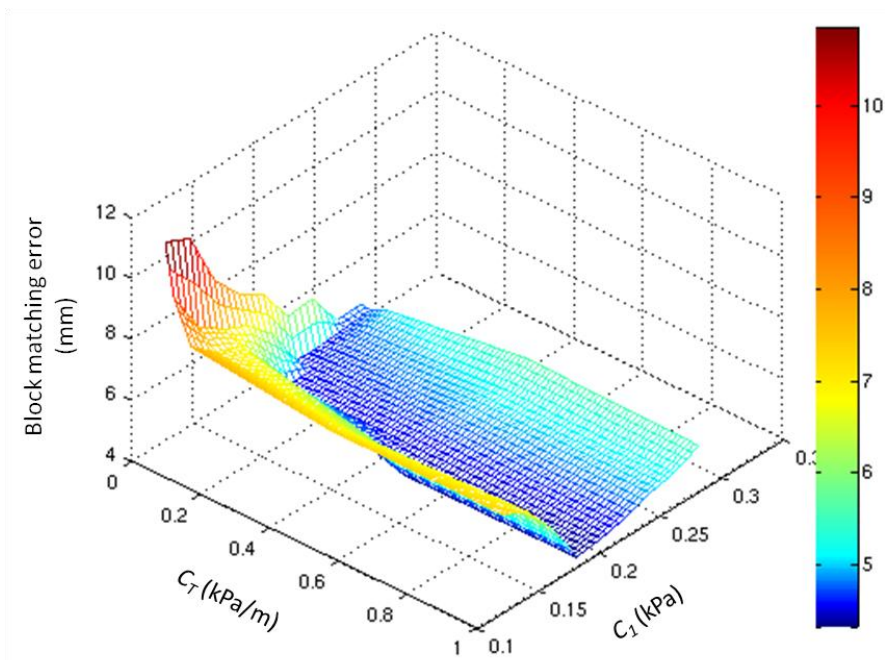
Figure 4.7: The parameter space, using the block matching comparison measure over the whole model as the metric, was investigated. The minimum lies along a flat valley, indicating the trade-off behaviour between the C_1 and C_T parameters.

(a)   (b)
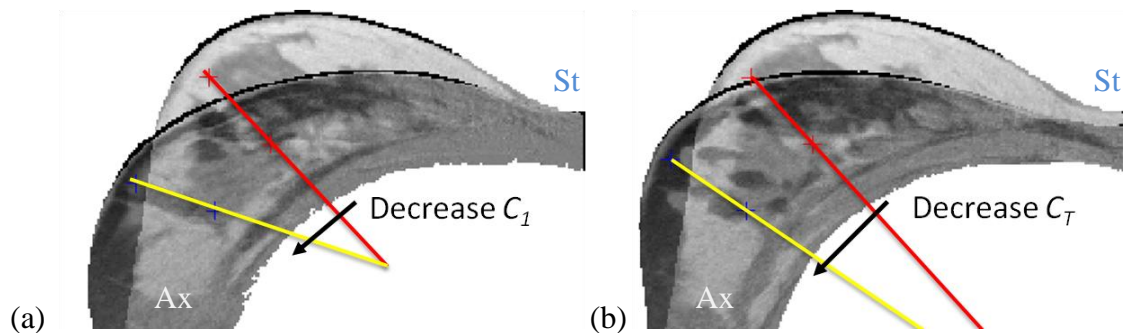
Figure 4.8: Difference images between models, with sternal (St) and axillary (Ax) regions identified, where (a) the material stiffness parameter, C_1, was reduced from 260 Pa to 120 Pa with a high tied contact value (10 MPa/m) and (b) where the contact stiffness parameter, C_T, was reduced from 10,000 kPa/m to 11 kPa/m, with C_1 set as 260 Pa. Two landmark points were identified in each model warped image and used to illustrate the difference in the model deformations.

The contact stiffness parameter, C_T, determines the level of sliding of the breast tissues on the rib surface, so the parts of the model most influenced by the C_T value would be the ones that lie closest to the rib surface. The rib surfaces of the prone and supine MR images were masked with a layer of voxels above the rib face of the model for Volunteers 1 and 2,

respectively. The thickness of the mask from the rib face of the model was determined by the thickness of the torso at the cranial and caudal edges of the prone and supine images, which corresponds to 8 mm and 14 mm, respectively, for Volunteers 1 and 2. The rib region masked prone image was warped using the FE model deformations. This FE-warped image was compared with the rib region masked supine image using the block matching method to assess the accuracy of the model deformations on the rib surface. The optimal C_T values were found to be 10 kPa/m and 15 kPa/m for Volunteers 1 and 2, respectively. In this two parameter optimisation, the C_1 parameters were only optimal for the deformations of the tissues around the ribs regions, thus these values were disregarded. The tied parameter was then fixed and block matching over the entire model was used as the metric in order to estimate the homogeneous C_1 parameter.

Using the above approach, the optimal parameters for the combination of a homogeneous material stiffness (C_1) model with tied contact constraints (C_T) on the rib surface were:

- C_T=10 kPa/m and C_1=125 Pa for Volunteer 1
- C_T=15 kPa/m and C_1=300 Pa for Volunteer 2.

4.6   Heterogeneous biophysical breast models

In the breast models described above, the tissues were modelled as isotropic, homogeneous and incompressible materials. However, it is known that normal breast tissue is primarily made up of two distinct tissues types: adipose and fibroglandular tissues. The skin and rib surfaces of the breast tissues were segmented to create the FE models. The FE models were used to mask the MR images to identify the regions that were included within the biomechanical model. Within this mask the adipose, fibroglandular, and muscle structures were identified using an intensity threshold, followed by manual editing with Medical Image Display and Analysis Software (MIDAS) (Freeborough et al., 1997). This process was used to identify three binary masks for adipose, fibroglandular and muscle tissues [Figure 4.9].
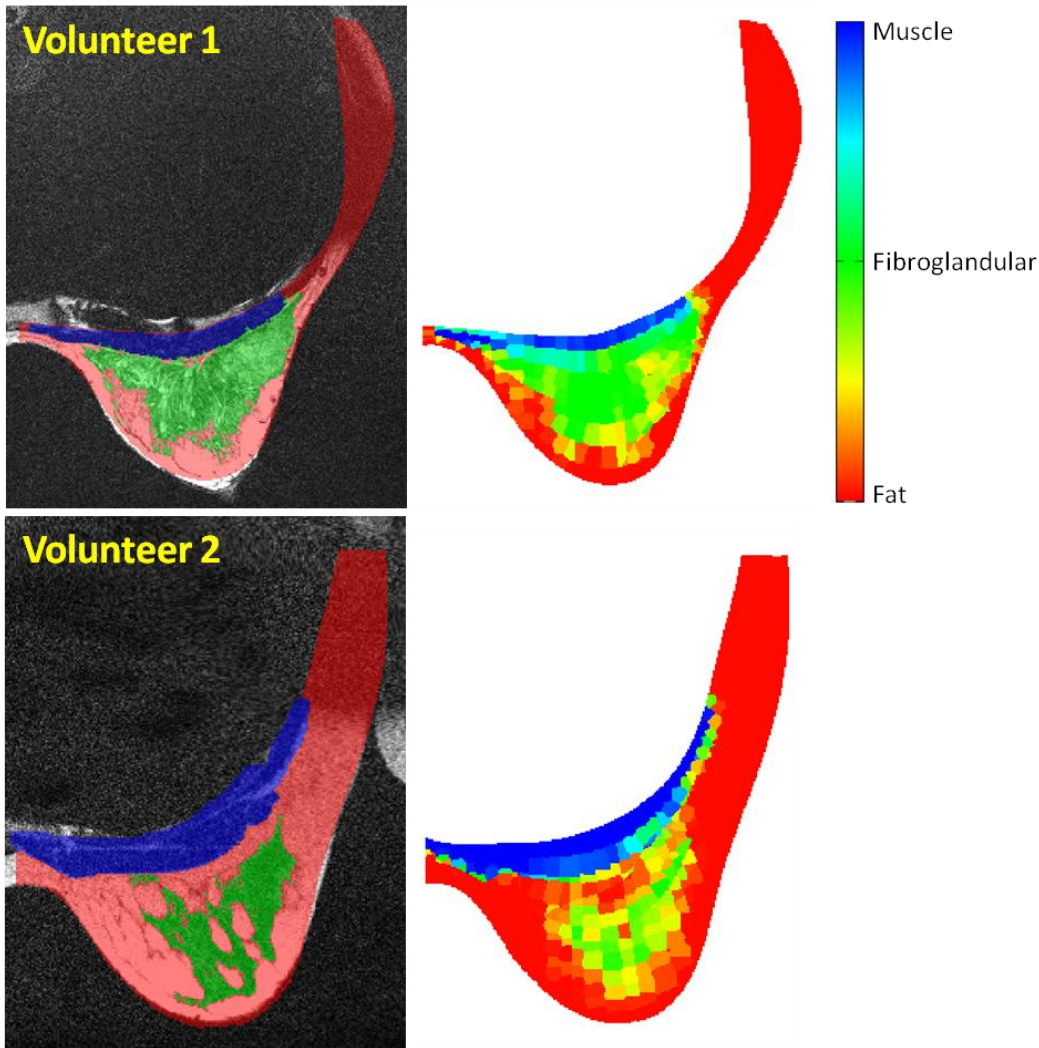
Figure 4.9: The breast and muscle tissues for the two volunteers were isolated in the MR prone image using a mask generated from the FE model. The adipose (red), fibroglandular (green) and muscular (blue) tissues were segmented using an intensity threshold followed by manual editing using the MIDAS three dimensional image analysis software. The heterogeneous stiffness field was then described using the distribution of Gauss points over the three dimensional FE breast mesh, as shown on the right.

In published models that take into account the heterogeneity of the breast tissues, elements were classed as a particular tissue type based on the majority tissue type in the particular element (Azar et al., 2001) or the tissue type associated with the centroid of the element (Tanner et al., 2009). This down-sampling interpolates the segmentations of the breast tissues to be at the level of the element sizes. Whether or not this is an acceptable resolution depends on the size of the elements. In the Tanner studies, for example, the average size of the elements was 15.2 mm^3.

The breast FE models that were developed in this thesis used hexahedral elements with tri-cubic Hermite basis functions, which enforce C^1 continuity across element boundaries. This meant that a relatively small number of elements (120) were required to accurately describe the shape of the breast tissues, whilst the total number of geometric solution degrees of freedom was 4606 (see Appendix A for details regarding the convergence analysis of the models). The average size of the elements was 6923 mm^3 and 9727 mm^3 for Volunteers 1 and 2, respectively [Figure 4.6]. To adequately represent the smaller tissue features, a different interpolation scheme was required to model the heterogeneity in the breast tissues (Section 3.4.2: Voronoi method). The segmentations were divided up into elements and each voxel in the element segmentation was assigned to the closest Gauss point in that element. In the current implementation, there were 64 Gauss points (4 x 4 x 4) in each element. The material stiffness, C_1, at each Gauss point was then calculated by linearly combining the weighted stiffnesses of each tissue type [Figure 4.9]:

$$C_1^{GP} = w_{ad}C_1^{ad} + w_{fg}C_1^{fg} + w_{mu}C_1^{mu} \tag{4.1}$$

where w_{ad}, w_{fg} and w_{mu} are the proportions of voxels associated with each Gauss point for the adipose, fibroglandular and muscle segmentations, respectively.

The difference in the densities of the breast tissues was accounted for at each Gauss point using the weighting scheme described above, with the density values for adipose, muscle and fibroglandular set to be 950 kg/m^3, 1,050 kg/m^3 (Hubbell and Seltzer, 2004) and 1,040 kg/m^3 (Bushberg et al., 2002), respectively.

In the heterogeneous model of the breasts, the material stiffnesses of the various tissues (C_1^{ad}, C_1^{fg} and C_1^{mu}) and the tied contact stiffness were taken into consideration in a two stage process. Firstly, the material stiffness of the muscle and the tied contact stiffness were estimated. The segmentation of the prone breast images was split up into two compartments: breast tissues (adipose and fibroglandular); and muscle. Since the bulk of the model was composed of adipose and fibroglandular tissues, the stiffnesses of both these tissue groups were initially set as the previous estimate of the homogeneous C_1 values: 75 Pa and 122 Pa for Volunteers 1 and 2, respectively.

As in the previous section, the block matching metric was calculated only over the region of interest (muscle and rib), by using the segmentation of the muscle region with the previously defined rib mask (Section 4.5.1) to mask the prone image prior to FE warping. The masked

FE-warped images were compared to the clinical supine MR images using the block matching metric. It was found that the optimal C_1 parameters for the muscle tissue stiffnesses for Volunteers 1 and 2 were 1.0 kPa and 0.5 kPa, respectively, whereas the estimated value of the tied contact stiffness parameters was 25 kPa/m for both volunteers. Once the muscle material stiffness and the tied contact parameter were estimated, they were fixed and the fat and fibroglandular were optimised simultaneously using the block matching comparison measure over the whole breast model.

Using the optimisation framework described above with the heterogeneous FE models, the tied contact penalty stiffness (C_T) and the material stiffnesses for the adipose (C_1^{ad}), fibroglandular (C_1^{fg}) and muscle tissues (C_1^{mu}) were estimated to be:

- C_T=25 kPa/m, C_1^{ad}=50 Pa, C_1^{fg}=60 Pa and C_1^{mu}=1.0 kPa for Volunteer 1
- C_T=25 kPa/m, C_1^{ad}=150 Pa, C_1^{fg}=300 Pa and C_1^{mu}=500 Pa for Volunteer 2.

4.7 Comparison of different breast biomechanical models

Biomechanical models of the breasts were used to simulate prone to supine reorientation of the breasts for two volunteers. The effects of modifying constraints on the rib surface and the stiffness fields in the biomechanical models were investigated. The block matching method was used to assess the accuracies of the different breast biomechanical model predictions.

4.7.1. Statistical analysis

The means and standard errors for the block matching measures of accuracies were calculated for the different biomechanical models of the breast. After confirming normality (Shapiro-Wilk test) and equal variance (Levene's test), the differences between the three models were assessed using a one way ANOVA design. The p value to reject normality and/or equal variance was set at $p \leq 0.05$. Where a significant difference (p$\leq$0.05) between the models was detected, *post-hoc* comparisons were conducted using a Tukey's test.

4.7.2. Results

The accuracy of the predictions from each type of model described in the previous sections were tested by comparing the model-warped images with clinical images of the breasts under supine gravity loading using the block matching method [Table 2]. One way ANOVA test

among the three models used to simulate the prone to supine reorientation for Volunteer 2 indicated that there were significant differences between the models (p<0.001). *Post-hoc* comparisons revealed that, in comparison to using zero-displacement boundary conditions on the rib surface of the breast model, incorporating contact mechanics to allow for breast tissue sliding on the rib surface significantly improved the model predictions for Volunteer 2 (p<0.001). The tied stiffness constraint on the rib surface of the model, was estimated to be 15 kPa/m for Volunteer 2, which corresponds to sliding of the breast model on the rib surface of up to 23 mm. The additional relaxation of the model constraints by allowing the material stiffness to vary across the breast further improved the model predictions for Volunteer 2 significantly (p<0.001).

Table 2: The accuracy of the biomechanical model predictions were tested by calculating the mean (±SE) of the overall block matching measure for FE models with different assumptions: homogeneous mechanical properties with fixed boundary conditions (Homogeneous); homogeneous mechanical properties with tied contact constraints (Homogeneous + contact); heterogeneous mechanical properties with tied contact constraints (Heterogeneous + contact).

	Volunteer 1 error (mm)	Volunteer 2 error (mm)
Homogeneous	5.74 ± 0.02 (n=44214)	5.03 ± 0.01 (n=45368)
Homogeneous + contact	5.71 ± 0.02 (n=43241)	4.63 ± 0.01 (n=44981)
Heterogeneous + contact	5.47 ± 0.02 (n=43591)	4.14 ± 0.01 (n=45966)
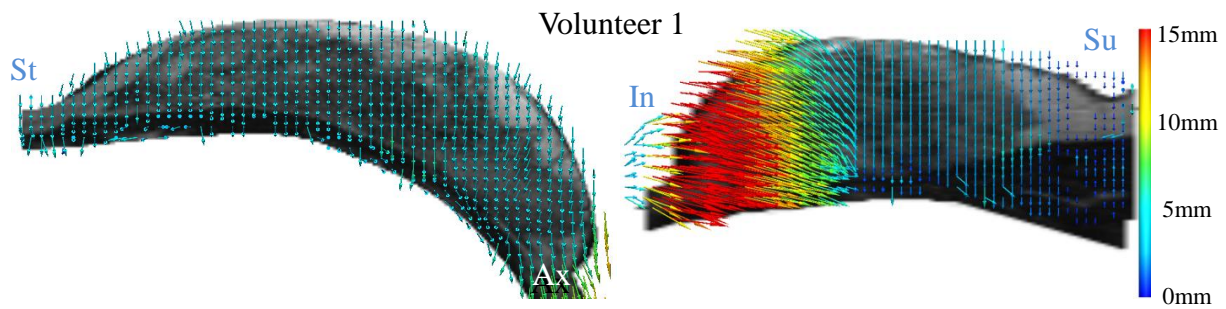
(a) Prone MR image warped using fixed rib constraints on a homogeneous FE model.
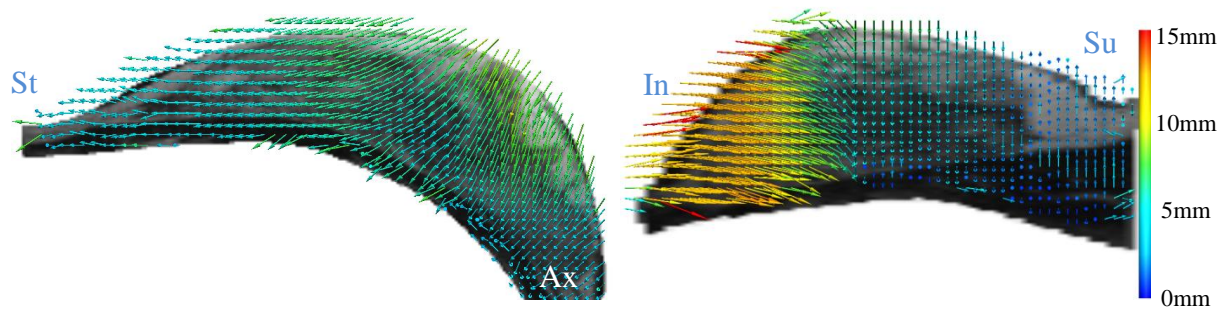
(b) Prone MR image warped using tied rib constraints on a homogeneous FE model.
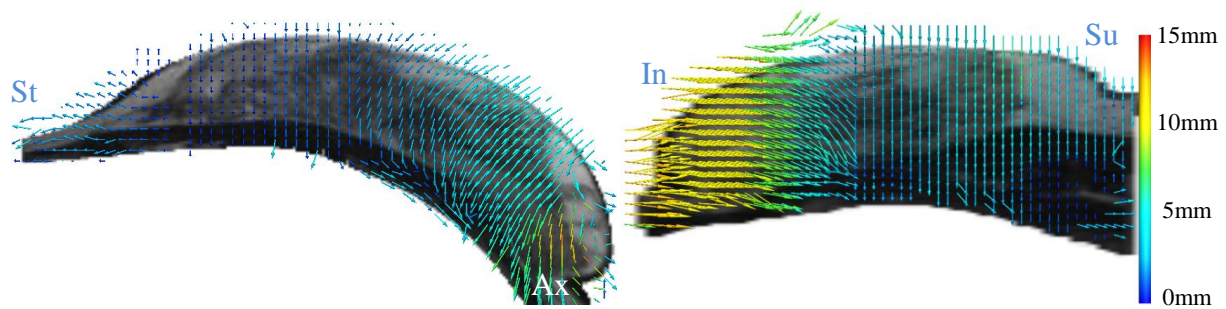
(c) Prone MR image warped using tied rib constraints on a heterogeneous FE model.

Figure 4.10: Registration error vectors using FE breast models to predict prone to supine reorientation overlaid on an axial slice with sternal (St) and axillary (Ax) regions identified (left column) and a sagittal slice with superior (Su) and inferior (In) regions identified (right column) of the FE-warped image for Volunteer 1. The magnitudes of the error vectors are colour coded.
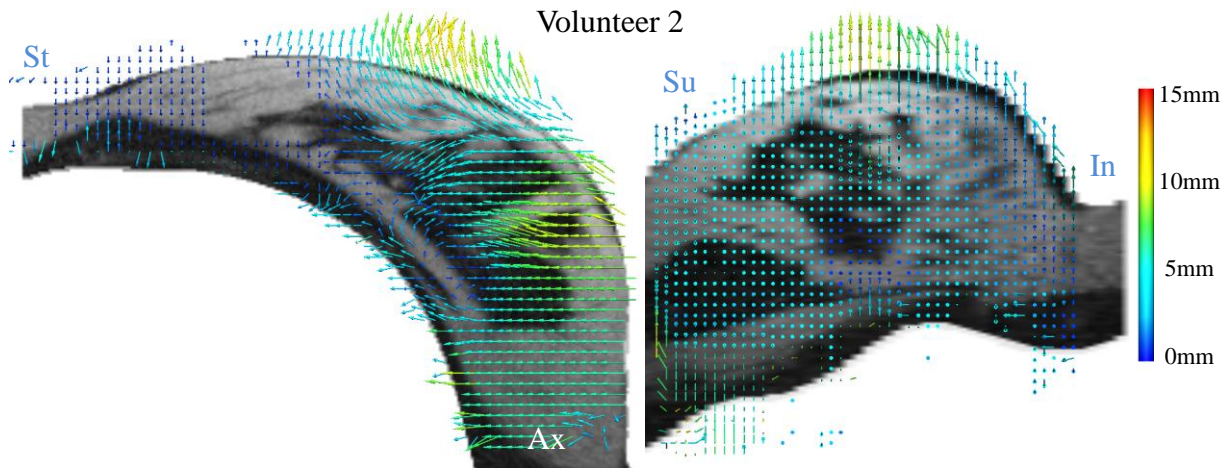
(a) Prone MR image warped using fixed rib constraints on a homogeneous FE model.
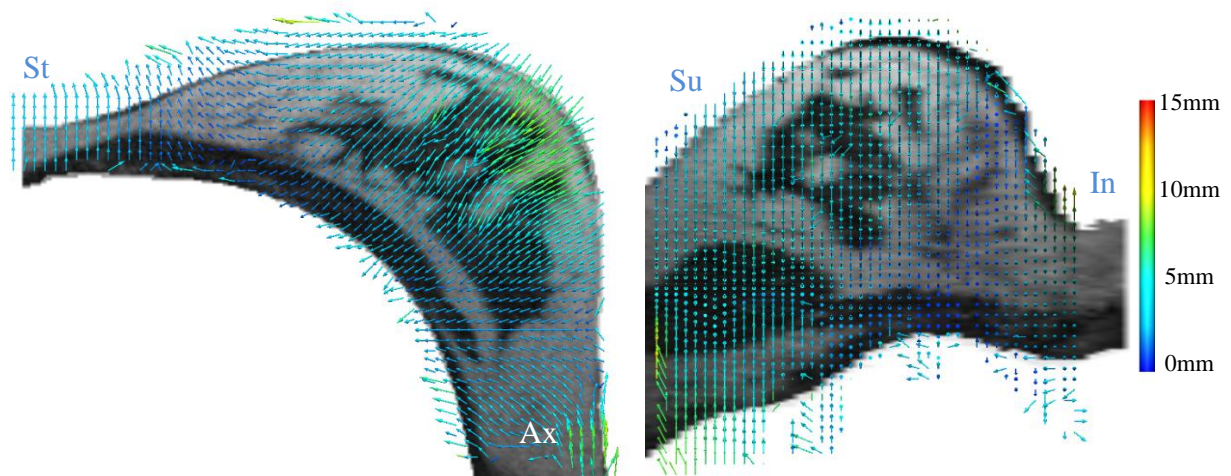
(b) Prone MR image warped using tied rib constraints on a homogeneous FE model.
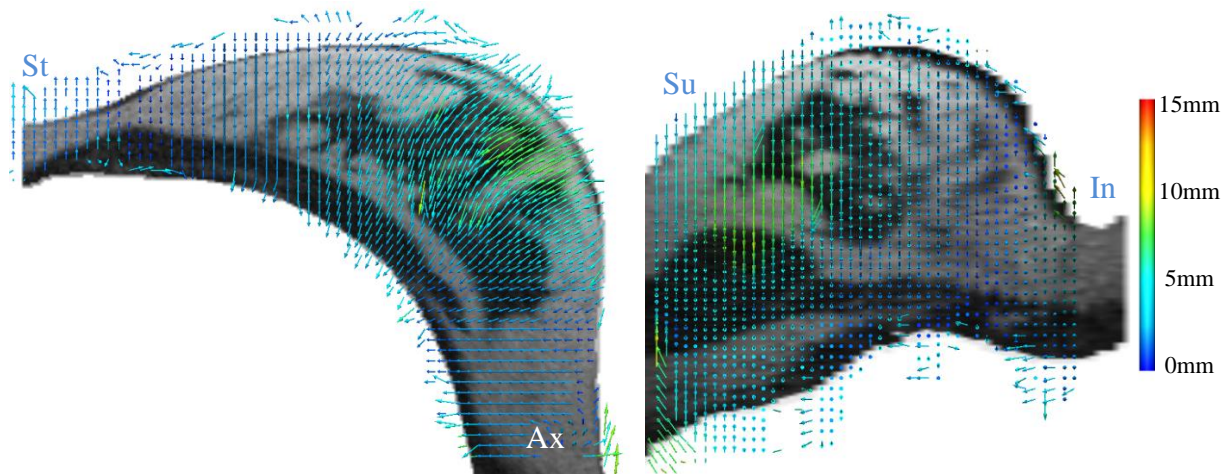
(c) Prone MR image warped using tied rib constraints on a heterogeneous FE model.

Figure 4.11: Registration error vectors using FE breast models to predict prone to supine reorientation overlaid on an axial slice with sternal (St) and axillary (Ax) regions identified (left column) and a sagittal slice with superior (Su) and inferior (In) regions identified (right column) of the FE-warped image for Volunteer 2. The magnitude of the error vectors are colour coded.

For Volunteer 1, one way ANOVA revealed that there were significant differences between the models used to simulate prone to supine reorientation (p<0.001). *Post-hoc* comparisons revealed that the heterogeneous model with contact constraints on the rib surface was significantly (p<0.001) more accurate than the homogeneous models [Table 2]. The addition of contact constraints on the rib surface was considered independently by comparing two homogeneous models, one with zero-displacement boundary constraints on the rib surface and the other with sliding contact constraints. *Post-hoc* comparisons, using the block matching over the whole breast model as the error measure, indicated that there was no significant difference (p=0.60) between the models with zero-displacement and sliding boundary constraints [Table 2: Homogeneous vs. Homogeneous + contact].

The error vectors from the block matching comparison method contain information about the regional nature of the errors in the models; however this information was not taken into account in the statistical analysis. Altering the constraints on the rib surface of the breast model would have the greatest effect in the regions that lie near to this boundary. Further investigation, using an independent t-test to analyse the block matching error vectors which were closer than 8 mm from the rib surface (approximate thickness of the torso at the cranial and caudal edges of the prone and supine images), revealed that incorporating contact constraints significantly improved the model predictions around the rib surface (mean ± SE:: 6.90 mm ± 0.04 mm with fixed constraints and 5.96 mm ± 0.03 mm with sliding constraints, p<0.001). The sliding constraint, C_T on the rib surface of the model for Volunteer 1, was estimated to be 10 kPa/m, which corresponds to up to 22 mm sliding of the breast model on the rib surface.

As shown in Figure 4.10 and Figure 4.11, in addition to an overall quantitative measure of accuracy of using the FE models to predict the deformations of the breast tissues, the block matching approach gives regional error estimates. For Volunteer 1, the lower half of the FE model needs to move primarily along the CC direction (towards the head) to match the clinical supine data, as shown in the sagittal images in Figure 4.10. This error was reduced as tied constraints were used for the rib surface and further improvements were achieved when heterogeneous material properties were incorporated into the model.

For Volunteer 2, it can be seen that the errors in the sagittal plane were similarly reduced as the rib constraints were changed from zero-displacement boundary conditions to using

contact constraints. Using fixed boundary constraints on the rib surface resulted in an underestimation of the material stiffness parameter, as shown in Figure 4.11a, where the error vectors indicate that the model needs to move in the anterior and medial directions to match the clinical supine data. Block matching analysis of the homogeneous and heterogeneous models with tied constraints on the rib surface revealed that the largest error vectors occurred in the interior of the breast models.

4.8 Discussion

In this chapter, the effects of constraints on FE breast models with respect to boundary conditions on the rib surface and homogeneous and heterogeneous material properties were investigated. The purpose of this chapter was to probe the importance of these modelling assumptions in predicting the three dimensional deformations of the breast from prone to supine gravity loading states using the block matching error measure described in Chapter 3.

It was found that for these two volunteers, the addition of contact constraints on the rib surface and heterogeneous material properties, significantly improved the accuracy of predicting the deformations of the breast tissues from prone to supine gravity loading orientations. A limitation of this work was that only two volunteers were considered. Further studies would need to be investigated to validate the techniques used and conclusions drawn.

The use of contact constraints on the rib surface of the homogeneous breast model, in contrast to having zero-displacement boundary conditions, significantly improved the accuracy of the model predictions for Volunteer 2. However, for Volunteer 1, it was found that there were insignificant differences when considering the block matching over the whole breast model. In analysing the overall accuracy of the model, only the magnitudes of the error vectors were considered, while the regional effects were ignored. As discussed previously, the tied contact constraint has the greatest effect on the model near the ribs region. Thus, only the block matching error vectors which were within 8 mm from the rib surface were investigated for Volunteer 1 (approximate thickness of torso at cranial and caudal edges of the breast images). It was found that using contact constraints, in contrast to using zero-displacement boundary conditions, on the rib surface significantly improved the accuracy of the model simulations. This is to be expected because the retromammary bursa sits between the breast tissues and the muscle tissue (as explained in Chapter 2), which allows for sliding between these two tissue groups. However, the breast model contains muscle tissue, in addition to the adipose and

fibroglandular tissues, which meant that the sliding constraint was not positioned at the breast-muscle interface, but closer to the muscle-rib or muscle-muscle interface. There are several muscle groups that lie under the breast tissues, which attach to the bones in the pectoral region as shown in Figure 2.4. Aside from those attachment points, these muscles can slide with respect to each other and over the rib surface due to the surrounding fascia.

A limitation of the current models is that this combined sliding behaviour (breast-muscle, muscle-muscle, muscle-ribs) is modelled using a single tied contact parameter, with only the muscle attachments at the sternum modelled using zero-displacement boundary conditions, and the other points of the muscle attachments ignored. The MRI data that were used to develop the models did not have a high enough resolution to be able to distinguish between the muscle groups, let alone their respective attachment points on the ribs. In addition, separating the breast and muscle tissues into independent meshes would result in thin elements, which can cause numerical issues when solving the mechanics.

In addition to allowing for sliding between the breast and the ribs, the model was further significantly improved by accounting for the material stiffnesses and densities of the adipose, fibroglandular, and muscular tissues in the model. A staged approach was used where the tied contact and muscle material stiffnesses were first identified by only considering the block matching error measures around the rib and muscle regions, while having the fat and fibroglandular stiffness values fixed. Secondly, the adipose and fibroglandular tissue stiffnesses were investigated simultaneously, with the muscle stiffness and tied contact stiffness parameters fixed.

For Volunteer 1, the estimated adipose, fibroglandular, and muscle material stiffness were 50 Pa, 60 Pa and 1.0 kPa, respectively. The fibroglandular material stiffness was at the lower bound of the permissible values for the fibroglandular tissues of the model, where decreasing the value of the C_1^{fg} parameter leads to numerical errors in the simulation. These values are lower than the homogeneous estimations of the breast model stiffness (C_1=75 Pa with zero-displacement boundary conditions and C_1=100 Pa with contact constraints on the rib surface), which highlights the importance of the choice of boundary constraints in estimating mechanical properties. This was due to the estimation of the stiffness of the muscle region of the breast model being much larger (C_1^{mu}=1.0 kPa) than the homogeneous estimations of the breast model stiffness. This increased stiffness in the muscle region resulted in a much lower estimate of the C_1 stiffness parameters for the rest of the breast model (C_1^{ad}, C_1^{fg}) to match

the global deformation of the breast during reorientation from prone to supine for Volunteer 1. However, as can be seen in Figure 4.12, this results in the breast model being too soft, as illustrated by the difference in the respective location of the nipple (red circle) between the clinical MR supine image and the FE model warped image. For Volunteer 2, the estimated stiffness parameters for the adipose and fibroglandular tissues were similarly too soft, causing over-rotation of the internal structures about the cranial-caudal axis in the model as highlighted (yellow circles) in Figure 4.13.
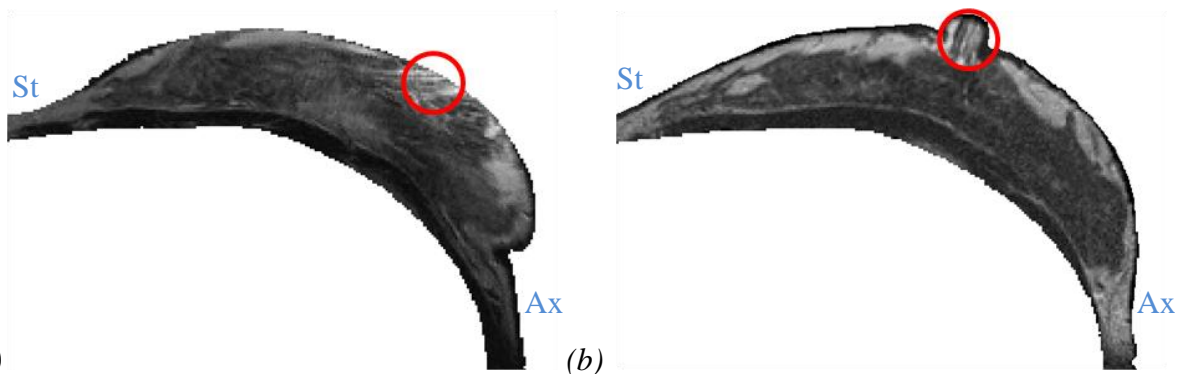
(a)   *(b)*

Figure 4.12: (a) FE model with heterogeneous material stiffness and tied contact constraints on the ribs and (b) the clinical supine MR data for Volunteer 1. The nipple location is highlighted (red) in both images, with the sternal (St) and axillary (Ax) regions identified.
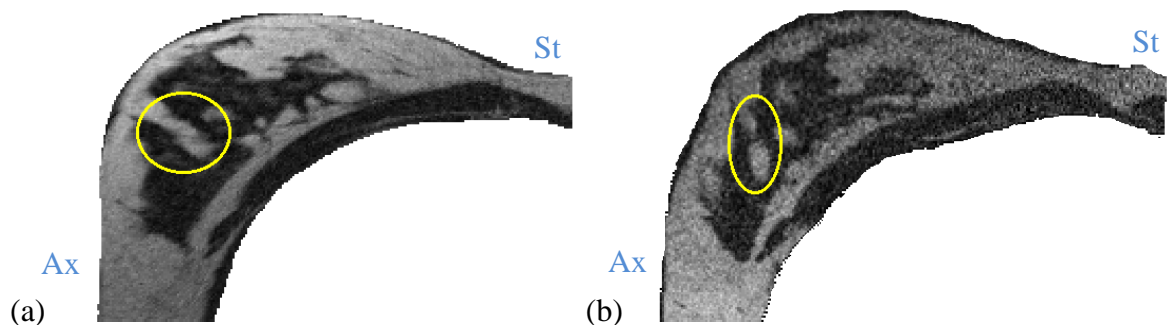
(a)   (b)

Figure 4.13: (a) FE model with heterogeneous material stiffness and tied contact constraints on the ribs and (b) the clinical supine MR data for Volunteer 2. A landmark highlighting the over-rotation of the internal structures in the FE model is indicated (yellow), with the sternal (St) and axillary (Ax) regions identified.

There are several factors that may contribute to this rotation and underestimation of the material stiffness values in the two volunteers. In Figure 4.8, it can be seen that this rotation of the internal tissues was more sensitive to lowering the material stiffness value than lowering the tied stiffness value. In the current implementation of the FEM software

(CMISS), contact mechanics cannot be employed in the 'reverse' method, where the biomechanical unloaded reference state is determined from a known loaded configuration. Therefore, zero-displacement boundary constraints were instead applied on the nodes on the posterior surface of the breast model. As noted earlier, there is a trade-off between the tied contact stiffness parameter and the material stiffness parameter, where an increase in the contact stiffness would require a reduction in the material stiffness parameter to achieve a similar deformation. Fixing the posterior surface of the breast in the 'reverse' step (equivalent to a 'high' contact stiffness value), could thus contribute to the underestimation of the material stiffness value, resulting in an increase in the rotation of the highlighted region in Figure 4.13. In addition, only the sliding contact between the rib surface and muscles was accounted for, whereas the sliding contact between the muscle and the breast tissues was not considered, as the muscles and breast tissues were incorporated into the same mesh. This has the effect of fixing the posterior surface of the breast with the anterior surface of the muscles (equivalent to a 'high' contact stiffness value), which could similarly result in an underestimation of the material stiffness values for the adipose and fibroglandular tissues.

Another possible cause of this rotation in the FE models was that the mechanical effects of the skin were not included in the model. Skin has been found to be highly nonlinear with a higher material stiffness than adipose or fibroglandular tissues (Gefen and Dilmoney, 2007). Accounting for these effects of skin in the biomechanical model would have a stiffening effect near the anterior surface of the breast model. Given sliding contact constraints on the rib surface, the addition of skin for prone to supine deformations could result in a shearing action, which would reduce the rotation observed in the current model. However, to model skin, aspects such as the attachment of the skin to the underlying tissue, the mechanical properties of the skin (Gefen and Dilmoney, 2007), the effect of the pre-tension (Langer, 1978) of the skin in the prone and supine gravity loaded states would all need to be investigated.

Another potential cause of this inaccuracy in the internal breast deformation could be due to the mechanical properties of the breast model. The constitutive behaviour for both the homogeneous and heterogeneous cases were modelled using the neo-Hookean material relation, which assumes that the tissue is isotropic and relatively linear. The effect of this assumption will need to be tested by the application of other material relations. In Tanner et al. (2011), FE models of the breast were used to simulate compression in the prone position,

and it was found that transversely isotropic material properties with an increased stiffness in the anterior-posterior (AP) direction were significantly more accurate than isotropic material properties, when considering the accuracy of the predicted locations of twelve manually selected landmarks. However, these models were based on a biomechanical reference model generated from prone MRI data, which due to the gravity loading, is pre-stretched in the AP direction. The application of transversely isotropic material properties will need to be investigated for the breast models described in this thesis to test whether the same improvements can be achieved.

In the current model, the ribs and the shoulders were used to constrain the breast model during the prone to supine simulations. However, it was observed that the location of the shoulder changed between the prone and supine clinical image acquisition. When an individual is lying in a prone position, the shoulders naturally drop forward, while in the supine position they move in the posterior direction. When the shoulder changes position, the pectoral muscle also deforms, and this effect is currently not accounted for in the prone to supine simulations, giving rise to larger modelling errors in this region. In future studies, the effect of the motion of the shoulder on the deformation of the tissues in the breast model will need to be studied.

The block matching results showed that the rib boundary conditions and the mechanical properties of the tissues in the breast model play an important role in the accuracy of the prone to supine deformation predictions. Further improvements can be made to the FE model and quantified using the block matching technique. In Chapter 5, these FE models were used as priors to an image-based non-rigid registration method. It was demonstrated that the image-based method can help to: (i) recover the local deformations; and (ii) identify the regions where the deformation predictions require improvement.

Chapter 5: Combining biomechanical models with free-form deformations

In this chapter the registration accuracy of large deformation FE-based approaches was compared with a conventional intensity-based non-rigid technique. In addition, the combination of the two methods, whereby the FE models are used as priors to the non-rigid registration, is investigated. The block matching algorithm (see Chapter 3) was used to quantify the regional errors of the different modelling methods.

5.1 Introduction

There has been considerable interest in applying image registration techniques to warp one medical image of the breast to match another. Image registration techniques can be classed into two broad categories: feature-based, where the alignment is between features such as points, contours, surfaces or volumes; and intensity-based, where the objective function is calculated directly from the voxel intensities.

The majority of work in three dimensional breast image registration has focused on intensity-based measures (Guo et al., 2006, Sivaramakrishna, 2005). This is because the breasts are soft tissues with no rigid structures, which means that only a few features such as the skin and rib boundaries and the nipple can be consistently identified for feature-based registration techniques. Different transformations have been applied to breast images with early work using affine or rigid transformations to warp the images (Zuo et al., 1996). However, breast

tissues undergo non-rigid deformations that can be poorly represented with rigid or affine transformations. Previous work has acknowledged this limitation and used non-rigid registration techniques such as thin-plate splines (Bookstein, 1989, Wirth et al., 2002), fluid registration (Crum et al., 2005), and free-form deformations (FFD) based on B-spline warping (Rohlfing et al., 2003, Rueckert et al., 1999) to capture the local deformations of the soft breast tissues.

The FFD based on B-splines algorithm as defined by Rueckert et al. (1999), is an inherently multi-scale technique. For non-linear breast deformations between sequential prone MR imaging, it was found that multi-level FFD registration was less sensitive to large localised deformations than to single-level FFD registration for sequential breast MR imaging (Schnabel et al., 2003). In this thesis, the large deformations of the breast phantom under compression, and breast tissues under different gravity loading conditions should similarly be better represented with multi-scale registration techniques, such as fluid registration and FFD based on B-splines, compared to single-level techniques. In this chapter, the freely available FFD software Image Registration Toolkit (IRTK[4]) was used in combination with the FE models developed previously in Chapter 3 and Chapter 4.

In previous studies, FE models have been used to simulate physically plausible deformations of the breast tissues for statistical deformation models (Tanner et al., 2008) or for the validation of other non-rigid registration algorithms such as fluid registration (Carter et al., 2006, Hipwell et al., 2007) or FFD based on B-splines techniques (Schnabel et al., 2003). Alternatively some authors have suggested using the information from fluid or FFD registration to determine kinematic boundary conditions to apply to FE models (Carter et al., 2009, Tanner et al., 2009). However, prescribing such displacement boundary conditions (for example, to match displacements at the skin surface) can introduce unrealistic reaction forces at the free surfaces of biomechanical models. In these studies, either the intensity-based non-rigid registration framework or the biomechanical model deformations were regarded as the 'gold standard'. However, a fundamental flaw with empirical methods that align images based on voxel intensities is that the deformations may be physically implausible. On the other hand, while biomechanical models may constrain the deformations to be within physically plausible ranges, the accuracy of such deformations depends upon the assumptions

---

[4] http://www.doc.ic.ac.uk/~dr/software/

of the FE models.

Carter et al. (2006, 2008) investigated the combination of fluid registration with a biomechanical model for supine and prone three dimensional MR image registration. Heterogeneity of the breast tissues was accounted for by assigning different densities to the adipose and fibroglandular tissues, while maintaining the same material stiffness. An estimation of the reference state was determined by applying gravity in the anterior direction to supine models of the breast and then re-setting the stresses to be zero. The prone orientation was then simulated by applying gravity again in the anterior direction. The problem with this method is that, in the initial case, the supine orientation is treated as a zero-stress zero-strain unloaded state. Deforming the supine mesh by applying gravity in the anterior direction does *not* negate the effect of gravity in the supine orientation. In contrast, in this thesis, the effect of gravity is accounted for by a reformulation of the governing equations for finite elasticity to correctly account for its effect (Rajagopal et al., 2007).

In Carter et al. (2009), displacement boundary conditions were applied to the rib and skin surfaces of the prone-deformed mesh to allow for better alignment with the MR prone image. The model deformations were then used to warp the prone image to the supine configuration. Further alignment was then done by using a fluid registration algorithm as described by Crum et al. (2005). The accuracies of the fluid registration, FE-based registration, and the hybrid method were then assessed by calculating the target registration error of eight manually defined landmarks.

The major differences between the published study by Carter et al. (2008) and the research in this chapter are in the model framework and the analysis of the error:

a) The biomechanical models described in this thesis used an estimation of the unloaded reference state of the breast tissues based on a reformulation of the finite deformation equations to correctly account for the physics in the estimation of the unknown unloaded state from the known loaded configuration. This technique for calculating the unloaded reference state was validated in Rajagopal et al. (2007).

b) The validation in Carter et al. (2008) was based on the target registration error of eight manually defined landmarks. In contrast the following analysis was based on the block matching approach as described in Chapter 3. This gives the regional error distribution over the entire breast, and thus a better understanding of the accuracy of

the biomechanical models.

c) The boundary conditions were based on physical boundary constraints of the breast tissues (for particulars please refer to Chapter 4), in contrast to defining nodal displacements on the skin surface of the breast mesh, which give rise to non-physical reaction forces on the skin surface.

d) The heterogeneity of the breast tissues were accounted for by setting material stiffnesses and density values for the adipose, fibroglandular, and muscular tissues (previously optimised in Chapter 4). In Carter et al. (2008), adipose and fibroglandular tissues were assumed to be of equal stiffness, while the densities were varied according to tissue type.

e) FFD based on B-splines was used as the empirical non-rigid registration technique to recover the local deformations instead of the fluid registration algorithm used in Carter et al. (2008). These techniques were found to be comparable for the non-rigid registration of MR derived FE simulation of X-ray images (Hipwell et al., 2007).

5.2 Methods

5.2.1 Free form deformations

In this chapter, the ability of the biomechanical models, developed in Chapter 3 and Chapter 4 to predict the large deformations of the breast, were compared with a conventional technique used for three dimensional breast image registration. The IRTK framework (Rueckert et al., 1999) was used to align the uncompressed and compressed breast phantom images in addition to warping the prone breast images to match to the supine data for two volunteers (Section 4.3).

The global motion between the images was modelled using rigid registration to align the global location of the images, followed by an affine transformation allowing for shearing and scaling of the images:

$$\boldsymbol{T}_{global}(x, y, z) = \begin{pmatrix} \theta_{11} & \theta_{12} & \theta_{13} \\ \theta_{21} & \theta_{22} & \theta_{23} \\ \theta_{31} & \theta_{32} & \theta_{33} \end{pmatrix} \begin{pmatrix} x \\ y \\ z \end{pmatrix} + \begin{pmatrix} \theta_{14} \\ \theta_{24} \\ \theta_{34} \end{pmatrix} \tag{5.1}$$

The local motions in the images were modelled by altering the parameters of a FFD mesh, Φ

with $n_x \times n_y \times n_z$ control points, $\emptyset_{i,j,k}$ distributed uniformly (δ spacing) over the image domain, $\Omega = \{(x, y, z)|0 \leq x \leq X, 0 \leq y \leq Y, 0 \leq z \leq Z\}$. The local deformations were represented as a three dimensional tensor product of 1D cubic B-splines:

$$T_{local}(x, y, z) = \sum_{l=0}^{3} \sum_{m=0}^{3} \sum_{n=0}^{3} B_l(u) B_m(v) B_n(w) \emptyset_{i+l,j+m,k+n} \tag{5.2}$$

where $= \left\lfloor \frac{x}{n_x} \right\rfloor - 1$, $j = \left\lfloor \frac{y}{n_y} \right\rfloor - 1$, $k = \left\lfloor \frac{z}{n_z} \right\rfloor - 1$, $u = \frac{x}{\delta} - \left\lfloor \frac{x}{\delta} \right\rfloor$, $v = \frac{y}{\delta} - \left\lfloor \frac{y}{\delta} \right\rfloor$, $w = \frac{z}{\delta} - \left\lfloor \frac{z}{\delta} \right\rfloor$,

with $\lfloor \ \rfloor$ denoting the floor function and where B_l represents the lth B-spline basis function:

$$\begin{aligned} B_0(u) &= (1 - u)^3/6 \\ B_1(u) &= (3u^3 - 6u^2 + 4)/6 \\ B_2(u) &= (-3u^3 + 3u^2 + 3u + 1)/6 \\ B_4(u) &= u^3/6 \end{aligned} \tag{5.3}$$

The multi-scale capability of IRTK comes from being able to refine the control spacing of successive FFD meshes. Low resolution FFD meshes (larger control point spacing) allow for the modelling of large-scale non-rigid deformations, while finer resolution meshes (smaller control point spacing) allow for the alignment of the highly local deformations. The deformation of the images was calculated by combining the global transformation with the local deformations given at each FFD resolution level, l.

$$T(x, y, z) = T_{global}(x, y, z) + \sum_{l=1}^{L} T_{local}^l(x, y, z) \tag{5.4}$$

In the following analysis, rigid and affine transformations were used to align the global deformations in the images. The local motions between the source and target images were then modelled using an FFD mesh that was iteratively refined from 40 mm x 40 mm x 40 mm to a 10 mm isotropic mesh. The similarity measure was based on NCC, with linear interpolation of the warped images.

5.2.2 Finite element models

In Chapter 3, a heterogeneous FE model of a breast phantom was created and used to simulate the deformations of the breast phantom under AP and CC compressions with contact constraints. For validation purposes, three dimensional MR images were also obtained of the breast phantom under compression in the AP and CC directions. The ability of the FE model to simulate the compressed states was analysed using the block matching method (described

in Chapter 3), as well as feature-based methods.

The breast phantom contained twelve landmarks, of which six were cystic masses and six were solid inclusions. The deformations of these internal features were used to assess the accuracy of the FE simulations by comparing the centroid error (CENT), surface distance (Eq. 3.6: SMAD), and volume overlap (Eq. 3.5: DICE) for each of the masses in the FE-warped images with those from the experimental images. In addition, the block matching similarity measure was calculated across the whole image [Table 1].

In Chapter 4, biomechanical models of the breast were developed and used to model the deformations of the breast tissues, due to gravity, for prone to supine reorientation. Unlike previous models simulating gravity loading, contact mechanics were used to model the interactions of the breasts against the chest wall. The influence of heterogeneity in the breast was also investigated for adipose, fibroglandular, and muscular tissues in the model.

The errors of the FE model predictions were calculated using the block matching error measure as described in Chapter 3. It was found that accounting for both the sliding between the chest wall and the breast tissues, and the material heterogeneity in the breast, substantially improved the accuracy of the image alignment with 'gold standard' clinical images in comparison to a biomechanical model with zero-displacement boundary conditions on the rib surface [Table 2].

In this chapter, three non-rigid image registration methods were tested: (i) the conventional B-spline-based FFD registration (FFD); (ii) the biomechanical models as described in Chapter 3 and Chapter 4 (FEM); and (iii) a hybrid method, where the FE models are used as priors to FFD registration of the images (FEM+FFD). The nodes that define the cubic B-splines provide local support, where modifying the parameters of a node only affects the local neighbourhood of that node. This should help recover the local deformations that are not recovered by the FE models, due to the respective resolutions of the FFD and FEM meshes. As before, the error of the image alignment was assessed using the block matching method along with feature localisation measures for the breast phantom.

5.3 Comparison of different non-rigid image registration methods

Landmark-based error measures (CENT, SMAD, and DICE, as defined previously in Section 3.5.1) for each of the inclusions in the phantom were calculated for the three non-rigid registration methods. In addition, the block matching method was used to assess the accuracy of the alignment of the phantom and breast images by the methods.

5.3.1. Statistical analysis

The means and standard errors for the landmark-based and block matching error measures were calculated for the three registration methods. After confirming normality (Shapiro-Wilk test) and equal variance (Levene's test), the differences between the three methods were assessed using one way ANOVA tests for each of the error measures. The p value to reject normality and/or equal variance was set at $p \leq 0.05$. Where a significant difference ($p \leq 0.05$) between the methods for any of the error measures was detected, *post-hoc* comparisons were conducted using a Tukey's test

5.3.2. Results

One-way ANOVA tests on the target registration error of the inclusions in the breast phantom revealed that there were significant differences ($p < 0.001$) between the three methods for all accuracy measures (CENT, SMAD, DICE and block matching) [Table 3]. *Post-hoc* comparisons indicated that the hybrid method was significantly more accurate than either method independently, and that FEM substantially outperformed FFD ($p < 0.001$) for all measures of error [Table 3].

The three image registration methods were also tested on prone to supine reorientation of breast tissues for the two volunteers. One way ANOVA tests revealed that there were significant differences between the three non-rigid registration methods for aligning prone and supine breast images for both volunteers. *Post-hoc* comparisons revealed that, the hybrid method was significantly more accurate ($p < 0.001$) than either method independently, and that FEM substantially outperformed FFD [Table 4]. Furthermore, the hybrid FEM+FFD method substantially outperformed both individual methods.

Table 3: The highest compression experiments in the AP and CC directions were used to test the different image registration methods. The mean (±SE) of the centroid distances (CENT), surface distances (SMAD) and volume overlaps (DICE) of the 12 inclusions in the phantom for the two models (n=24) and the block matching method were used to assess the accuracy.

	CENT (mm)	SMAD (mm)	DICE (%)	Block Matching (mm)
FFD	4.53 ± 0.45	2.27 ± 0.28	30.3 ± 4.7	3.46 ± 0.01 (n=48289)
FEM	1.84 ± 0.14	0.97 ± 0.06	55.1 ± 3.5	2.75 ± 0.01 (n=45184)
FEM+FFD	1.38 ± 0.12	0.76 ± 0.04	63.9 ± 3.7	2.19 ± 0.01 (n=48316)

Table 4: The block matching error measure for prone to supine reorientation for three methods: free form deformation (FFD), biomechanical models (FEM) and a hybrid method, where FEM is used as a prior to FFD (FEM+FFD) as tested over two volunteers.

	Volunteer 1 error (mm)	Volunteer 2 error (mm)
FFD	11.5 ± 0.02 (n=42749)	6.05 ± 0.03 (n=46554)
FEM	5.47 ± 0.02 (n=45488)	4.14 ± 0.01 (n=45966)
FEM+FFD	0.95 ± 0.01 (n=50328)	3.74 ± 0.004 (n=48324)

(a) FFD   (b) FEM   (c) FEM + FFD

Figure 5.1: The compression of the breast phantom in the anterior-posterior (AP) and cranial-caudal (CC) directions were warped from the uncompressed images using a) the free-form deformation method (FFD), b) the biomechanical models (FEM) and c) a hybrid method where the FE-warped images were further warped using the FFD method (FEM+FFD). The experimental compressed images have been subtracted from the warped images to indicate the accuracy of the method. Brighter and darker regions highlight the where the images intensities differ.

Figure 5.2: The warped prone images were compared against the clinical supine images for the three methods for Volunteer 1 (left column) and Volunteer 2 (right column), with the sternal (St) and axillary (Ax) regions identified.

5.4 Discussion

The use of a biomechanical model as a prior to an intensity-based non-rigid registration algorithm was investigated in this chapter, in addition to the two methods being applied independently. Experimental MR images were used to assess the accuracies of the registration methods using the block matching method described in Chapter 3, in addition to

feature-based methods for the breast phantom. Non-rigid registration techniques can give rise to unrealistic deformations, such as implausible changes in the volume of the tissues, since they do not account for the physics of large deformations. The FE models can be used to apply physically realistic constraints on breast deformations. Though FE simulations may be physically plausible, reasonable assumptions regarding the tissue properties and the loading conditions are required in order to predict realistic breast deformations.

In a previous study (Lee et al., 2010b) earlier incarnations of the biomechanical models were used. It was found that the use of these FE models as a prior for FFD image alignment, significantly improved the accuracy of image alignment compared to either method applied independently. In contrast to the FE models of the breast phantom (Chapter 3) and breast (Chapter 4) in this thesis, the previous study did not account for the material stiffness heterogeneity. In addition, the boundary conditions were improved in this thesis by accounting for the frictional interactions between the compression plates and the phantom, where previously frictionless contact was applied, with kinematic constraints on nodes to prevent unrealistic deformations. Similarly, improvements were made to the breast models as described in Chapter 4, where tied contact constraints were used instead of fixed boundary conditions on the rib surface of the breast model. In this thesis, the alignment of the images for the volunteers differed from the alignment used in the previous study. In the current models, the alignment accounted for the rotation of the volunteers. This was achieved by digitising the respective rib surfaces on the prone and supine images, creating a surface mesh on the prone rib data, and aligning the supine data by minimising the RMSE of the Euclidean distances between each data point and the projected location on the prone rib surface. In the previous study, the rotation about the CC axis was assumed to be 180º (prone to supine) while the rotations about the other axes were assumed to be zero, and only the translation was optimised.

The absolute values of the block matching error measures cannot be directly compared to the previous study (Lee et al., 2010b) due to the difference in the rigid alignment of the prone and supine images. However, the relative differences in the three methods can be studied. Consistent results were achieved for Volunteer 1. For Volunteer 2, there was insubstantial improvement with using the FEM method in comparison to the FFD method in the previous work (mean: 8.7 mm vs. 8.9 mm, respectively, corresponding to a 2% difference), while in this chapter, FEM substantially outperformed FFD (mean: 4.14 mm vs. 6.05 mm,

respectively, corresponding to a 32% difference).

In this chapter, the deformations of the breasts from prone (required for MRI) to supine (required for ultrasound and surgery) gravity loading conditions were investigated. The accuracy of the biomechanical models in simulating these deformations was compared to two other image registration methods: FFD; and a hybrid FEM+FFD method. Statistical analysis of the block matching error measure revealed that FEM was substantially and significantly more accurate than the FFD method, while the hybrid method substantially outperformed both of the independent methods [Table 4]. The deformations of the breasts while under X-ray mammographic compression are also of clinical interest. In Chapter 6, the deformations of the breast from the prone gravity loaded state to the cranial-caudal compressed state was investigated.

Chapter 6: Finite element model-based multimodal image registration

6.1 Motivation and previous work

6.1.1 Motivation for multimodal image registration

X-ray mammography is commonly used to image the breast to assist in the diagnosis and management of breast cancer. During X-ray mammography, the breasts are compressed in the CC or MLO directions to increase image contrast and minimise the radiation dose that is absorbed by the breast tissues. Mammograms are considered the gold-standard for breast screening and are useful for locating tumours and micro-calcifications, which can often indicate the presence of cancer in the breasts (Ikeda, 2011).

In order to diagnose and manage breast cancer, clinicians often compare mammograms to help interpret the images. This comparison may be performed between images of the same breast over time to observe the temporal changes in the breast tissues. Alternatively, the asymmetry in the left and right breasts, or difference in the views of the same breast, taken at the same visit may be considered. Image registration algorithms have been proposed to align the information in the mammograms, either through feature-based methods (Kumar et al., 2001, Marias et al., 2005, Marti et al., 2006, Sultana et al., 2010, van Engeland et al., 2003, Wirth et al., 2002), intensity-based measures (Dıez et al., 2010, Periaswamy and Farid,

2003b, van Engeland et al., 2003), or a combination of both (Richard and Maidment, 2003).

A limitation of the two dimensional image registration applied for mammographic comparisons was that mammograms are two dimensional projections of the three dimensional breast tissues. Variations in the degree of compression, rotation of the breast, and angle of the compression plates can result in very different images. Thus it is generally impossible to recover the three dimensional deformation of the breast tissues using purely two dimensional transformations. Efforts to address this limitation include incorporating three dimensional information of the breast tissues derived from MRI of the breast (Behrenbruch et al., 2004, Kita et al., 2002).

Studies have also shown that combining information from multiple modalities can aid in the diagnosis of breast cancer (Malur et al., 2001). MR images of the breast are generally acquired with the patient in a prone position, with the breast hanging pendulously under the effect of gravity. In contrast, mammograms are obtained with an individual in an upright position and the breast compressed between two plates in the MLO or CC directions. The large deformations of the breast tissues between the two imaging modalities can make it difficult to co-localise information in the breast tissues. Efforts to simulate mammographic compression of the breast tissues from the prone gravity loaded shape of the breast include scaling, rotation, and translation (Marti et al., 2004), geometric transforms (Kita et al., 2002, Behrenbruch et al., 2003) or volume-preserving affine transformation of the three dimensional breast image (Mertzanidou et al., 2010). Though these methods allow for fast calculations, they provide a poor representation of the deformation of the breast tissues from the prone to compressed states. Earlier studies have found that affine transformations were insufficient to recover the non-linear deformations of the breasts between dynamic contrast enhanced MRI studies (Rueckert et al., 1999). In Rueckert et al. (1999), the deformation of the breast was due to patient motion (e.g. breathing artefacts) in the prone MR breast coil. Thus, for the much larger deformations of the breast tissues due to mammographic compressions, it is highly likely that such simple transformations are unsuitable.

6.1.2 Previous work on multimodal image registration

The majority of studies combining three dimensional breast images with two dimensional X-rays have focussed on four main areas: (i) to estimate the density of the breast tissues (Alonzo-Proulx et al., 2010, Hartman et al., 2008, Shih et al., 2010, van Engeland et al.,

2006); (ii) to track points of interest between medical images (Chung et al., 2008b, Kita et al., 2002, Qiu et al., 2004, Reynolds et al., 2011, Ruiter et al., 2006, Tanner et al., 2010, Zhang et al., 2007); (iii) to validate other registration algorithms for aligning X-ray images (Hipwell et al., 2007, Pinto Pereira et al., 2010, Van de Sompel and Brady, 2008); or (iv) to register the three dimensional MRI to two dimensional mammography images (Behrenbruch et al., 2004, Mertzanidou et al., 2010).

6.1.3 Previous work with finite element models to simulate X-ray mammographic and MR compressions

There is also a clinical need to be able to track features of interest (potential tumours) from the uncompressed contrast-enhanced MRI to the compressed breast state. For contrast enhanced MRI studies, a contrast agent is injected into a patient and dynamic images are acquired to follow the changes in the enhancement characteristics of the breast tissues over time. Malignant tumours tend to be well vascularised, having a faster and greater uptake of contrast agent in comparison to surrounding tissues (Warren and Coulthard, 2002). When lesions are identified in breast imaging, histological samples are typically taken out of the breast tissues for diagnostic purposes. Some lesions may be non-palpable and only identifiable using MR imaging. One technique used to obtain biopsies, or insert localisation wires, relies on compressing the breast tissues using a MR breast coil and inserting needles to an appropriate depth (Warren and Coulthard, 2002). However, accurate localisation of the region of interest in the breast tissues can be difficult as compression can cause changes in contrast enhancement of lesions (Heywang et al., 1989). Authors have proposed the use of FE models to simulate the compression of the breasts with the MR coil, for the accurate localisation of tumours (Azar et al., 2001, Chung, 2008, Chung et al., 2008a, Lee et al., 2010a, Ruiter et al., 2006, Samani et al., 2001, Tanner et al., 2009, 2011). Quantitative validation studies of compression simulations using FE models found that the mean errors for internal and skin surface deformations were around 5 mm or less (Azar et al., 2001, Chung et al., 2008b, Lee et al., 2010a, Ruiter et al., 2006, Tanner et al., 2011). Different modelling frameworks have been explored for FE models, based on linear elasticity (Azar et al., 2001, Hipwell et al., 2007, Ruiter et al., 2006, Schnabel et al., 2003, Van de Sompel and Brady, 2008) or finite elasticity (Carter et al., 2008, Chung et al., 2008a, Lee et al., 2010b, Pathmanathan et al., 2008, Rajagopal et al., 2007b, Reynolds et al., 2011, Ruiter et al., 2006, Samani et al., 2001). An oft-repeated criticism of using linear elasticity FE models is that

these methods are valid only for small deformations (<1%) and are therefore inaccurate for simulating large deformations, such as mammographic compressions of soft breast tissues where up to a 75% compression level has been reported (Reynolds et al., 2011).

In a number of studies, the ability of FE models to constrain the deformations of the breast tissues to be within physically realistic limits has been applied to warp breast images. Such FE-warped images were then used in the validation of other non-rigid registration frameworks. The deformations from the FE models were regarded as the 'gold standard', and the other methods were compared to the FE model deformation fields (Hipwell et al., 2007, Pinto Pereira et al., 2010, Schnabel et al., 2003, Van de Sompel and Brady, 2008). However, a lack of rigorous validation of these FE models leads to questions about the applicability of their FE derived deformations.

The deformation of the FE breast models due to compression has been modelled by either imposing displacement boundary conditions on the surface nodes or by including contact mechanics in the FE simulations. Nodal displacements on the outer surfaces of the breast model have alternatively been fixed (Tanner et al., 2006), prescribed based on compression plate displacement (Azar et al., 2001, Hipwell et al., 2007, Ruiter et al., 2006, Tanner et al., 2008, 2010, Zhang et al., 2007), or explicitly prescribed using the deformation field from another non-rigid registration algorithm such as free form deformation based on B-splines or fluid registration (Tanner et al., 2006, 2009, 2011). In the Tanner et al. studies (2006, 2009, 2011), non-rigid registration was performed on three dimensional images that were acquired before and during compression with a MR scanner. This non-rigid registration using FFD was used to provide kinematic information with which to prescribe the nodal displacements on the FE mesh. However, this three dimensional information of the breast deformations under compression is typically not collected in clinical practice, where X-ray mammograms represent the two dimensional projections of the compressed breast tissue.

Ruiter et al. (2006) sought to overcome this limitation by enforcing nodal displacements on the skin surface of the FE model based on the two dimensional contours of the model compared to the contour on the mammograms. However, explicitly defining the nodal displacements imposes unrealistic forces upon the FE model. This approach is the physical equivalent of having tethering points in the breast and pulling upon them. There are clearly no such boundary conditions on the breast tissues in the clinical situation.

Boundary conditions

In order to specify boundary conditions representing the compression pads, the location of the compression plates with respect to the breast is required. A patient may shift, resulting in breast tissue rotation about the roll (longitudinal) and yaw (vertical) axes. In addition, the amount of tissue that is compressed between the pads depends on the distance between the chest wall and the compression pads. In Tanner et al. (2008), statistical deformation models were created using FE models to investigate the variability of breast motion for mammographic compressions due to breast rolling, yawing, and translation with respect to the compression plates. Surface displacement boundary conditions were again used in these models, where the compression was simulated by displacing nodes on the skin surface of the breast model in the direction of the compression. Posterior surface nodes of the breast mesh were fixed in the direction of the surface normal, and the breast was further stabilised by fixing surface nodes along the mid-sagittal plane of the model so they did not deviate in the lateral direction. As noted previously, the limitation with this approach is that physically unrealistic forces are imposed on the skin surfaces of the FE models. In addition, the imposition of nodal displacement constraints instead of boundary conditions that reflect the physical constraints limits the ability of the FE models in predicting deformations.

Appropriate boundary conditions are important for the accuracy of FE model predictions. In contrast to prescribing displacement boundary conditions on the surface nodes of FE meshes, a more physically realistic approach has been investigated by incorporating contact mechanics in the FE models (Chung, 2008, Chung et al., 2008a, Reynolds et al., 2011). Contact mechanics have been used to model the interaction of the breast tissues with the compression plates and the ribs. Efforts were made by Chung et al. (2008b) to validate using non-linear finite element models of the breast to simulate breast compression using contact constraints, where MR images were obtained of the uncompressed and 32% compressed breasts with a volunteer lying in a prone position.

In this chapter, a novel framework for the multimodal three dimensional-two dimensional non-rigid registration of prone MRI to X-ray mammography using non-linear FE models is described. This method was systematically validated using uncompressed and (up to) 49% percentage compression MR and X-ray images of a breast phantom. The applicability of these techniques was then demonstrated using X-ray mammograms with the breast compressed to 52% from a breast cancer patient. The sensitivity of the material properties and

boundary conditions on X-ray mammographic compression simulations was assessed for this patient. An important contribution of this thesis was a novel automated method for defining the location and orientation of the compression plates based on the clinical images of the breasts. In previous work the boundary conditions and model parameters needed to be defined prior to the mechanics simulation (Hipwell et al., 2007, Pinto Pereira et al., 2010, Reynolds et al., 2011, Tanner et al., 2011). This optimisation framework was demonstrated on the parameters defining the location and orientation of the compression plates with respect to the breast, however it can likewise be used to estimate the other parameters of the FE model, such as stiffness values.

6.2 Error quantification for multimodality image registration using a breast phantom

In order to systematically validate the error at the stages of this modelling framework, MRI and X-ray images of a breast phantom were acquired. Using these ground truth clinical images, the repeatability of the compression experiments, X-ray simulation error and the error associated with the biomechanical model used to simulate the mammographic compression, were analysed. Various assumptions were made regarding the FE models of the breast phantom, including approximating the heterogeneous nature by varying the material stiffness across elements and neglecting the interface conditions between the boundaries of the inclusions and the bulk material. By establishing the error associated with the repeatability and reproducibility of the breast phantom compressions and the X-ray simulation code, the additional error due to the assumptions of the FE models could be investigated.

6.2.1 X-ray imaging of the breast phantom

To validate the techniques used for multimodal image registration, a breast phantom (Triple Modality Biopsy Training Phantom, Model 051, Computerized Imaging Reference Systems, Virginia, USA) was imaged before and during varying levels of compression in the equivalent AP and CC directions in a 1.5T MR scanner (MAGNETOM Avanto, Siemens, Munich, Germany) as described in Chapter 3. This breast phantom contains 12 distinct inclusions that are visible under both MR and X-ray imaging. The breast phantom was similarly imaged with a mammography system (Senographe DS, General Electric,

Connecticut, USA) under the following levels of compression: AP 24%, AP 29%, AP 34%, AP 37%, AP 46%, CC 27%, CC 32%, CC 37%, CC 39%, and CC 49% [Figure 6.1]. The mammogram dimensions were 1914 pixel x 2294 pixel with a 190 mm x 230 mm field of view.
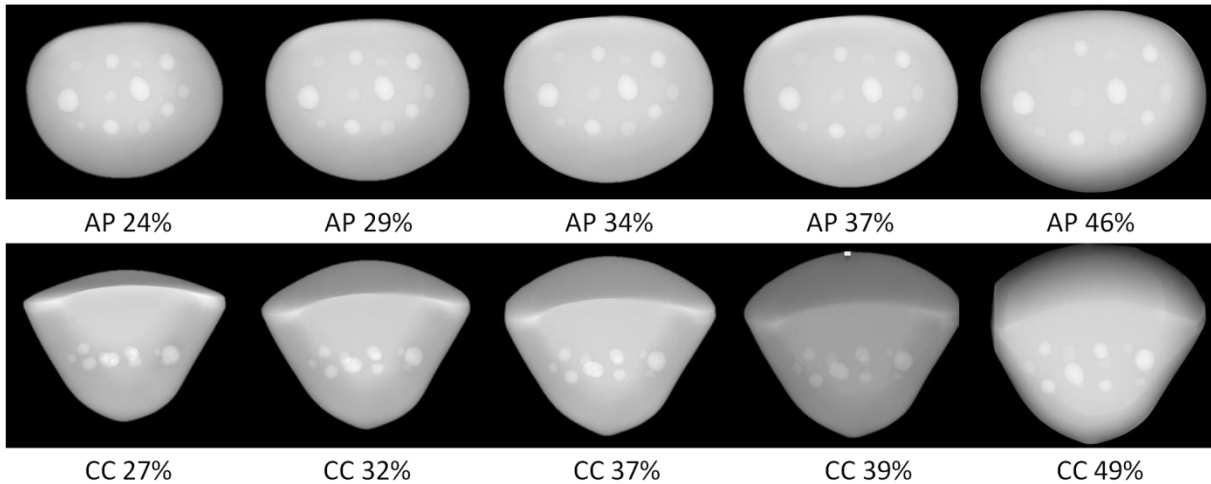
Figure 6.1: X-ray images of the breast phantom under various levels of compressions. AP: anterior-posterior and CC: cranial caudal compressions.

Statistical analysis

The repeatability and reproducibility of the breast phantom experiments were assessed using landmark-based methods (as described in Chapter 3). The centroid distances (CENT), surface distances (SMAD), and area overlaps (DICE) for the phantom and each of its twelve lesions were calculated between pairs of X-ray images. The means and standard errors of each of the landmark-based error measures for the two sets of data (repeatability and reproducibility experiments) were calculated. The differences between the repeatability and reproducibility experimental data give an indication of the error arising from recompressing the breast phantom in the compression device.

In addition, both frictional (no lubrication) and frictionless (with lubrication) experiments were conducted. The difference between experiments conducted with similar frictional conditions was compared against the difference between experiments conducted where dissimilar frictional conditions were used. The means and standard errors of each of the landmark-based error measures for the two sets of data (similar and dissimilar frictional conditions) were also calculated.

Normality was confirmed using the Shapiro-Wilk test, while equal variance was confirmed using the Levene test. The p value to reject normality and/or equal variance was set at $p \leq 0.05$. After confirming normality and equal variance of the data, the differences between the repeatability and reproducibility experiments were assessed using independent t-tests for each landmark-based error measure. Similarly, independent t-tests were used to assess the differences between experiments where similar frictional conditions were used in comparison to experiments where dissimilar frictional conditions were used.

Testing the repeatability of the X-ray mammographic imaging experiments

To test the repeatability of the X-ray mammographic experiments, the AP compression at 46% was repeated 6 times (MG1 – MG6) as shown in Figure 6.2. Mammographic images were obtained of the breast phantom on two separate days. Five of the experiments (MG1-MG5) were conducted on day one and one further experiment was conducted on day two (MG6). On the first day grid lines were etched into the compression plates. As the thickness of the compression plates were reduced at the grid line locations, fewer X-rays were deflected, resulting in higher mammographic intensity values at the grid line locations with respect to the rest of the plates [Figure 6.2]. For the imaging on day two, the compression plates were replaced with ones without grid lines [Figure 6.2]. In addition, no lubrication was used for the experiments conducted on day one (frictional experiments), while the plates and surface of the breast phantom were lubricated on day two (frictionless experiments).
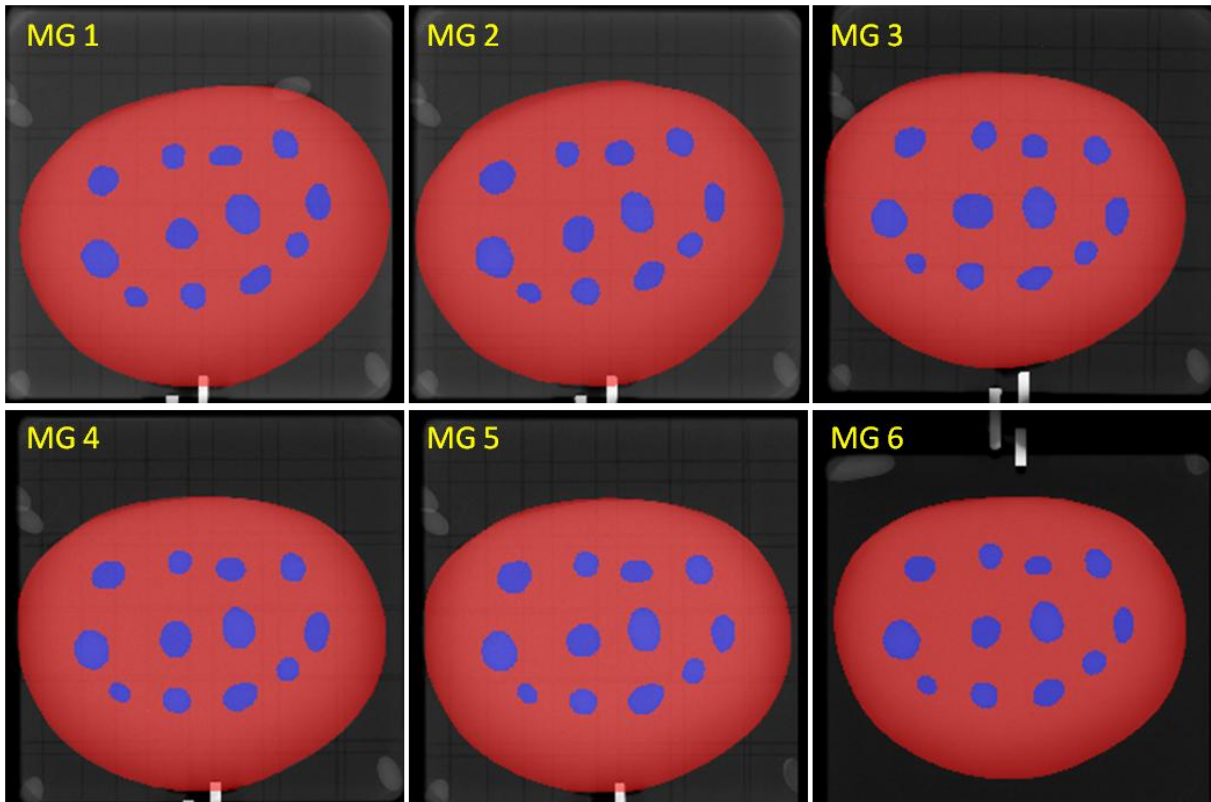
Figure 6.2: Six mammograms (MG1 – MG6) were obtained with the breast phantom placed under 46% compression in the AP direction. The inclusions (blue) and the breast phantom surface (red) were segmented from these images.

The inclusions and the outer contours of the breast phantom were segmented, as shown in Figure 6.2. The compression device was removed from, and replaced in the mammographic system, between each image acquisition; therefore the location of the breast phantom in each of the images is different for MG1 – MG6. Each of the six segmented images were rigidly registered to the remaining five segmented images, leading to 30 pairs of images for comparisons. Landmark-based error measures (CENT, SMAD, and DICE) were then calculated for each pair of images.

The breast phantom was not taken out of the compression device between MG1 and MG2, or between MG4 and MG5, but it was taken out and recompressed prior to the acquisition of the images for MG3, MG4, and MG6. Analysis of the similarity between MG1:MG2, and between MG4:MG5 provides an indication of the repeatability of the image acquisition as quantified by the difference in the image comparison metrics [Table 5]. In these cases, it was found that there was little difference between the images, with mean CENT and SMAD of less than 0.5 mm. Since a rigid transformation was used to register the images, this neglects

the projection differences in generating the images. This was a source of error as the X-rays pass through the breast phantom volume from a point source. An estimation of this projective error was calculated by using what is known about the geometry of the mammography system set-up and the relative locations of the breast phantom in the repeatability image pairs. The bounding boxes for the outer contours of the breast phantom were used to find the difference in the projections for the image pairs MG1:MG2 and MG4:MG5. The maximum surface distances between the image pairs were 0.46 mm for MG1:MG2 and 0.73 mm MG4:MG5. In addition, there will be errors associated with the manual segmentation and registration processes, as the rigid registration biases the result towards matching the outer contours of the breast phantom, where the area overlap for the bulk of the phantom was greater than 99%.

Table 5: Repeatability of the X-ray mammography experiments was tested by removing and then replacing the compression device on the mammography system (MG1:MG2 and MG4:MG5). The segmentations of the 12 individual masses and the outer contours of the breast phantom were used to calculate the means (±SE) of the centroid distances (CENT), surface distances (SMAD) and area overlaps (DICE).

	CENT (mm)	SMAD (mm)	DICE (%)
Mean ± SE (n=26)	0.49 ± 0.04	0.45 ± 0.03	92.0 ± 0.6

Testing the reproducibility of the mammographic compressions

Secondly, the reproducibility of the compression of the breast phantom was assessed using the comparison metrics. As noted in Section 6.2.1, during the experiments, the breast phantom was uncompressed and recompressed prior to the acquisition of MG3, MG4 and MG6. To investigate the reproducibility of the mammographic comparisons, the similarity between the experiments where the breast phantom was recompressed were assessed.

Independent t-tests indicated that there were significant differences when the breast phantom was uncompressed and then recompressed, compared with simply shifting the breast phantom on the mammography system for all the landmark-based measures of error ($p < 0.005$). Comparisons revealed that the physical differences, with regard to the mean of the feature-based error measures for experiments where the phantom was recompressed and experiments where the phantom was not recompressed, were small (<0.3mm) [Table 6].

Table 6: The reproducibility of the compression was tested by uncompressing and recompressing the breast phantom. The segmentations of the 12 individual masses and the outer contours of the breast phantom for 26 image pairs were used to calculate the mean (±SE) of the centroid distances (CENT), surface distances (SMAD) and area overlaps (DICE).

	CENT (mm)	SMAD (mm)	DICE (%)
Mean ± SE (n=338)	0.75 ± 0.03	0.64 ± 0.02	89.5 ± 0.3

The X-ray image MG6 was acquired on a separate day as part of the frictionless experiments, in contrast to the frictional experiments (MG1 - MG5). Independent t-tests found that there were statistically significant differences ($p < 0.005$, n=65) between recompressing with the same frictional conditions (no lubrication) and recompressing with different frictional conditions (no lubrication for MG1 - MG5 and with lubrication on the compression plates for MG6) for all three landmark-based measures of error. Comparisons revealed that the differences between recompressing with the same frictional conditions versus dissimilar frictional conditions were small with respect to the mean (±SE) for the centroid distances (CENT): 0.64 mm (±0.03 mm) vs. 0.91 mm (±0.05 mm), respectively, surface distances (SMAD): 0.51 mm (±0.02 mm) vs. 0.85mm (±0.05 mm), respectively, and area overlaps (DICE): 91.1% (±0.3%) vs. 87.0% (±0.6%), respectively. In Section 6.2.2, MR images of the breast phantom under compression with and without lubrication were compared with X-ray images where lubrication was used on the compression plates. The above errors are small in comparison to the MR image voxels size of 0.68 mm x 0.68 mm x 0.75 mm.

6.2.2 Generating pseudo X-rays from MR images

In addition to acquiring X-ray images of the breast phantom under compression, MR images were obtained of the breast phantom under various compression loads using a T_1 weighted FL3D pulse sequence in a 1.5T MR scanner (MAGNETOM Avanto, Siemens, Munich, Germany), as described Chapter 3. The image dimensions were 512 pixel x 512 pixel with a 350 mm x 350 mm field of view for 176 slices with 0.75 mm slice thickness.

There are two main methods for simulating X-ray images from a three dimensional image. A Monte Carlo approach has been used to simulate X-ray mammographic systems (Ay et al., 2004, Boone, 2002, Ng et al., 2000, Nigapruke et al., 2009, Peplow and Verghese, 2000, Sechopoulos et al., 2008). This is a stochastic method that tracks the progression of the X-ray photons as they progress through the tissue volume, allowing for the X-ray dosage to the breast tissues to be accurately calculated. This is of interest due to the increased risk of cancer

associated with high X-ray dosages. However, this method is computationally intensive and excessive for the purposes of simulating X-ray images of the compressed breasts to compare with experimental and clinical X-ray mammograms. An alternative is to use a ray-casting algorithm and X-ray attenuation coefficients to simulate X-ray images (Hipwell et al., 2007, Pinto Pereira et al., 2010).

X-rays from a point source in the mammography system were passed through the breast phantom. To simulate this process, Insight Segmentation and Registration Toolkit[5] (ITK) code using a perspective ray casting algorithm (DigitallyReconstructedRadiograph1 example) was employed to generate the digitally reconstructed radiographs from the three dimensional MR image (Hipwell et al., 2007). To simulate an X-ray image from the three dimensional MR image, parameters describing the set-up of the mammographic experiments were required [Figure 6.3]. The pseudo X-ray image changes with the location of the three dimensional image in the ray casting algorithm as the projection is from a point source.
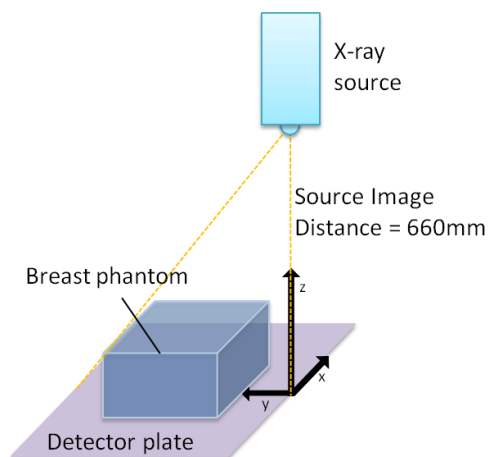
Figure 6.3: The projection of the three dimensional breast phantom image was set up to match the physical set-up of the mammography system. The x and y positions and rotation about the z-axis were optimised using rigid image registration.

The compression of the breast phantom was achieved with an independent compression device (see Chapter 3). This allowed the compression to be reliably repeated for both X-ray mammography and MR imaging experiments. The deformation of the breast phantom does not depend on the relative location of the breast phantom with respect to the X-ray mammography system. The location of the compressed three dimensional breast phantom

---

[5] http://www.itk.org/

with respect to the two dimensional X-ray image in the x-y plane was unknown. Therefore, the location of the three dimensional image was initially assumed to be in the centre of the output image for the ray casting algorithm [Figure 6.3]. The location of the three dimensional image was then varied to minimise the difference between the images, by combining the ray casting code with the Beer Lambert law (Section 2.1.1) to generate a combined pseudo X-ray and a rigid registration routine.

The process for determining the pseudo X-ray images is as follows: first the exterior surfaces of the breast phantom and the inclusions were segmented from the three dimensional MR images to create masks. The ray casting algorithm was used to generate projections through the MR masks. The pixel intensities on the projected images represented the distance that the X-ray beam travelled through each of the tissues. A 'raw' image was calculated using the Beer Lambert law (Section 2.1.1) with the calculated distances and the effective attenuation coefficients for this case. The 'raw' images were then processed to generate pseudo X-ray images [Figure 6.4], which were then rigidly registered to the actual X-ray images [Figure 6.1]. If the rigid registration transformation was less than a specified tolerance, then the optimisation was converged. Otherwise, the gradients of the translations in x and y and the rotation about the z axis from the resulting rigid transformation were used to perturb the location of the three dimensional image in the ray casting algorithm using ITK functionality.

MRI and mammography are fundamentally different imaging modalities, MR images are generated based on the spin of hydrogen nuclei in the breast tissues, while X-ray images are based on the interaction of X-ray photons with the breast tissues. Due to this difference, the image intensities between the two modalities cannot be directly mapped. The three dimensional MR images were segmented into the different tissues types and the effective attenuation coefficients were assigned to each of the segmented tissue types.

An effective attenuation coefficient can be calculated from the energy spectrum that is emitted by the mammography machine and the attenuation coefficient (see Section 2.1.1). The bulk of the breast phantom is made of material that radiographically simulates a 50% glandular 50% adipose breast (Bushberg et al., 2002). The cystic and solid masses were assumed to have similar radiographic characteristics as water and ductal infiltrating carcinoma, respectively (Hubbell and Seltzer, 2004). Based on the polyenergetic X-ray spectrum for a rhodium anode and rhodium filtering at 31 kV peak (Bushberg et al., 2002), the effective linear attenuation characteristics for the bulk, solid and cystic masses for the

breast phantom were estimated to be 79 m^{-1}, 104 m^{-1} and 99 m^{-1}, respectively.
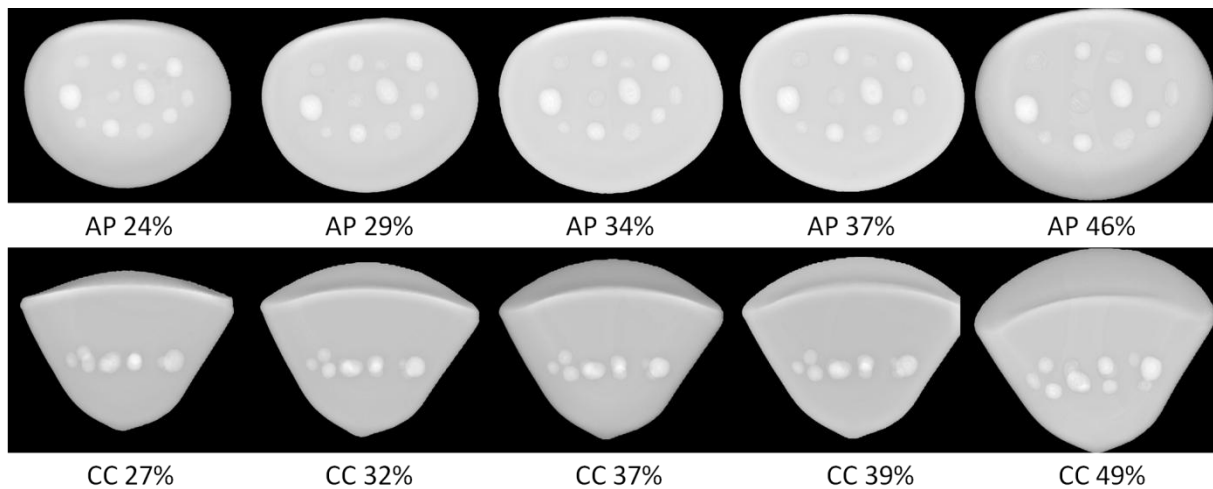
Figure 6.4: Pseudo X-rays derived from MRI of the phantom physically subjected to different levels of physical compression (indicated) in the anterior-posterior (AP) and cranial caudal (CC) directions.

6.2.3 Multimodality image registration using finite element modelling

In Section 6.2.2, a method for generating pseudo X-rays directly from three dimensional MR images was presented. Similar compression loads were applied during the experimental MR and X-ray studies for the above analysis of the breast phantom. In contrast, X-ray mammography and MR images of the breast are acquired with very different boundary and loading conditions. MR images of the breast are typically acquired with an individual lying in a prone position with the breasts subject to gravity loading. On the other hand, X-ray mammograms are obtained with the patient standing upright with the breast tissues highly compressed between two plates. As breasts are soft tissues, there were large deformations of the tissues between these two imaging modalities. In order to account for this difference in breast shape, a modelling framework was proposed, where biophysically-based FE models were used to simulate large mammographic compressions and the model deformations were used to warp the MR images accordingly.
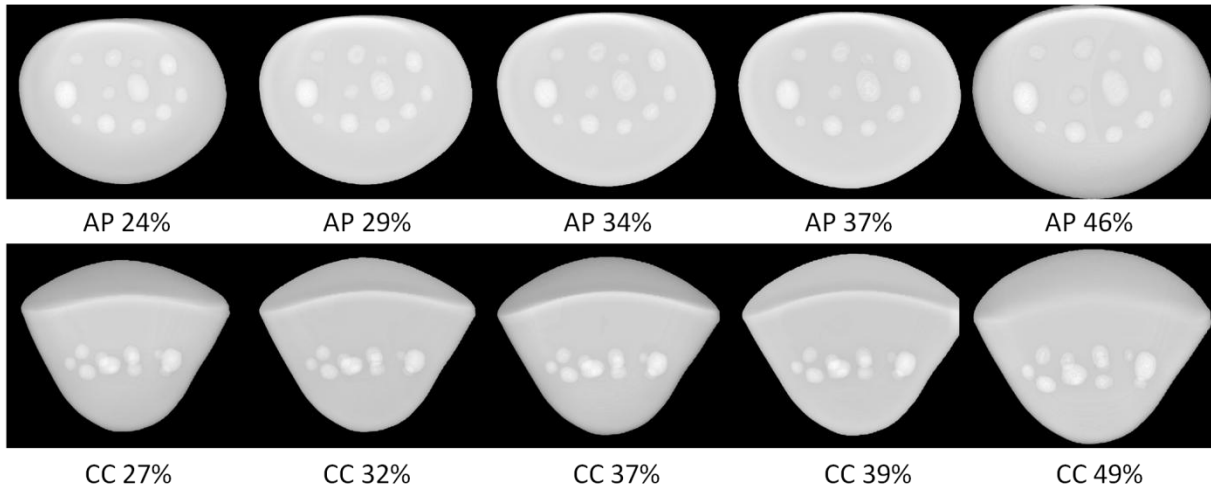
Figure 6.5: Pseudo X-rays derived from FE model-warped MRI, where the uncompressed images are subject to transformations derived from associated FE models for different levels of compression (indicated) in the anterior-posterior (AP) and cranial caudal (CC) directions. See text for details.

First, the FE modelling framework for multimodality registration requires validation. In addition to the compressed X-ray images described previously, the breast phantom was also imaged before compression in a MRI system (MAGNETOM Avanto 1.5T, Siemens, Munich, Germany) with its AP and CC axes aligned with gravity. In Chapter 3, finite element models of the breast phantom were developed and used to simulate different levels of AP and CC compression from the uncompressed MR images. The contact between the breast phantom and the compression plates was modelled using frictional and frictionless contact mechanics for the AP and CC simulations, respectively. The dimensionless static frictional coefficient for the contact between the breast phantom and the compression plates was determined experimentally to be μ=0.95 (see Section 3.3.4). As described in Chapter 3, a heterogeneous model was developed, whereby the inclusions within the phantom were assigned different neo-Hookean values, since they were composed of stiffer (solid inclusions) and softer (cystic masses) materials compared with the bulk material of the phantom: C_1^{bulk} =1.07 kPa, C_1^{solid}=6.73 kPa, and C_1^{cysts}=0.04 kPa.

The breast phantom was compressed and imaged using both a 1.5T MR scanner (MAGNETOM Avanto, Siemens, Munich, Germany) and a mammography system (Senographe DS, General Electric, Connecticut, USA) under varying levels of compression with the AP and CC axes of the phantom aligned with gravity. The MR images of the compressed phantom were used to generate pseudo X-rays as described in Section 6.2.2,

which could then be directly compared with the experimental X-rays [Table 7: MRI-MG]. The MR images of the uncompressed breast phantom were warped based on the deformations of the biomechanical models and pseudo X-rays were then generated from these warped images [Figure 6.5]. The error between the images can be given as the overall image similarity or by feature tracking. The masses inside the breast phantom were segmented in the three dimensional compressed and uncompressed MR images. The uncompressed images were warped using the FE models to simulated compressed images. The perspective ray casting algorithm was used to generate the two dimensional projections of the individual masses from the actual and simulated compressed images which were then compared with those from the experimental X-ray images [Table 7].

Table 7: The centroid distance (CENT), surface distance (SMAD) and area overlap (DICE) of the 12 masses and the outer contours of the breast phantom for 10 MR images (MRI-MG) and two FE models (MRI-FEM-MG) were used to assess the accuracy of the techniques used in the multimodality image registration.

	CENT (mm)	SMAD (mm)	DICE (%)
MRI-MG (n=130)	0.97 ± 0.06	0.96 ± 0.05	83.8 ± 0.7
MRI-FEM-MG heterogeneous (n=26)	2.46 ± 0.28	1.73 ± 0.13	65.3 ± 4.0

6.2.4 Quantification of errors of the multimodality image registration framework components

In this section, the errors associated with the different components of a pseudo X-ray generation algorithm were assessed. Specifically, the repeatability and reproducibility of the compression of the breast phantom [Table 6], the ray casting process used to project 3D MRI data into 2D pseudo X-rays registration [Table 7: MRI-MG], and the use of a biomechanical model to simulate the compression of the breast phantom from an uncompressed state model [Table 7: MRI-FEM-MG] were assessed.

Statistical analysis

The means and standard errors for the landmark-based measures of accuracies were calculated for the different stages of the multimodality framework. After confirming normality (Shapiro-Wilk test) and equal variance (Levene's test), the differences between the different stages of the framework were assessed using a one way ANOVA design. The p value to reject normality and/or equal variance was set at $p \leq 0.05$. Where a significant difference

(p≤0.05) between the models was detected, *post-hoc* comparisons were conducted using a Tukey's test.

Results

One-way ANOVA tests on the landmark-based measures of error (CENT, SMAD and DICE) revealed that there were significant differences ($p < 0.05$) between the different stages of the multimodality framework. *Post-hoc* comparisons indicated that there was significantly less error in the mean (±SE) for the recompression [Table 6] vs. MRI-MG experiments [Table 7] ($p < 0.005$) for all the landmark-based error measurements. However, this increase in error for the MRI-MG vs. recompression experiments was insubstantial and can be attributed to the difference in resolution in the MR and X-ray images (0.68 mm x 0.68 mm x 0.75 mm voxels vs. 0.1 mm x 0.1 mm pixels) and errors due to the ray casting code used to generate the pseudo X-rays. *Post-hoc* comparisons also found that there was significantly lower error ($p < 0.05$) for the MRI-MG vs. MRI-FEM-MG experiments for the mean (±SE) feature-based measures [Table 7]. These differences in the errors between these two data sets can be attributed to the inaccuracy of the FE model simulations.

To date, this is the first systematic analysis and validation of the different components of a modelling framework for multimodal image registration of MR and mammographic X-ray images. The mean error was quantified at each stage against ground truth X-ray images using feature-based measures: centroid error (CENT), surface distance (SMAD) and the area overlap (DICE) between the corresponding inclusions. The analysis focussed on the repeatability of the experimental image acquisition from an X-ray mammography system [Table 5], the repeatability of the compression of the breast phantom [Table 6], the simulation of X-ray images from three dimensional MR images [Table 7: MRI-MG], and lastly FE modelling of the large compression of soft bodies [Table 7: MRI-FEM-MG]. The errors associated with the experimental and the X-ray simulation code can be used to determine a baseline error, providing context for the errors associated with the FE models. This baseline error indicates the point at which further improvements to the FE model will no longer be effectual.

6.3   Application to breast MR and X-ray images

A modelling framework for three dimensional - two dimensional multimodality image

registration has now been analysed using the breast phantom and the localisation errors in the procedures have been quantified. In this section, the elements of the modelling framework for multimodality image registration for the optimisation of the FE model parameters were assembled, and the application of this method is demonstrated using clinical images from a breast cancer patient. This framework was then used to further improve the biomechanical model prediction of the breast shape during X-ray mammography.

6.3.1 Clinical data

Imaging data was acquired from a 57 year old patient where breast cancer was identified in both the MR and X-ray mammography images of the left breast. Written informed consent for use of this data was obtained from this patient, approved by the local ethics committee[6]. Axial T_1-weighted FL3D pulse sequences were used for MR image acquisition on a MR scanner (MAGNETOM Avanto 1.5T, Siemens, Munich, Germany). The image dimensions were 512 pixel x 512 pixel with a 360 mm x 360 mm field of view and with 208 slices with 0.75 mm slice thickness [Figure 6.6]. A mammography system (Senographe DS, General Electric, Connecticut, USA) was used to acquire X-ray mammograms [Figure 6.10]. An expert radiologist identified the locations of two small tumours for the patient. Based on this guidance, the tumour locations were segmented as shown in Figure 6.6.
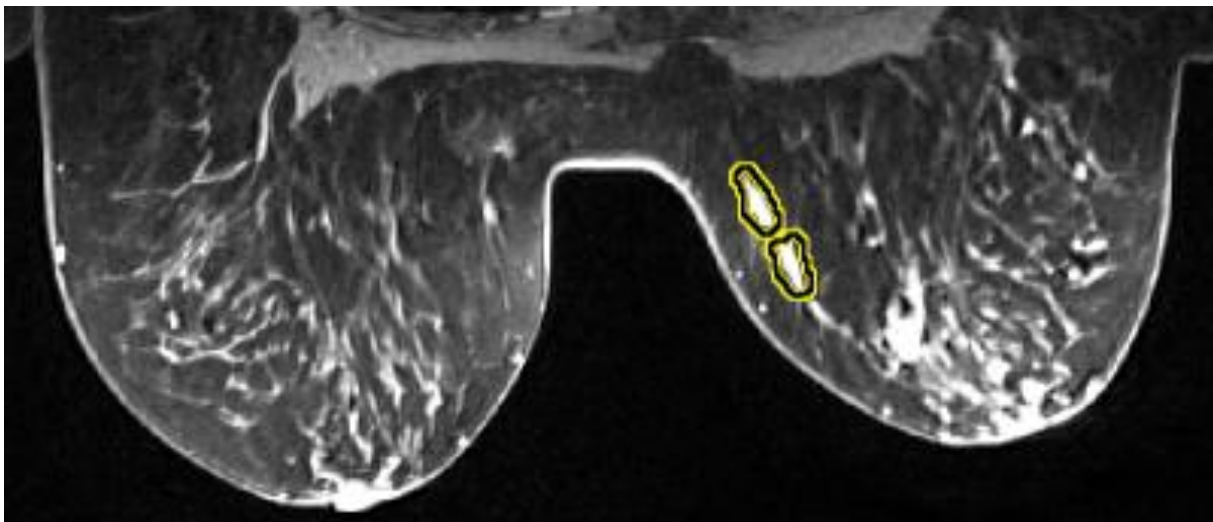
Figure 6.6: Prone MR images of a breast cancer patient with tumour locations outlined in yellow.

---

[6] Central Regional Ethics Committee (reference: CEN/09/09/EXP)

The prone breast MR images were used to construct pseudo X-ray mammograms. The prone MR image was masked using FE-model defined borders to isolate the breast tissues from the background and the rest of the torso. The masked MR breast images were then segmented into four tissue compartments (adipose, fibroglandular, muscle, and tumour) using an intensity threshold supplemented by manual editing of the segmentations in MIDAS to account for the spatial relationship between the structures as done previously in Chapter 4 (Freeborough et al., 1997).

The adipose, fibroglandular, muscle, and tumour masks were then warped based on the FE model compression deformations. A ray-casting algorithm was applied to the mask images to obtain two dimensional projections of the various components that make up the breast tissues, representing the length of tissue that the X-ray beam travelled through (Section 6.2). The Beer Lambert law was then used to determine the transmitted ray intensities by taking an exponential transform of the weighted sum of the path lengths, where the weights were the respective monoenergetic equivalent attenuation coefficients (see Section 2.1.1).

Based on the tables for the mass attenuation coefficients and densities and the X-ray spectrum that is generated at 29 kV peak with the rhodium anode and attenuated by the rhodium filter (Bushberg et al., 2002), monoenergetic equivalent attenuation coefficients for the adipose, glandular, skeletal muscle, infiltrating ductal carcinoma were set as: 73 m^{-1}, 92 m^{-1}, 110 m^{-1} and 109 m^{-1}, respectively.

The image representing the transmitted rays was then further processed by taking the negative natural logarithmic transform and then performing unsharp masking and thickness equalisation (Section 6.2) to simulate a 'for presentation' image that could be directly compared against the actual 'for presentation' mammogram images acquired for this patient.

6.3.2 Finite element models for mammographic compression of the breast

The skin and breast-rib boundaries were segmented from the three dimensional prone MR images using CMGUI[7] software and customised FE meshes were created by fitting a generic mesh to the segmented skin and rib data (Rajagopal, 2007). The breast tissues were modelled as isotropic and incompressible as defined by the neo-Hookean constitutive relation (Chung

---

[7] http://www.cmiss.org/cmgui

et al., 2008a). The initial homogeneous stiffness value for the breast tissues was set as C_1=400 Pa, which was determined previously from a manual parameter search (Reynolds et al., 2011).

Rajagopal et al. (2008b) demonstrated the importance of accurately defining the biomechanical unloaded reference state for large deformations of soft breast tissues under gravity loading. For mammographic compressions, the patient is orientated in an upright position, as opposed to the prone position required for MRI acquisition. Using the methods developed by Rajagopal (2007) the unloaded reference state was directly calculated from the known gravity deformed states of the breast for the patient. Currently the methods used for estimating the unloaded reference state of the breasts are unable to account for contact constraints between the breast tissues and the rib surface; thus the nodal displacements at the posterior surface of the breast mesh were fixed for this calculation.

For these simulations the breast tissues were modelled as an isolated body, although adjacent structures provide constraints on the in-vivo deformations. In a previous formulation of this model, the axilla edge of the breast model terminated at the shoulder region and to minimise unrealistic movement of the breast tissues from the shoulder region the elements associated with the axilla edge of the breast mesh were set to be two times stiffer than the rest of the mesh (Reynolds et al., 2011). This ad-hoc approach was formulated based on the effect of the constraint on the modelling, rather than through careful consideration of the actual physical constraints on the breasts. In the current formulation of the model, this ad-hoc approach was improved by assigning more realistic kinematic boundary conditions at the axilla, sternum, cranial, and caudal surfaces of the mesh to account for the restrictions imposed by the rest of the torso. The methods used here were based on those used previously for the prone to supine simulations described in Chapter 4.

FE implementation of finite deformation elasticity was used to simulate mammographic compressions in the CC direction. Gravity was not accounted for during the compression simulations. In earlier work on breast compressions it was found that including gravity in the simulations resulted in only minor differences in the model predictions (Chung, 2008). This indicates that for large compression simulations, the boundary forces play a greater role in the model deformations than the gravity force.

In contrast to the simulations used to define the unloaded reference state, contact mechanics

were used for the forward compression simulations, thus the nodal constraints on the rib surface of the breast mesh were removed, and tied contact constraints were imposed. In Chapter 4, tied contact mechanics was used to simulate the attachment of the breast tissues on the chest wall for both the prone to supine reorientation studies and the compression simulations.

Frictionless contact boundary conditions (see Chapter 2) were used to model the interaction between the breast tissues and the compression pads, whilst tied contact constraints (Chapter 4) were used to represent the breast-to-rib interface. The breast model used in this section was based on previous work (Reynolds et al., 2011), where the contact stiffness was set as 2 kPa/m, to ensure numerical convergence, and the tied stiffness value was set to be 10 kPa/m . The final distances between the compression plates were recorded as 64 mm, corresponding to 52% compression for this patient.

6.3.3 Improvements to the finite element model

The accuracy of the boundary conditions has a significant impact on the accuracy of the model simulations (Tanner et al., 2006). The boundary conditions for the breast tissues against the chest wall and the rest of the torso were investigated in Chapter 4 for prone to supine simulations and similar boundary conditions were imposed in the compression simulations. The amount of tissue that is compressed directly depends on the location of the compression plates with respect to the patient; however the location of the compression plates with respect to the uncompressed breast tissues is unknown.
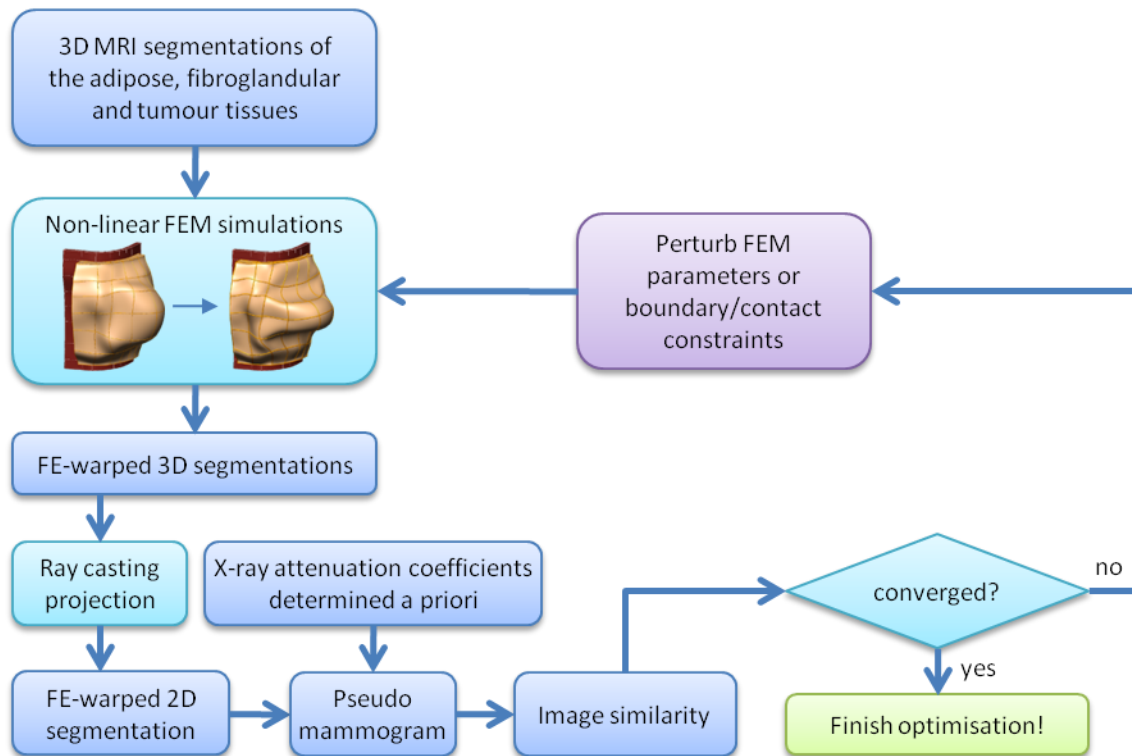
Figure 6.7: Framework for three dimensional-two dimensional multimodal image registration to estimate FE-model parameters such as mechanical properties and boundary conditions

The angle of the compression plates with respect to the patient can vary depending on how the patient positions her body during an X-ray mammogram. During the X-ray mammography procedure a patient can rotate about the yaw (vertical) axis, so that more/less axilla tissue is captured in the X-ray image [Figure 6.8]. In the initial model, this yaw angle of rotation was assumed to be 25° towards the axilla edge for the patient, based on a visual assessment comparing the shape of the unloaded reference mesh with the outline of the breast on the CC mammogram (Reynolds et al., 2011). This approach is highly subjective, depending on the modeller's judgement. An individual can also lean to the side resulting in breast rolling (rotation about central anterior-posterior axis) and in the initial model this roll angle was set to 0°. This rotational information is not captured (and would be hard to record) during mammographic image acquisition. Novel methods were developed to automate the plate alignment based on the mammographic images, and hence remove the subjective choices [Figure 6.7].

The nipple is one of the few consistent landmarks in the breast; therefore the nipple location in the pseudo mammogram and the clinical mammogram was used to determine the

translation of the compression plates. In this study, the yaw angle was then determined with a rigid rotation image registration algorithm in the axial plane centered about the nipple location, with normalised cross correlation as the similarity measure. The relative location of the compression plates was then updated and the FE simulation was repeated until the yaw rotation angle and translation parameters were converged as shown in Figure 6.8. Updating the yaw angle (to 41º towards the axilla) and translation substantially improved the accuracy of the tumour alignment, with the surface distance measure (SMAD) of the tumour reducing from 16.4 mm to 8.4 mm [Figure 6.8].
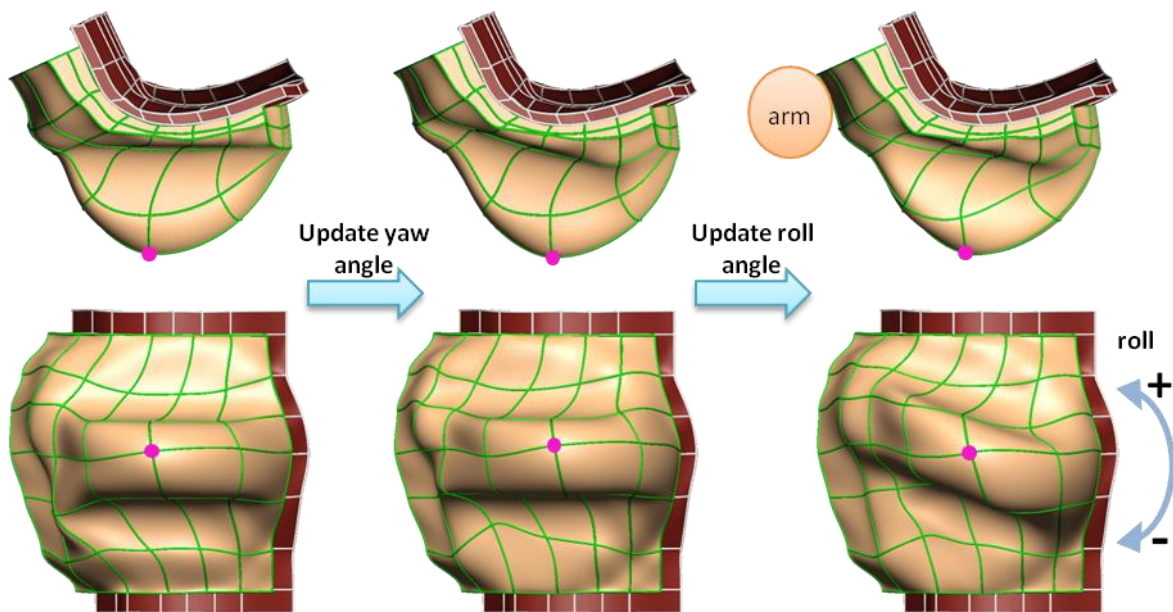
Figure 6.8: The location of the compression plates was altered by updating the yaw and roll angles and by translating the images to align the nipple landmark, based on image similarity.

Once the yaw and translational parameters were optimised, the effects of breast rolling and varying the material stiffness of the breast tissues were considered. The feature that is of most interest is the breast tumour (previously identified by an expert in both the MR and mammographic images). Therefore, the sensitivity of the breast rolling was assessed at 10º intervals from -40º to 20º using the SMAD of the tumour as an accuracy measure [Figure 6.9]. In a previous study by Tanner et al. (2008), the roll was assumed to deviate by ±30º. Negative roll corresponds to the patient rotating her body slightly to allow for more of the tissue in the shoulder region to be compressed between the plates as shown in Figure 6.8. It can be seen in Figure 6.9, that the error remains relatively constant between roll angles of -30º to -10º, with the minimum at a roll angle of -20º. The corresponding SMAD values were -

30º: 3.6 mm; -20º: 3.1 mm; and -10º: 4.7 mm. This indicates that the roll needs to be accounted for in simulating mammographic compressions; however it is sufficient to be accurate to within ± 10º.
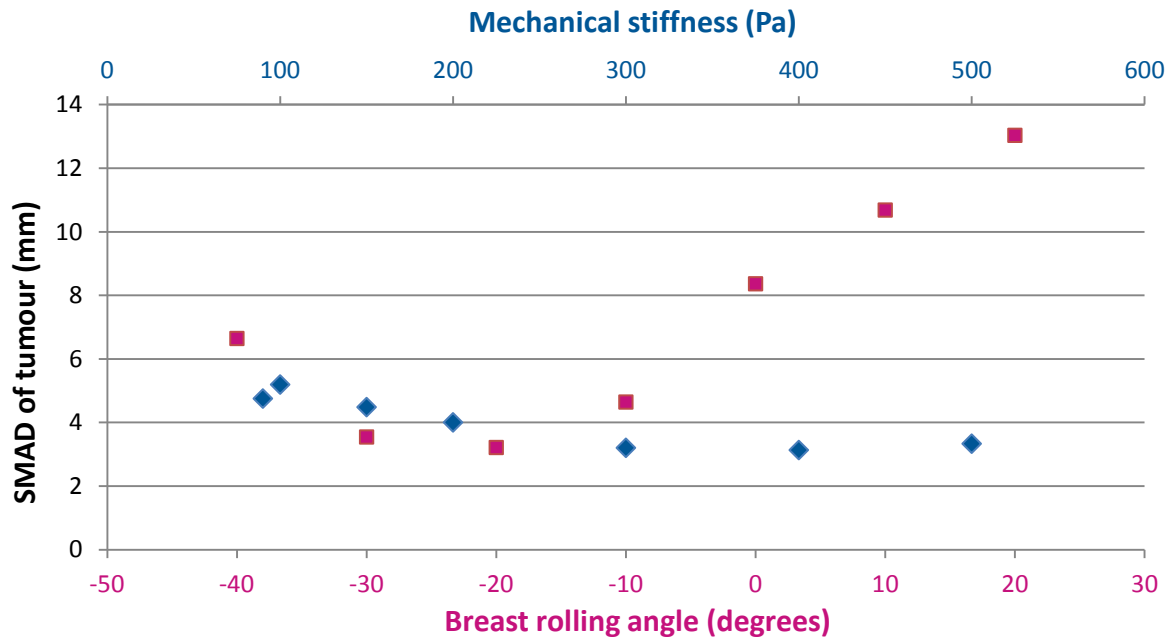
Figure 6.9: Sensitivity of the FE model deformations with respect to the rolling angle (squares) of the compression plates and the mechanical stiffness (diamonds) of the breast model.

In Figure 6.10, it can be seen how improving the location of the compression plates with respect to the breast substantially improves the accuracy of the alignment of the breast tumour. It should be noted however, that only a single case study was considered here, where the tumour used to measure the accuracy of the model was located near the sternum and close to the skin. The sensitivity of the localisation accuracy with respect to the roll angle is likely to be greater in this case compared to the case where a tumour resides closer to the centre of the breast.
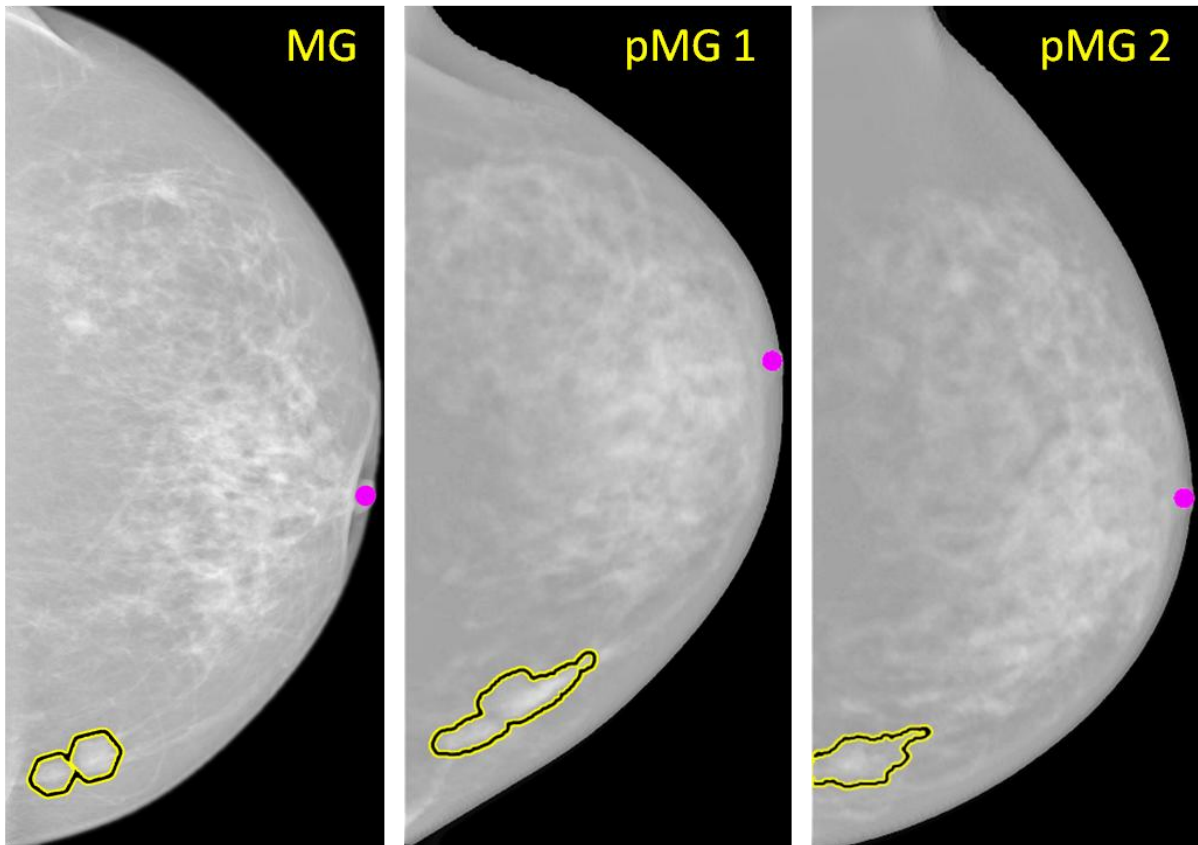
Figure 6.10: Mammogram (MG) and pseudo-mammograms (pMG) for a breast cancer patient with the segmented tumours outlined in yellow and the nipple location highlighted in pink. Initially the plates were positioned based on a visual alignment (pMG 1). Automatically updating the translation, yaw and roll of the compression pad with respect to the breast tissues substantially improved the alignment (pMG 2).

The sensitivity of the material stiffness was also investigated using the tumour as a landmark measure. In Chapter 4, the material stiffnesses for Volunteers 1 and 2 were found to be 125 Pa and 300 Pa, respectively, for the homogeneous model with tied contact constraints applied to the rib surface. The neo-Hookean stiffness values that were investigated for the compression simulations for the patient ranged from 90 Pa to 500 Pa. With reference to Figure 6.9, the SMAD for the tumour was approximately constant between 300 Pa and 500 Pa, with the error ranging from 3.1 mm to 3.3 mm. This indicates that the kinematics of the compression deformation mode has a greater effect on the accuracy of the FE model deformations in comparison to the mechanical properties of the breast tissues. It is thus likely that individual specific estimation of the mechanical properties may not be required for reliable compression simulations, although this needs to be verified using additional patient data.

6.4   Limitations and future work

In this chapter, a novel modelling framework for three dimensional-two dimensional non-rigid image registration using FE modelling has been presented and its accuracy was quantified using ground truth clinical images. The sensitivity of the material properties and boundary conditions on mammographic compression simulations was assessed for a breast cancer patient using this framework.

6.4.1 Boundary conditions

The majority of studies using FE models to simulate large breast compressions prescribe nodal displacement on the outer (skin) surface of the model, which introduces unrealistic forces into the models (Hipwell et al., 2007, Ruiter et al., 2006, Schnabel et al., 2003, Tanner et al., 2006, 2010, 2011). In contrast, the patient model presented in this chapter accounts for the interactions between compression plates and the breast using contact mechanics coupled with finite elasticity to predict the deformations of the breast under compression. In this chapter, a novel automated method for defining the location of the compression plates based on the multi-modal imaging of the breasts has been proposed and demonstrated.

In Figure 6.10 it can be seen that even though the tumour and nipple locations for the pseudo mammogram generated from the updated model (pMG 2) match well with the clinical mammogram, the alignment of the axilla region (upper section of the image) did not align as well. The FE model of the breast excludes the shoulder and arm region as well as the rest of the torso. The movement of the shoulder and arm, and their subsequent effects on the model, were not accounted for during these simulations despite the belief that arm motion is likely to have a substantial influence on the breast deformations. Kinematic boundary conditions were applied at the edges of the breast mesh to account for these structures, with selected nodes on the skin-cranial edge fixed to account for the effect of the shoulder. During the MR image acquisition, the patient pressed her arms against her body. If the patient had lifted her arm during the mammogram acquisition, this could have the effect of increasing the skin tension around the shoulder region leading to decreased deformation in this region.

6.4.2 Skin-plate interactions

The interaction between the compression plates and the breast tissues has been modelled

using frictionless contact mechanics. However, observations in the clinical environment indicate that a slip-stick condition of frictional contact may be a more suitable representation of these interactions. Frictional contact requires the static frictional coefficient to be specified. In earlier studies, the (dimensionless) frictional coefficient was given as 0.2, although the method for determining this value was not described (Shih et al., 2010, Yin et al., 2004). This appears to be a rather low frictional coefficient for the contact between the compression plates and the breast skin, in the context of earlier studies on the frictional properties of the skin.

Naylor (1955) found that the frictional coefficient between polythene and skin on the anterior surface of the tibia was 0.5. Later studies have found that different locations on the body can result in different frictional properties (Cua et al., 1990, Zhang and Mak, 1999). Cua et al., (1990) investigated a range of anatomical regions: forehead, postauricular upper arm, abdomen, thigh, ankle, lower back, and upper back against Teflon. The closest anatomical region to the breast would be the abdomen or upper back, which were found to have frictional coefficients against Teflon of 0.12 and 0.25, respectively. However, Teflon typically has much lower friction against human skin compared to the plastic compression plates. Zhang and Mak (1999) investigated the frictional properties of human skin in six anatomical regions (palm and dorsam of the hand; and the anterior and posterior sides of the forearm and leg) against a larger range of materials (aluminium, nylon, silicone, cotton sock and Pelite). In this study, the closest material to the plastic compression plates was silicone, which against skin, was found to have mean frictional coefficients ranging from 0.47 to 0.93 across the different anatomical regions for 10 subjects.

The frictional coefficient of skin for each individual is dependent on the underlying structure, the amount of oil or sweat, and its suppleness or smoothness. Physically measuring the frictional coefficient for each patient when they get a mammogram is unrealistic. However, using the modelling framework developed in this chapter, this property can be determined for each individual.

6.4.3 Mechanical properties

The biomechanical model for this patient assumed that the breast tissues were isotropic, homogeneous, and incompressible. In Chapter 4, the importance of accounting for the stiffnesses of adipose, fibroglandular, and muscular tissue was explored. It was found that

incorporating information about the heterogeneity of the breast tissues significantly improved the accuracy of prone to supine reorientation FE simulations (Section 4.6). Studies have found that fibroglandular tissues have a 5-fold to 50-fold greater stiffness compared to the adipose tissues (Gefen and Dilmoney, 2007). Moreover, the elastic modulus of the muscles underlying the breasts is reported to range from 0.75 kPa to 30 kPa (Gefen and Dilmoney, 2007). Incorporating the mechanical properties of the different tissue types may improve the alignment of the axilla region of the breast model. Further work is required to investigate the effects of incorporating heterogeneity and altering the position of the arm during the compression simulations.

Tumourous tissues have an even greater difference in stiffness, with studies reporting up to 100-fold greater stiffness in comparison to normal breast tissues (O'Hagan and Samani, 2009). It has also been postulated that tumours have a stiffening effect on the surrounding normal tissues, due to spiculations extending out from the tumour (Wessel et al., 2010). Therefore, accounting for these effects of the tumours (particularly large tumours) in the patient's breast is likely to improve the accuracy of the compression simulations.

6.4.4 Summary

In this chapter, a novel modelling framework to determine FE model parameters from MR and X-ray clinical images has been demonstrated on a single case study. Promising results have been acquired for this patient study, where it was shown that the kinematics of the FE model simulations had a substantial impact on the accuracy of the simulations. A novel method was developed to determine the yaw and translation of the compression plates in the FE model simulations from the multi-modal medical images. The sensitivity to breast roll and material stiffness of the breast tissues was also investigated by considering the tumour localisation accuracy. Best results were found with a roll between -10º and -30º, whereas the localisation error was relatively insensitive to mechanical stiffness. However, only a single case study with one feature (tumour) for the error measure was considered. In order to be clinically useful, this framework would need to be tested on more patient studies with tumours in different locations. In addition, the accuracy of more landmarks or regions would need to be considered for each study.

The advantage of the biomechanical models of the breast used in this thesis is that they are capable of predicting the deformations of breast tissues under different loading conditions. In

contrast to the majority of studies using FE models to simulate large deformations of the breasts, where displacement of nodes on the skin surface are explicitly prescribed, the boundary conditions used in this thesis are more physically realistic. In this way, a biomechanical model can be customised for each patient and different deformations can be *predicted* by altering the loading conditions or boundary conditions to simulate the physical environment. For example, a biomechanical model of the breast that can accurately simulate the deformations of the breast from the prone to compressed states, could also be used to predict the breast shape in the supine orientation (for example, for application to ultrasound imaging or surgery). A biophysical tool that can co-localise features of interest across modalities will help clinicians in the diagnosis and management of breast cancer.

Chapter 7: Conclusions and future work

7.1. Summary

The overall goal of this research is to develop a modelling framework that can aid clinicians in the interpretation of breast images from multiple views and imaging modalities. To that end, biophysically-based models of the breast have been developed and used to simulate the deformations of the breast under gravity and compressive loads. In this thesis, techniques for integrating FE modelling and image processing methods were developed and validated using a breast phantom. A novel application of a block matching method was used to inform the modelling and improve the reliability of the physically-based FE models of the breasts.

7.2. Breast phantom studies

Modelling large deformations of the breast is a complex problem, due to the various structures that make up and surround the breast, such as adipose, fibroglandular, muscle, and skin tissues. In addition, the breast is not an isolated organ and the surrounding structures provide physical constraints on the problem. A breast phantom was therefore used to investigate aspects of the modelling framework because it allows greater control over its deformations and boundary conditions (for example, by imaging the breast phantom under varying degrees of compression (see Chapter 3)).

Compression was simulated using finite elasticity coupled with contact constraints for both frictional and frictionless cases. The structures inside the breast phantom were alternatively

modelled as homogeneous and heterogeneous, and the accuracy of the models were assessed using conventional landmark-based methods and the block matching approach.

Evaluation of the results between the model simulations and the experimental images led to the following conclusions:

1. Statistical analysis indicated that the block matching comparison measure is a suitable unbiased alternative to landmark-based methods in assessing the accuracy of the internal deformations of the breast phantom. The block matching method is preferable to the landmark-based measure as it allows the FE model predictions to be automatically evaluated on a three dimensional regional basis over the whole breast.
2. Techniques were developed to take into account the heterogeneous structures of the breast phantom. Statistical analysis of the results between the homogeneous versus the heterogeneous FE models revealed that the latter provided significantly more accurate compressive deformations.

7.3. Clinical studies

Two types of breast deformations were considered in this thesis: prone to supine reorientation (Chapter 4 and Chapter 5); and prone to CC mammographic compression (Chapter 6). Simulating prone to supine deformations is of clinical importance, as MR images of the breast are typically acquired with a patient in a prone position, whereas ultrasound imaging, biopsy and surgery are generally performed while the patient lies in a supine orientation.

Mammographic compression was also simulated using the experience from modelling the breast deformations from prone to supine gravity loading states. Clinical images of a breast cancer patient were acquired with the breast under prone gravity loading in the MRI scanner, and under CC compression using an X-ray mammography system. The novel framework for fusing information from three dimensional MR and two dimensional X-ray images was validated using breast phantom images and then applied to the clinical breast images. Using an iterative process, the parameters of the model were updated and the image alignment between the three dimensional MR images and the X-ray mammogram was improved.

Evaluation of the block matching comparison between the biomechanical model predictions and the clinical images led to the following conclusions:

1. In contrast to applying zero-displacement boundary conditions on the rib surface of the breast model, a more realistic sliding contact constraint was implemented. Accounting for the sliding of the breast tissues over the chest wall significantly improved the accuracy of the model predictions.

2. In earlier work, the breast tissues were modelled as homogeneous tissue. However, the breasts are composed of adipose and fibroglandular tissues and in addition, muscle was incorporated into the breast models. These tissue groups have distinct mechanical properties and accounting for the different stiffnesses of these tissues significantly improved the accuracy of the image alignment.

3. The FE method was significantly more accurate than FFD-based method in registering prone with breast supine images. However, there is still room for further improvement of the FE models of the breast. In the meantime a hybrid method where FFD method is applied following the FE method allows for better alignment between prone and supine breast images.

4. Biomechanical models were used to align three dimensional MR and two dimensional X-ray images. An iterative process was used to estimate the unknown relative location of the compression plates and the mechanical properties of the breast tissues. Initial results indicated that kinematic constraints play a greater role in the accuracy of the model predictions than the mechanical properties of the breast tissues.

7.4. Future work

In order to improve the robustness and reliability of the modelling framework a number of areas require further work. Various assumptions were made about the breast tissues and their boundary conditions to simulate the large deformations between the different loading conditions. These assumptions will need to be investigated to assess their effect on the accuracy of the model predictions.

1. The neo-Hookean material relation models the breast tissues as an isotropic incompressible material. In recent work by Tanner et al. (2011), it was found that simulating the breast tissues as anisotropic (where the antero-posterior direction was stiffest) significantly improved the accuracy of compression simulations. The models used in the Tanner studies, assumed that the prone gravity loaded orientation was the biomechanical reference state. The justification for using anisotropic material laws was

that the prone gravity loaded state imposes stretching in the AP direction already. In addition, it was postulated that the effects of the Cooper's ligaments, which lie preferentially in the AP direction, were accounted for with anisotropy. It will need to be investigated as to whether or not this finding still holds true when the loads on the breast in the prone orientation are taken into account, as was done in this thesis.

2. Cooper's ligaments and the retromammary bursa allow the breast tissues to slide on the muscle tissues that make up the chest wall. In the forward simulations, the interactions of the posterior surface of the breast models and the rib surface were modelled using contact constraints. However, to determine the unloaded reference state from the gravity loaded state (using the 'reverse method'), software limitations required that zero-displacement boundary conditions be applied on the nodes that were in contact with the compression plate or the rib surface for the breast phantom and breast model simulations, respectively. Contact mechanics still remains to be implemented in CMISS for the 'reverse method'. In addition, the boundary conditions of the breast tissues are an approximation to the actual constraints on the breast. Currently the models of the breasts extend in the antero-posterior axis from the skin to the ribs. However, as discussed in Chapter 2, the conventional description of the breast tissues places it on top of the pectoral muscles. Sliding contact constraints need to be implemented between the pectoral muscle surface and the breast tissues.

3. In Chapter 6, the interactions between the breast tissues and the compression plates were modelled using frictionless contact constraints. However, no lubrication was used between the compression plates and the breast, so frictional contact would be more appropriate. To model frictional interactions between surfaces, additional parameters need to be defined: the tied stiffness penalty; and the frictional coefficient (see Chapter 2). As shown in Chapter 6, a framework has now been developed where the image similarity between the FE model warped image and the clinical image can be used to estimate parameters (such as the frictional parameters) in the model. It will need to be investigated to see whether the use of frictional, instead of frictionless contact constraints will lead to a significant improvement on the accuracy of the model simulations.

4. In this thesis, the modelling framework was used to fuse the information from MR and X-ray mammography modalities. In addition to MR imaging, ultrasound is also used as a common adjunct to mammography for the diagnosis and management of breast cancer. The modelling framework presented here can be extended to take into account the images

acquired from ultrasound, with further work required to align two dimensional ultrasound images with the FE-warped MR images.

5. Finally, only a limited number of human studies have been presented. The prone to supine studies were carried out on two volunteers, whereas the breast compression study was demonstrated on a single breast cancer patient. These studies were intended to demonstrate the clinical applicability of the modelling framework. However, there is a risk that the conclusions drawn from these limited studies may not be applicable to all situations. There is a wide variety of breast shapes and sizes, and to demonstrate that the methods presented in this thesis can be a useful tool in the clinical environment, a greater number of patient cases, with tumour locations in different regions, will need to be studied to validate this modelling framework across a range of women.

In this thesis, breast models simulating deformations due to gravity and compressive loads were investigated. MR images of the breast in the prone gravity loaded orientation were warped, according to the model deformations, to simulate the compressed state (required for X-ray mammography) and the supine gravity loaded state (required for ultrasound). A framework for multimodality image registration, combining FE modelling techniques with image processing methods, was demonstrated in this thesis. The use of a biophysically-based modelling tool that can co-localise features across breast imaging modalities, including X-ray mammography, MRI and ultrasound, will potentially aid clinicians in the diagnosis and management of breast cancer.

Appendix A: Convergence analysis of the models

Mesh convergence analysis was carried out for the breast phantom (Chapter 3 and Chapter 5) and the breast models used for the two volunteers (Chapter 4 and Chapter 5) to minimise the effect of the discretisation error during the mechanics simulations. The models were used to simulate mechanics (compression for the phantom and prone to supine reorientation for the volunteers). As there is no analytic solution for the deformation of the breast phantom and breasts, the highest refinement in each of the directions was used as the 'gold standard'. To test for convergence of the models, the FE-warped images of the unrefined and refined models were compared using the NCC metric (Eq. 2.1).

For the breast phantom, the unrefined model (2043 geometric solution degrees of freedom (DOF)) was refined once in each of the xi directions, where xi 1 was defined along the circumference of the phantom, xi 2 was defined as from the skin to the center of the phantom, and xi 3 was defined as from the apex to base of the phantom. The homogeneous 45% CC compression model, with C_1 set to be 1 kPa, was used to warp the uncompressed images. The NCC values (a measure of the image similarity) ranged from 99.5% to 99.9% [Table 8].

For the volunteers, the unrefined model (4606 geometric solution degrees of freedom) was refined once in each xi direction. The xi directions were defined as follows: xi 1 was defined as right side of the body to left side of the body; xi 2 was defined as from head to toe; and xi 3 was defined as from skin to rib. The homogeneous models with fixed boundary conditions on the rib surface, with C_1 set as 80 Pa and 122 Pa for Volunteers 1 and 2, respectively, were used to warp the prone images. For Volunteer 1, the image similarity, given as NCC, was

found to range from 99.3% to 99.7% [Table 9]. For Volunteer 2, the NCC value was found to range from 99.5% to 99.7% [Table 10].

Due to the need to maintain computational efficiency and the relatively small differences in the images it was concluded that the original (unrefined) models were sufficiently converged for both volunteers and the phantom.

Table 8: Phantom convergence analysis. The unrefined model was refined once in each xi direction. The NCC values were calculated for each refinement.

	Refine in xi 1	Refine in xi 2	Refine in xi 3
Model			
Geometric solution DOF	3891	4045	3891
NCC value	0.997	0.999	0.995

Table 9: Volunteer 1 model convergence analysis. The unrefined model was refined once in each xi direction. The NCC values were calculated for each refinement.

	Refine in xi 1	Refine in xi 2	Refine in xi 3
Model			
Geometric solution DOF	8343	7507	7735
NCC value	0.994	0.997	0.993

Table 10: Volunteer 2 model convergence analysis. The unrefined model was refined once in each xi direction. The NCC values were calculated for each refinement.

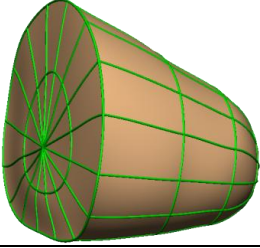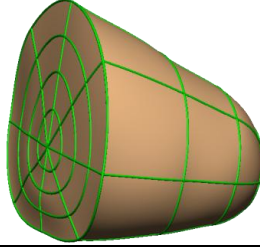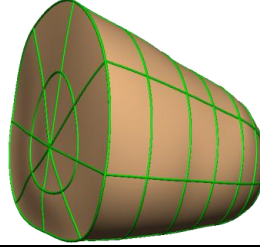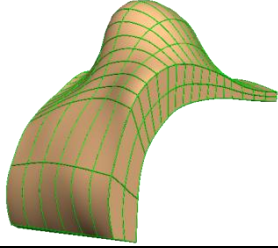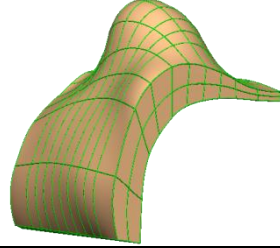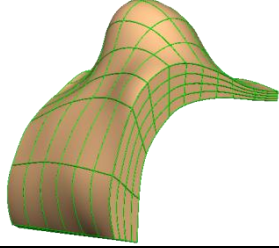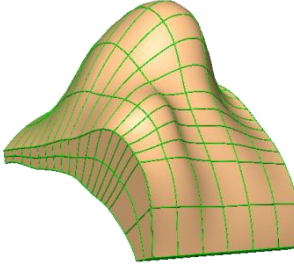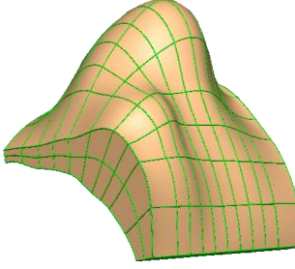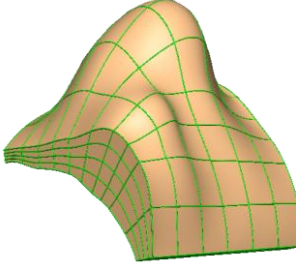|	Refine in xi 1	Refine in xi 2	Refine in xi 3
Model			
Geometric Solution DOF	8343	7507	7735
NCC value	0.997	0.996	0.995

References

ALONZO-PROULX, O., PACKARD, N., BOONE, J. M., AL-MAYAH, A., BROCK, K. K., SHEN, S. Z. & YAFFE, M. J. 2010. Validation of a method for measuring the volumetric breast density from digital mammograms. *Phys Med Biol,* 55**,** 3027-44.

ANDERSON, J. E. 1983. *Grant's Atlas of Anatomy,* Baltimore, Williams & Wilkins.

ATKIN, R. J. & FOX, N. 1980. *An introduction to the theory of elasticity*, Longman.

AY, M. R., SHAHRIARI, M., SARKAR, S., ADIB, M. & ZAIDI, H. 2004. Monte carlo simulation of x-ray spectra in diagnostic radiology and mammography using MCNP4C. *Phys Med Biol,* 49**,** 4897-917.

AZAR, F. S., METAXAS, D. N. & SCHNALL, M. D. 2001. A deformable finite element model of the breast for predicting mechanical deformations under external perturbations. *Acad Radiol,* 8**,** 965-75.

BABARENDA GAMAGE, T. P., RAJAGOPAL, V., NIELSEN, P. M. F. & NASH, M. P. 2011. Patient-specific modeling of breast biomechanics with applications to breast cancer detection and treatment. *In:* GEFEN, A. (ed.) *Patient-Specific Modeling in Tomorrow's Medicine.* Springer Berlin Heidelberg.

BAKER, L. H. 1982. Breast cancer detection demonstration project: five-year summary report. *CA Cancer J Clin,* 32**,** 194-225.

BEHRENBRUCH, C. P., MARIAS, K., ARMITAGE, P. A., YAM, M., MOORE, N. R., ENGLISH, R. E., CLARKE, P. J., LEONG, F. J. & BRADY, J. M. 2004. Fusion of contrast-enhanced breast MR and mammographic imaging data. *Br J Radiol,* 77**,** S201-S208.

BERG, W. A., GUTIERREZ, L., NESSAIVER, M. S., CARTER, W. B., BHARGAVAN, M., LEWIS, R. S. & IOFFE, O. B. 2004. Diagnostic accuracy of mammography, clinical examination, US, and MR imaging in preoperative assessment of breast cancer. *Radiology,* 233**,** 830-49.

BICK, U. & DIEKMANN, F. 2010. Digital Mammography. *Medical Radiology,*. Berlin, Heidelberg: Springer-Verlag Berlin Heidelberg.

BONET, J. & WOOD, R. D. 1997. *Nonlinear continuum mechanics for finite element analysis*, Cambridge University Press.

BOOKSTEIN, F. L. 1989. Principal warps - thin-plate splines and the decomposition of deformations. *IEEE Trans. on Pattern Analysis and Machine Intelligence,* 11**,** 567-585.

BOONE, J. M. 2002. Normalized glandular dose (DgN) coefficients for arbitrary X-ray

spectra in mammography: computer-fit values of Monte Carlo derived data. *Med Phys,* 29**,** 869-75.

BUSHBERG, J. T., SEIBERT, J. A., LEIDHOLDT, J. E. M. & BOONE, J. 2002. *The essential physics of medical imaging,* Philadelphia, Pa. ; London, Lippincott Williams & Wilkins.

CARTER, T. J., TANNER, C., BEECHEY-NEWMAN, N., BARRATT, D. & HAWKES, D. 2008. MR Navigated Breast Surgery: Method and Initial Clinical Experience. *Lecture Notes in Computer Science,* 5242**,** 356-363.

CARTER, T. J., TANNER, C., CRUM, W. R., BEECHEY-NEWMAN, N. & HAWKES, D. J. 2006. A framework for image-guided breast surgery. *Lecture Notes in Computer Science,* 4091**,** 203-210.

CARTER, T. J., TANNER, C. & HAWKES, D. J. 2009. Determining material properties of the breast for image-guided surgery. *Proceedings of SPIE Medical Imaging,* 7621.

CHUNG, J. H. 2008. *Modelling mammographic mechanics.* PhD Thesis, University of Auckland.

CHUNG, J. H., RAJAGOPAL, V., LAURSEN, T. A., NIELSEN, P. M. & NASH, M. P. 2008a. Frictional contact mechanics methods for soft materials: application to tracking breast cancers. *J Biomech,* 41**,** 69-77.

CHUNG, J. H., RAJAGOPAL, V., NIELSEN, P. M. & NASH, M. P. 2008b. Modelling mammographic compression of the breast. *Lecture Notes in Computer Science,* 5242**,** 758-65.

COOPER, A. 1840. *On the anatomy of the breast,* London, Longman, Orme, Green, Brown, and Longmans.

CRUM, W. R., TANNER, C. & HAWKES, D. J. 2005. Anisotropic multi-scale fluid registration: evaluation in magnetic resonance breast imaging. *Physics in Medicine and Biology,* 50**,** 5153-5174.

CUA, A. B., WILHELM, K. P. & MAIBACH, H. I. 1990. Frictional properties of human skin: relation to age, sex and anatomical region, stratum corneum hydration and transepidermal water loss. *Br J Dermatol,* 123**,** 473-9.

DEL PALOMAR, A. P., CALVO, B., HERRERO, J., LOPEZ, J. & DOBLARE, M. 2008. A finite element model to accurately predict real deformations of the breast. *Med Eng Phys,* 30**,** 1089-97.

DıEZ, Y., OLIVER, A., LLAD´O, X. & MARTI, R. 2010. Comparison of registration methods using mammographic images. *IEEE International Conference on Image Processing***,** 4421-4424.

DRAKE, R., VOGL, W., MITCHELL, A. W. M., TIBBITTS, R. & RICHARDSON, P. 2008. *Gray's Atlas of Anatomy*, Churchill Livingstone.

EGOROV, V., KEARNEY, T., POLLAK, S. B., ROHATGI, C., SARVAZYAN, N., AIRAPETIAN, S., BROWNING, S. & SARVAZYAN, A. 2009. Differentiation of benign and malignant breast lesions by mechanical imaging. *Breast Cancer Res Treat,* 118**,** 67-80.

FREEBOROUGH, P. A., FOX, N. C. & KITNEY, R. I. 1997. Interactive algorithms for the segmentation and quantitation of 3-D MRI brain scans. *Computer Methods and Programs in Biomedicine,* 53**,** 15-25.

GALEA, A. & HOWE, R. 2003. Mammography registered tactile imaging. *In:* AYACHE, N. & DELINGETTE, H. (eds.) *Surgery Simulation and Soft Tissue Modeling.* Springer Berlin / Heidelberg.

GEFEN, A. & DILMONEY, B. 2007. Mechanics of the normal woman's breast. *Technol Health Care,* 15**,** 259-71.

GUO, Y., SIVARAMAKRISHNA, R., LU, C. C., SURI, J. S. & LAXMINARAYAN, S. 2006. Breast image registration techniques: a survey. *Med Biol Eng Comput,* 44**,** 15-26.

HALL-FINDLAY, E. J. & EVANS, G. R. D. 2010. Aesthetic and reconstructive surgery of the breast. Edinburgh: Saunders/ Elsevier.

HAN, L., HIPWELL, J., MERTZANIDOU, T., CARTER, T., MODAT, M., OURSELIN, S. & HAWKES, D. 2011. A hybrid FEM-based method for aligning prone and supine images for image guided breast surgery. *IEEE International Symposium on Biomedical Imaging: From Nano to Macro***,** 1239-1242.

HARMS, S. E. & FLAMIG, D. P. 2001. Breast MRI. *Clin Imaging,* 25**,** 227-46.

HARTMAN, K., HIGHNAM, R., WARREN, R. & JACKSON, V. 2008. Volumetric assessment of breast tissue composition from FFDM images. *In:* KRUPINSKI, E. (ed.) *Digital Mammography.* Springer Berlin / Heidelberg.

HELVIE, M. A., CHAN, H. P., ADLER, D. D. & BOYD, P. G. 1994. Breast thickness in routine mammograms: Effect on image quality and radiation dose. *American Journal of Roentgenology,* 163**,** 1371-1374.

HEYWANG, S. H., WOLF, A., PRUSS, E., HILBERTZ, T., EIERMANN, W. & PERMANETTER, W. 1989. MR imaging of the breast with Gd-DTPA: use and limitations. *Radiology,* 71.

HIPWELL, J. H., TANNER, C., CRUM, W. R., SCHNABEL, J. A. & HAWKES, D. J. 2007. A new validation method for x-ray mammogram registration algorithms using a projection model of breast x-ray compression. *IEEE Trans. on Med. Imag.,* 26**,** 1190-1200.

HUBBELL, J. H. & SELTZER, S. M. 2004. Tables of x-ray mass attenuation coefficients and mass energy-absorption coefficients. National Institute of Standards and Technology,Gaithersburg, MD.

IKEDA, D. M. 2011. *Breast imaging,* Philadelphia, PA, Elsevier/Mosby.

JEMAL, A., BRAY, F., CENTER, M. M., FERLAY, J., WARD, E. & FORMAN, D. 2011. Global cancer statistics. *CA Cancer J Clin,* 61**,** 69-90.

KERDOK, A. E., JORDAN, P., LIU, Y., WELLMAN, P. S., SOCRATE, S. & HOWE, R. D. 2005. Identification of nonlinear constitutive law parameters of breast tissue. *2005 ASME Summer Bioengineering Conference.*

KITA, Y., TOHNO, E., HIGHNAM, R. & BRADY, M. 2002. A CAD system for the 3D location of lesions in mammograms. *Med Image Anal,* 6**,** 267-73.

KLEIN, A., ANDERSSON, J., ARDEKANI, B. A., ASHBURNER, J., AVANTS, B., CHIANG, M.-C., CHRISTENSEN, G. E., COLLINS, D. L., GEE, J., HELLIER, P., SONG, J. H., JENKINSON, M., LEPAGE, C., RUECKERT, D., THOMPSON, P., VERCAUTEREN, T., WOODS, R. P., MANN, J. J. & PARSEY, R. V. 2009. Evaluation of 14 nonlinear deformation algorithms applied to human brain MRI registration. *NeuroImage,* 46**,** 786-802.

KLEIN, R., AICHINGER, H., DIERKERT, J., JANSEN, J. T. M., JOITE-BARFU, S., SABEL, M., SCHULZ-WENDTLAND, R. & ZOETELIEF, J. 1997. Determination of average glandular dose with modern mammography units for two large groups of patients. *Phys. Med. Biol.,* 42**,** 651-671.

KROL, A., UNLU, M. Z., BAUM, K. G., MANDEL, J. A., LEE, W., COMAN, I. L., LIPSON, E. D. & FEIGLIN, D. H. 2006. MRI/PET nonrigid breast-image registration using skin fiducial markers. *Phys Med,* 21 Suppl 1**,** 39-43.

KROUSKOP, T. A., WHEELER, T. M., KALLEL, F., GARRA, B. S. & HALL, T. 1998. Elastic moduli of breast and prostate tissues under compression. *Ultrason Imaging,* 20**,** 260-74.

KROUSKOP, T. A., YOUNES, P. S., SRINIVASAN, S., WHEELER, T. & OPHIR, J. 2003. *Differences in the compressive stress-strain response of infiltrating ductal carcinomas with and without lobular features: implications for mammography and elastography,* Silver Spring, Dynamedia.

KUMAR, S., SALLAM, M. & GOLDGOF, D. 2001. Matching point features under small nonrigid motion. *Pattern Recognition,* 34**,** 2353-2365.

LANGER, K. 1978. On the anatomy and physiology of the skin: I. The cleavability of the cutis. *British journal of plastic surgery,* 31**,** 3-8.

LAURSEN, T. A. 2002. *Computational contact and impact mechanics: Fundamentals of modeling interfacial phenomena in nonlinear finite element analysis*, Springer.

LEE, A. W. C., RAJAGOPAL, V., CHUNG, J. H., NIELSEN, P. M. F. & NASH, M. P. 2010a. Method for validating breast compression models using normalised cross correlation. *Computational Biomechanics for Medicine IV.* Springer.

LEE, A. W. C., SCHNABEL, J., RAJAGOPAL, V., NIELSEN, P. M. F. & NASH, M. P. 2010b. Breast image registration by combining finite elements and free-form deformations. *Lecture Notes in Computer Science,* 6136**,** 736-743.

LEWIS, J. P. 1995. Fast normalised cross-correlation. *Vision Interface***,** 120-123.

LORENZEN, J., SINKUS, R., BIESTERFELDT, M. & ADAM, G. 2003. Menstrual-cycle dependence of breast parenchyma elasticity: estimation with magnetic resonance elastography of breast tissue during the menstrual cycle. *Invest Radiol,* 38**,** 236-40.

MACÉA, J. R. & FREGNANI, J. H. T. G. 2006. Anatomy of the thoracic wall, axilla and breast. *International Journal of Morphology,* 24**,** 691-704.

MALUR, S., WURDINGER, S., MORITZ, A., MICHELS, W. & SCHNEIDER, A. 2001. Comparison of written reports of mammography, sonography and magnetic resonance mammography for preoperative evaluation of breast lesions, with special emphasis on magnetic resonance mammography. *Breast Cancer Res,* 3**,** 55-60.

MALVERN, L. E. 1969. *Introduction to the mechanics of a continuous medium,* Englewood Cliffs, N.J., Prentice-Hall.

MARIAS, K., BEHRENBRUCH, C., PARBHOO, S., SEIFALIAN, A. & BRADY, M. 2005. A registration framework for the comparison of mammogram sequences. *IEEE Trans Med Imaging,* 24**,** 782-790.

MARTI, R., RABA, D., OLIVER, A. & ZWIGGELAAR, R. 2006. Mammographic registration: proposal and evaluation of a new approach. *Lecture Notes in Computer Science,* 4046.

MCKNIGHT, A. L., KUGEL, J. L., ROSSMAN, P. J., MANDUCA, A., HARTMANN, L. C. & EHMAN, R. L. 2002. MR elastography of breast cancer: preliminary results. *Am J Roentgenol,* 178**,** 1411-7.

MERTZANIDOU, T., HIPWELL, J. H., CARDOSO, M. J., TANNER, C., OURSELIN, S. & HAWKES, D. J. (eds.) 2010. *X-ray mammography - MRI registration using a volume-preserving affine transformation and an EM-MRF for breast tissue classification*: LNCS.

NAYLOR, P. F. 1955. The skin surface and friction. *Br J Dermatol,* 67**,** 239-46.

NG, K. P., KWOK, C. S. & TANG, F. H. 2000. Monte Carlo simulation of X-ray spectra in mammography. *Phys Med Biol,* 45**,** 1309-18.

NIGAPRUKE, K., PUWANICH, P., PHAISANGITTISAKUL, N. & YOUNGDEE, W. 2009. A comparison of mammographic X-ray spectra: simulation with EGSnrc and experiment with CdTe detector. *J Radiat Res (Tokyo),* 50**,** 507-12.

O'HAGAN, J. J. & SAMANI, A. 2009. Measurement of the hyperelastic properties of 44 pathological ex vivo breast tissue samples. *Phys Med Biol,* 54**,** 2557-69.

PANDYA, S. & MOORE, R. G. 2011. Breast development and anatomy. *Clin Obstet Gynecol,* 54**,** 91-5.

PARKIN, D. M., BRAY, F., FERLAY, J. & PISANI, P. 2005. Global cancer statistics, 2002. *CA Cancer J Clin,* 55**,** 74-108.

PATHMANATHAN, P., GAVAGHAN, D. J., WHITELEY, J. P., CHAPMAN, S. J. & BRADY, J. M. 2008. Predicting tumor location by modeling the deformation of the breast. *IEEE Trans Biomed Eng,* 55**,** 2471-80.

PEPLOW, D. E. & VERGHESE, K. 2000. Digital mammography image simulation using Monte Carlo. *Med Phys,* 27**,** 568-79.

PERIASWAMY, S. & FARID, H. 2003a. Elastic registration in the presence of intensity variations. *IEEE Trans. on Med. Imag.,* 22**,** 865-874.

PERIASWAMY, S. & FARID, H. 2003b. Elastic registration in the presence of intensity variations *IEEE Trans. on Med. Imag.,* 22**,** 865-874.

PERIASWAMY, S., WEAVER, J. B., JR., D. M. H. & KOSTELEC, P. J. 1999. Automated multiscale elastic image registration using correlation. *Proceedings of SPIE Image Processing,* 3661**,** 828-838.

PINTO PEREIRA, S. M., HIPWELL, J. H., MCCORMACK, V. A., TANNER, C., MOSS, S. M., WILKINSON, L. S., KHOO, L. A., PAGLIARI, C., SKIPPAGE, P. L., KLIGER, C. J., HAWKES, D. J. & SILVA, I. M. 2010. Automated registration of diagnostic to prediagnostic x-ray mammograms: evaluation and comparison to radiologists' accuracy. *Med Phys,* 37**,** 4530-9.

POULOS, A., MCLEAN, D., RICKARD, M. & HEARD, R. 2003. Breast compression in mammography: How much is enough? . *Australasian Radiology,* 47**,** 121-126.

QIU, Y., GOLDGOF, D., LI, L., SARKAR, S., ZHANG, Y. & ANTON, S. 2004. Correspondence recovery in 2-view mammography. *IEEE International Symposium on Biomedical Imaging: Nano to Macro,* 1**,** 197-200.

RAJAGOPAL, V. 2007. *Modelling breast tissue mechanics under gravity loading.* PhD Thesis, University of Auckland.

RAJAGOPAL, V., CHUNG, J., BULLIVANT, D. P., NIELSEN, P. M. & NASH, M. P. 2008a. Determining the finite elasticity reference state from a loaded configuration *International Journal for Numerical Methods in Engineering,* 1**,** 1434-1451.

RAJAGOPAL, V., CHUNG, J. H., BULLIVANT, D., NIELSEN, P. M. F. & NASH, M. P. 2007a. Determining the finite elasticity reference state from a loaded configuration. *International Journal for Numerical Methods in Engineering,* 72**,** 1434-1451.

RAJAGOPAL, V., LEE, A. W. C., CHUNG, J. H., WARREN, R., HIGHNAM, R. P., NASH, M. P. & NIELSEN, P. M. 2008b. Creating individual-specific biomechanical models of the breast for medical image analysis. *Academic Radiology,* 15**,** 1425-36.

RAJAGOPAL, V., LEE, A. W. C., CHUNG, J. H., WARREN, R., HIGHNAM, R. P., NIELSEN, P. M. & NASH, M. P. 2007b. Towards tracking breast cancer across medical images using subject-specific biomechanical models. *Lecture Notes in Computer Science,* 4791**,** 651-658.

RAJAGOPAL, V., NIELSEN, P. M. & NASH, M. P. 2010. Modeling breast biomechanics for multi-modal image analysis--successes and challenges. *Wiley Interdiscip Rev Syst Biol Med,* 2**,** 293-304.

REDDY, B. S. & CHATTERJI, B. N. 1996. An FFT-based technique for translation, rotation, and scale-invariant image registration. *IEEE Trans. on Imag. Proc.,* 5**,** 1266-1271.

REYNOLDS, H. M., PUTHRAN, J., DOYLE, A., JONES, W., NIELSEN, P. M., NASH, M. P. & RAJAGOPAL, V. 2011. Mapping breast cancer between clinical x-ray and MR images. *Computational Biomechanics for Medicine: Soft Tissues and the*

Musculoskeletal System. Springer.

RICHARD, F. J. P. & MAIDMENT, P. R. B. A. D. A. 2003. Non-rigid registration of mammograms obtained with variable breast compression: a phantom study. *Lecture Notes in Computer Science,* 2717**,** 281-290.

RIGGIO, E., QUATTRONE, P. & NAVA, M. 2000. Anatomical study of the breast superficial fascial system: the inframammary fold unit. *European Journal of Plastic Surgery,* 23**,** 310-315.

ROBINSON, D. M. & SCRIMGER, J. W. 1991. Monoenergetic approximately of a polyenergetic beam: a theoretical approach. *Br J Radiol,* 64**,** 452-4.

ROHLFING, T., MAURER, C. R., JR., BLUEMKE, D. A. & JACOBS, M. A. 2003. Volume-preserving nonrigid registration of MR breast images using free-form deformation with an incompressibility constraint. *IEEE Trans. on Med. Imag.,* 22**,** 730-41.

ROOSE, L., LOECKX, D., MOLLEMANS, W., MAEST, F. & SUETENS, P. 2008. Adaptive boundary conditions for physically based follow-up breast MR image registration. *Med Image Comput Comput Assist Interv,* 11**,** 839-46.

RUECKERT, D., SONODA, L. I., HAYES, C., HILL, D. L. G., LEACH, M. O. & HAWKES, D. J. 1999. Nonrigid registration using free-form deformations: Application to breast MR images. *IEEE Trans. on Med. Imag.,* 18**,** 712-721.

RUITER, N. V., STOTZKA, R., MULLER, T. O., GEMMEKE, H., REICHENBACH, J. R. & KAISER, W. A. 2006. Model-based registration of X-ray mammograms and MR images of the female breast. *Ieee Transactions on Nuclear Science,* 53**,** 204-211.

RUITER, N. V., ZHANG, C. P., BAKIC, P. R., CARTON, A. K., KUO, J. & MAIDMENT, A. D. A. 2008. Simulation of tomosynthesis images based on an anthropomorphic software breast tissue phantom. *Medical Imaging 2008: Visualization, Image-Guided Procedures, and Modeling, Pts 1 and 2,* 6918**,** I9182-I9182.

SABEL, M. S. 2009. *Surgical foundations: essentials of breast surgery,* Philadelphia, PA, Mosby/Elsevier.

SAMANI, A., BISHOP, J., YAFFE, M. J. & PLEWES, D. B. 2001. Biomechanical 3-D finite element modeling of the human breast using MRI data. *IEEE Trans Med Imaging,* 20**,** 271-9.

SAMANI, A. & PLEWES, D. 2004. A method to measure the hyperelastic parameters of ex vivo breast tissue samples. *Phys Med Biol,* 49**,** 4395-405.

SAMANI, A., ZUBOVITS, J. & PLEWES, D. 2007. Elastic moduli of normal and pathological human breast tissues: an inversion-technique-based investigation of 169 samples. *Phys Med Biol,* 52**,** 1565-76.

SARDANELLI, F., GIUSEPPETTI, G. M., PANIZZA, P., BAZZOCCHI, M., FAUSTO, A., SIMONETTI, G., LATTANZIO, V. & DEL MASCHIO, A. 2004. Sensitivity of MRI versus mammography for detecting foci of multifocal, multicentric breast cancer in fatty and dense breasts using the whole-breast pathologic examination as a gold standard. *Am. J. Roentgenol.,* 183**,** 1149-1157.

SCHNABEL, J. A., TANNER, C., CASTELLANO-SMITH, A. D., DEGENHARD, A., LEACH, M. O., HOSE, D. R., HILL, D. L. & HAWKES, D. J. 2003. Validation of nonrigid image registration using finite-element methods: application to breast MR images. *IEEE Trans. on Med. Imag.,* 22**,** 238-47.

SECHOPOULOS, I., SURYANARAYANAN, S., VEDANTHAM, S., D'ORSI, C. J. & KARELLAS, A. 2008. Radiation dose to organs and tissues from mammography: Monte Carlo and phantom study. *Radiology,* 246**,** 434-43.

SHIH, T. C., CHEN, J. H., LIU, D., NIE, K., SUN, L., LIN, M., CHANG, D., NALCIOGLU, O. & SU, M. Y. 2010. Computational simulation of breast compression based on

segmented breast and fibroglandular tissues on magnetic resonance images. *Phys Med Biol,* 55**,** 4153-68.

SIVARAMAKRISHNA, R. 2005. 3D breast image registration--a review. *Technol Cancer Res Treat,* 4**,** 39-48.

SKAANE, P. 2011. Screening of breast cancer. *In:* KAHÁN, Z. & TOT, T. (eds.) *Breast Cancer, a Heterogeneous Disease Entity.* Springer Netherlands.

SULTANA, A., CIUC, M., STRUNGARU, R. & FLOREA, L. 2010. A new approach in breast image registration. *IEEE International Conference on Intelligent Computer Communication and Processing***,** 149-154.

TANNER, C., HIPWELL, J. H. & HAWKES, D. J. 2008. Statistical deformation models of breast compressions from biomechanical simulations. *Lecture Notes in Computer Science,* 5116**,** 426-432.

TANNER, C., HIPWELL, J. H., HAWKES, D. J. & SZEKELY, G. 2010. Breast shapes on real and simulated mammograms. *Lecture Notes in Computer Science,* 6136**,** 540-547.

TANNER, C., SCHNABEL, J. A., CHUNG, D., CLARKSON, M. J., RUECKERT, D., HILL, D. L. G. & HAWKES, D. J. 2000. Volume and shape preservation of enhancing lesions when applying non-rigid registration to a time series of contrast enhancing MR breast images. *Medical Image Computing and Computer-Assisted Intervention - Miccai 2000,* 1935**,** 327-337.

TANNER, C., SCHNABEL, J. A., HILL, D. L., HAWKES, D. J., LEACH, M. O. & HOSE, D. R. 2006. Factors influencing the accuracy of biomechanical breast models. *Med Phys,* 33**,** 1758-69.

TANNER, C., WHITE, M., GUARINO, S., HALL-CRAGGS, M. A., DOUEK, M. & HAWKES, D. J. 2009. Anisotropic behaviour of breast tissue for large compressions. *IEEE International Symposium on Biomedical Imaging: From Nano to Macro***,** 1223-1226.

TANNER, C., WHITE, M., GUARINO, S., HALL-CRAGGS, M. A., DOUEK, M. & HAWKES, D. J. 2011. Large breast compressions: observations and evaluation of simulations. *Med Phys,* 38**,** 682-90.

UNLU, M. Z., KROL, A., MAGRI, A., MANDEL, J. A., LEE, W., BAUM, K. G., LIPSON, E. D., COMAN, I. L. & FEIGLIN, D. H. 2010. Computerized method for nonrigid MR-to-PET breast-image registration. *Comput Biol Med,* 40**,** 37-53.

VAN DE SOMPEL, D. & BRADY, M. 2008. Generation of realistic MR-derived breast phantoms for the validation of digital breast tomosynthesis reconstructions. *Medical Image Undestanding and Analysis.*

VAN ENGELAND, S., SNOEREN, P. R., HENDRIKS, J. H. & KARSSEMEIJER, N. 2003. A comparison of methods for mammogram registration. *IEEE Trans Med Imaging,* 22**,** 1436-1444.

VAN ENGELAND, S., SNOEREN, P. R., HUISMAN, H., BOETES, C. & KARSSEMEIJER, N. 2006. Volumetric breast density estimation from full-field digital mammograms. *IEEE Trans Med Imaging,* 25**,** 273-82.

VAN HOUTEN, E. E., DOYLEY, M. M., KENNEDY, F. E., WEAVER, J. B. & PAULSEN, K. D. 2003. Initial in vivo experience with steady-state subzone-based MR elastography of the human breast. *J Magn Reson Imaging,* 17**,** 72-85.

WARREN, R. & COULTHARD, A. (eds.) 2002. *Breast MRI in practice,* London: Martin Dunitz.

WELLMAN, P. S. 1999. *Tactile Imaging.* PhD Thesis, Harvard University.

WESSEL, C., SCHNABEL, J. A. & BRADY, M. 2010. A Biomechanical model of spiculated tumours under mammographic compressions. *IEEE Eng Med Biol Soc,* 2010**,** 712-5.

WIRTH, M. A., NARHAN, J. & GRAY, D. Year. Nonrigid mammogram registration using mutual information. *In:* SPIE Medical Imaging: Image Processing, 2002 San Diego USA. 562-573.

YIN, H. M., SUN, L. Z., WANG, G., YAMADA, T., WANG, J. & VANNIER, M. W. 2004. ImageParser: A tool for finite element generation from three-dimensional medical images. *BioMedical Engineering OnLine,* 3.

YU-NEIFERT, Q. 1995. *A three-dimensional finite element model to predict the applicability of holographic interferometry to breast tumour detection.* PhD, University of Akron.

ZHANG, M. & MAK, A. F. 1999. In vivo friction properties of human skin. *Prosthet Orthot Int,* 23**,** 135-41.

ZHANG, Y., SARKAR, S., QIU, Y., GOLDGOF, D. B. & LI, L. 2007. 3D finite element modeling of nonrigid breast deformation for feature registration in X-ray and MR Images. *IEEE Workshop on Applications of Computer Vision***,** 38-38.

ZIENKIEWICZ, O. C. & TAYLOR, R. L. 2005. The finite element method for solid and structural mechanics. 6th ed. Amsterdam ; Boston: Elsevier Butterworth-Heinemann.

ZUO, C. S., JIANG, A., BUFF, B. L., MAHON, T. G. & WONG, T. Z. 1996. Automatic motion correction for breast MR imaging. *Radiology,* 198**,** 903-6.